INL/EXT-19-55699-Rev001

September 2019

Summary of Bison milestones and activities - NEAMS FY19 Report

INL
S. R. Novascone, A. Casagranda, L. K. Aagesen, B. W. Beeler, W. Jiang, A. M. Jokisaari, D. J. McDowell, A. D. Lindsay, J. B. Tompkins, G. Pastore, A. X. Zabriskie, D. Schwen, R. L. Williamson, B. W. Spencer, A. E. Slaughter

ANL
Y. Miao, A. Oaks, A. M. Yacout

LANL
C. Matthews

Southwestern Scientific
D. S. Stafford

INL/EXT-19-55699-Rev001

Summary of Bison milestones and activities – NEAMS FY19 Report

INL
S. R. Novascone, A. Casagranda, L. K. Aagesen, B. W. Beeler, W. Jiang, A. M. Jokisaari, D. J. McDowell, A. D. Lindsay, J. B. Tompkins, G. Pastore, A. X. Zabriskie, D. Schwen, R. L. Williamson, B. W. Spencer, A. E. Slaughter

ANL
Y. Miao, A. Oaks, A. M. Yacout

LANL
C. Matthews

Southwestern Scientific
D. S. Stafford

September 2019

Idaho National Laboratory
Fuel Modeling and Simulation Department
Idaho Falls, Idaho 83415

Prepared for the
U.S. Department of Energy
Office of Nuclear Energy
Under U.S. Department of Energy-Idaho Operations Office
Contract DE-AC07-99ID13727

Contents

Chapter 1

Introduction

This summary report contains an overview of work performed under the work package entitled "FY2019 NEAMS Engineering Scale Fuel Performance", which is focused on the development and support of the fuel performance code Bison [1]. The second chapter lists FY19 milestones titles, completion schedule, and milestone level. Subsequent chapters summarize and demonstrate completion of milestones and activities. The last chapter outlines FY20 proposed future work.

In FY19, the NEAMS program emphasized development of Bison for its application to advanced reactors. While there are a variety of advanced fuel concepts, based on interaction with industry and the Nuclear Regulatory Commission, the two fuel types we chose to develop were metallic fast reactor and particle fuels.

Focusing on advanced reactor fuel types required changes in our development process. In light water reactor fuel performance modeling, data from physical experiments is used to develop empirical models. Considering the relative lack of experiment data for advanced reactors, an alternative method is required to develop fuel performance simulation capability. The alternate approach proposed by NEAMS is to develop and incorporate lower length scale models into engineering scale calculations.

The development team chose to begin this new approach with metallic fuel swelling. We chose this primarily because existing models performed poorly and there were obvious features of the swelling model that could be improved via an influx of lower length scale information. Details regarding this development process, applications, and a new plan for validating metallic fuel simulations are provided in chapters 3, 5, and 7.

The NEAMS fuels product line improved interaction among labs, especially in the area of metallic fuel. Significant contributions from LANL and ANL were made to the development of Bison metallic fuel capabilities in terms of code improvements and model development.

For particle fuel, we implemented a statistical failure model for TRISO layers. This model utilized the Monte Carlo method and is a new feature within MOOSE [2]. Due to the voluminous number of calculations required by the Monte Carlo method, memory allocation considerations were paramount and required significant contributions to the MOOSE framework to enable the functionality. We anticipate that the work on particle fuel will be of interest to the advanced reactor community. More details regarding the new failure model and our plan for validating particle fuel modeling capabilities in Bison are found in chapters 9 and 10.

Converting existing documentation of validation cases to an online format was a profound step toward making Bison more accessible. This involved converting dozens of latex files to markdown format and connecting to the ever evolving gitlab documentation system. Details about this milestone can be found in chapter 11.

Highlights of activities in FY19 are: improvements to frictional contact, using XFEM to simulate moving material interface, code robustness improvements, and supporting micro-reactor modeling development and simulation. Other activities that are typically yearly include improving code documentation, testing, and providing user training. See chapter 12 for more information.

The last chapter of this report documents proposed work for FY20. We plan to continue work on metallic and particle fuel in terms of developing/calibrating models and to begin rigorous validation/assessment for both fuel types. Due to the merger of the NEAMS and CASL programs, FY20 will see a return to light water reactor model development and simulation; this time focused on advanced technology fuels. Additionally, we seek to improve Bison, fundamentally. As such, we plan improvements to Bison and MOOSE in terms of algorithmic robustness, performance, ease-of-use, and quality assurance. See a detailed write-up in chapter 13.

Bibliography

[1] R. L. Williamson, J. D. Hales, S. R. Novascone, M. R. Tonks, D. R. Gaston, C. J. Permann, D. Andrs, and R. C. Martineau. Multidimensional multiphysics simulation of nuclear fuel behavior. *Journal of Nuclear Materials*, 423:149–163, 2012.

[2] D. Gaston, C. Newman, G. Hansen, and D. Lebrun-Grandié. MOOSE: A parallel computational framework for coupled systems of nonlinear equations. *Nuclear Engineering and Design*, 239:1768–1778, 2009.

Chapter 2

Milestone summary and completion schedule

FY-2019 Milestones and the completion dates are listed in Table 2.1. The milestones are listed by topic (metallic fuel, particle fuel, and validation documentation). Following chapters contain a short description of each milestone and references to related detailed documentation. Where applicable, a representative technical result from the work is included.

Table 2.1: FY-2019 Milestones for NEAMS INL-engineering scale fuel performance effort

Milestone	Completion Date	MS Level
Implement unit cell volumetric swelling model for metallic fuel	1/27	M3
Implement lower length scale informed swelling model for metallic fuel	6/20	M3
Develop validation plan for metallic fuel and run additional validation cases	8/15	M2
Implement failure models and statistical treatment to compute failure probability for particle fuel	6/23	M2
Develop validation plan for particle fuel and run additional cases	8/30	M3
Convert existing validation cases to new Bison documentation system	7/18	M3

Chapter 3

Implement unit cell volumetric swelling model for metallic fuel

L. K. Aagesen
A. Casagranda
C. Matthews

3.1 Background

A recurring problem while running metal fuel simulations has been obtaining reliable convergence behavior. The original fuel swelling model is believed to be a source of some of the robustness issues observed in metal fuel simulations. An example of the convergence problems was observed early on while running the X447 example model with Zr redistribution and fuel creep active. When running this model on our HPC system, the following warning would be generated:

```
*** Warning ***
Gaseous swelling strain, calculated in VSwellingUPuZr, is large. This is due
to large, positive values for hydrostatic stress. Consider taking smaller
times steps and using elements with low aspect ratio.
```

This message would be output in the first few steps of the analysis. Subsequently, in the next couple of time steps, a MooseException would be generated:

```
A MooseException was raised during Auxiliary variable computation.
The next solve will fail, the timestep will be reduced, and we will try again.
```

However, at this point the run would fail and the PBS error file contained the following message.

```
Encountered inf or nan in material return mapping iterations.
At element 1435 _qp=0 Coordinates (x,y,z)=(0.00186784, 0.0752564,        0) block=3
In 1000 iterations the residual went from nan to nan in 'fuel_upuzrcreep'.
```

The first warning message above originates in the metal fuel swelling model, VSwellingUPuZr, and indicates that the gaseous volumetric swelling strain is increasing rapidly due to the hydrostatic stress. The equation for gaseous swelling is given as

$$\left(\frac{\Delta V}{V_0}\right)_g = \frac{3.59\times10^{-24} F T}{1.01\times10^{7} - \sigma_h} \tag{3.1}$$

where one can see that as $\sigma_h \rightarrow 1.01\times10^7$ the denominator approaches zero. This behavior is problematic and inherent in the formulation of the original swelling model.

When convergence issues are encountered in numerical simulations, a common strategy is to simplify the models being used. Applying this approach to the metal fuel simulations, we attempted to streamline the mechanics of the fuel

by using an elastic material model and disabling fuel creep. However, due to the interplay between the fuel swelling and creep models, when elastic fuel was used fission gas release did not occur. This in turn caused the plenum pressure to be much lower than expected and therefore resulted in the cladding strains being incorrect.

Finally, whenever the fuel swells and begins to contact the cladding, persistent numerical difficulties have been encountered. Typically, the time step size is rapidly reduced until eventually reaching the minimum size allowed and the simulation is terminated. Other fuel-cladding systems such as oxide fuel and zirconium do not exhibit this behavior, however, the boundary conditions on the cladding are very different. In PWRs the external pressure on the cladding is significantly higher than the plenum pressure and generally keeps the cladding in contact with the fuel. In the case of EBR-II simulations, the external pressure is atmospheric and the plenum pressure is usually greater especially at higher burnups. Therefore, the cladding is creeping outwards at the same time as the fuel swells into contact with the cladding. This "soft" contact is difficult to model and may require modifications to the contact algorithms in Bison.

3.2 New Implementation of Simple Volumetric Swelling Model

A new model for volumetric swelling in U-Pu-Zr fuels, `UPuZrVariableRBubSwellingEigenstrain`, was developed and merged to Bison. The model includes swelling due to gas bubble formation and solid fission product swelling in the fuel matrix. It differs from the previous model for swelling in U-Pu-Zr fuels, `UPuZrVolumetricSwellingEigenstrain`, in the model for gas swelling in that it allows for variation in gas bubble radius and assumes the number density of bubbles is constant. This is based on the assumption of one-off nucleation of fission gas bubbles.

3.2.1 Gaseous Swelling

The derivation for the mechanistic fuel swelling model for U-Pu-Zr systems used here was originally presented in [1]. The gaseous fission product swelling is given as

$$\left(\frac{\Delta V}{V_0}\right)_g = \left(\frac{3}{4\pi}\right)^{1/2} \frac{[(kT/2\gamma)Y_{Xe}\dot{F}t]^{3/2}}{N^{1/2}} \tag{3.2}$$

where k is the Boltzmann constant, T is the temperature in K, γ is the surface energy of the fuel-bubble interface (and equal to 0.8 J/m^2 from [2]), Y_{Xe} is the gaseous fission product yield, $\dot{F}$ is the fission rate density, t is time, and N is the number density of bubbles. The derivation is based on the following assumptions:

1. The number density of bubbles is constant and their size is uniform (coalescence and coarsening of the bubbles are thus neglected)
2. The gas within the bubbles can be treated as an ideal gas (appropriate for larger bubbles)
3. The gas/vacancy ratio in the bubbles is in equilibrium, i.e. the bubbles are not over- or under-pressurized
4. All the gas produced in the fuel is transported immediately to bubbles and remains there; thus, the time required for gas to diffuse from the fuel to the bubbles and the re-solution of fission gas atoms from the bubbles are neglected (this assumption conflicts with the empirical solid swelling model described in Section 3.2.2; plans to resolve this inconsistency are described in Section 3.5).
5. The solid is assumed to be un-stressed
6. All swelling is due to intragranular bubbles; the effect of intergranular bubbles is neglected

3.2.2 Solid Swelling

Swelling due to solid fission products is assumed to be 1.5% per 1% burnup as suggested by [3]:

$$\left(\frac{\Delta V}{V_0}\right)_s = 4.16 \times 10^{-29} F \tag{3.3}$$

where F is the fission density in fissions/m^3, V is the current volume, and V_o is the original volume.

3.2.3 Total Isotropic Volumetric Swelling

Following [4], the total volumetric swelling is the summation of contributions from gaseous and solid swelling:

$$\left(\frac{\Delta V}{V_0}\right)_{total} = \left(\frac{\Delta V}{V_0}\right)_g + \left(\frac{\Delta V}{V_0}\right)_s \tag{3.4}$$

3.3 Metal Fuel Model Robustness Improvements

3.3.1 Convergence Issue Due to Hydrostatic Stress

The first simulation used to test the new mechanistic volumetric swelling model for UPuZr was the X447 example problem including the effect of Zr redistribution. This simulation failed fairly early on due to the increasing hydrostatic stress causing numerical problems in the original swelling model. Since the new model is not dependent on the hydrostatic stress, it should behave better. Figure 3.1 shows the fission gas release predicted by Bison for this case. Although the simulation did not run to completion, it ran much farther than the original run and also exhibits the typical fission gas release behavior for metal fuel which is encouraging.

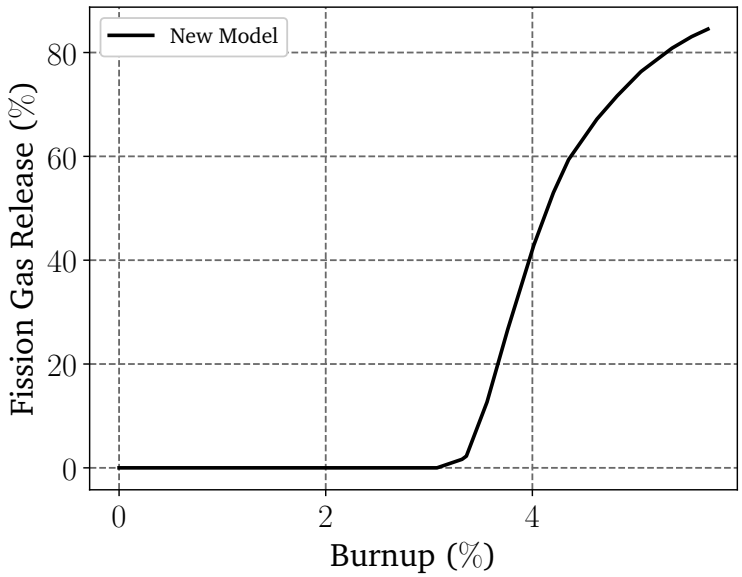

Figure 3.1: Fission gas release as function of burnup for new swelling model in X447 simulation including Zr redistribution.

3.3.2 Comparisons of Original and New Swelling Models

Since the X447 example including Zr redistribution did not run to completion with the original swelling model, a version of the model without Zr redistribution will be used to compare Bison solutions. Using the default parameter values for the original and new swelling models both simulations were able to run to completion.

Figure 3.2 shows a comparison of the fission gas release as a function of burnup using both models. The new model being based on a constant number of bubbles growing in isolation (i.e., no coalescence) should swell more slowly and thus the fission gas release is delayed.

Figures 3.3 and 3.4 shows a comparison of the porosity and volumetric strain which confirms that the new model predicts slower swelling.

In addition, Figures 3.5 and 3.6 show the plenum pressure and hydrostatic stress as a function of time. Once again, the new model predicts a slower increase in both the plenum pressure and hydrostatic stress as expected.

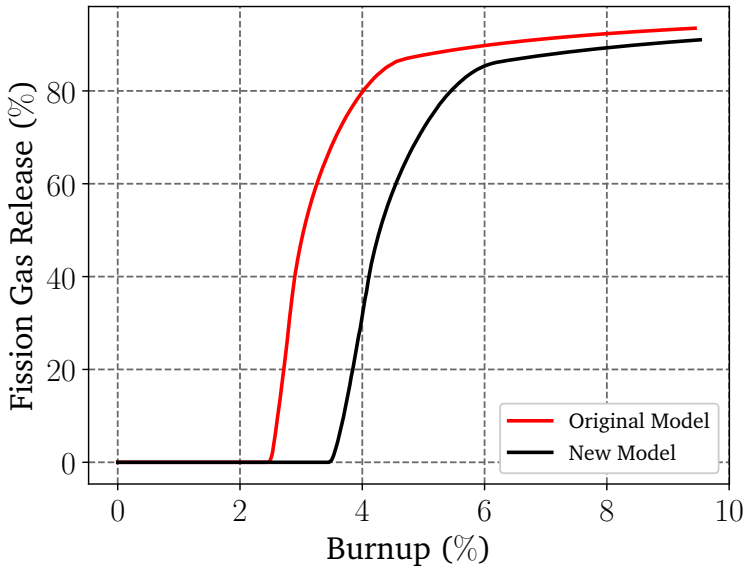

Figure 3.2: Comparison of fission gas release between original and new swelling models.

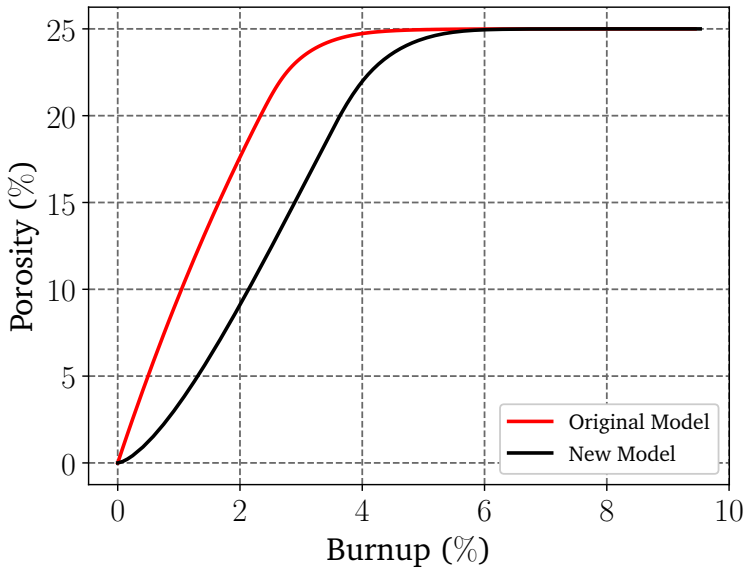

Figure 3.3: Comparison of porosity between original and new swelling models.

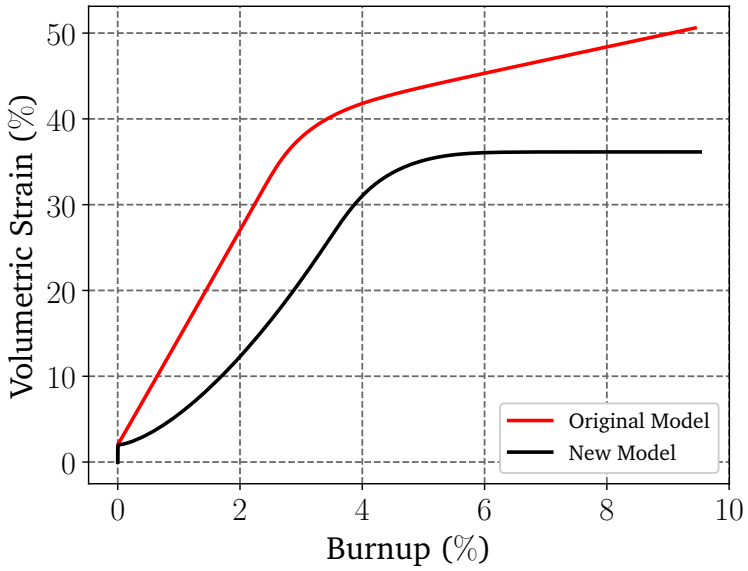

Figure 3.4: Comparison of volumetric strain between original and new swelling models.

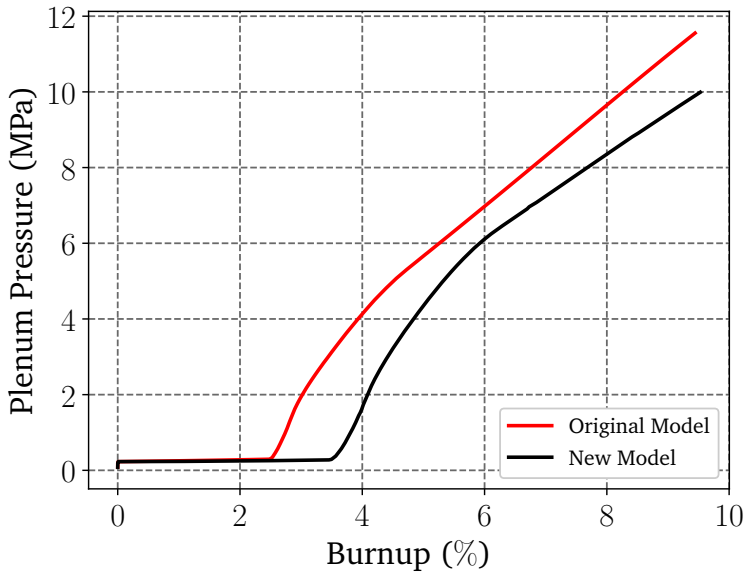

Figure 3.5: Comparison of plenum pressure between original and new swelling models.

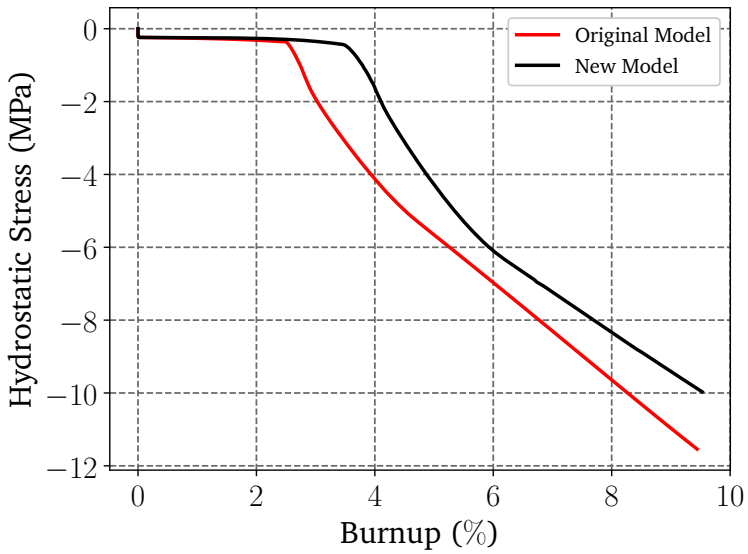

Figure 3.6: Comparison of hydrostatic stress between original and new swelling models.

Figure 3.7 shows the effect of the bubble number density parameter on the porosity evolution for the new swelling model. The default value of N = 1e20 provides a smooth increase in porosity over time. However, increasing the bubble number density implies that the bubble size is smaller which causes the swelling to decrease. In contrast, decreasing the bubble number density implies that the bubble size is larger which results in an acceleration of the predicted porosity.

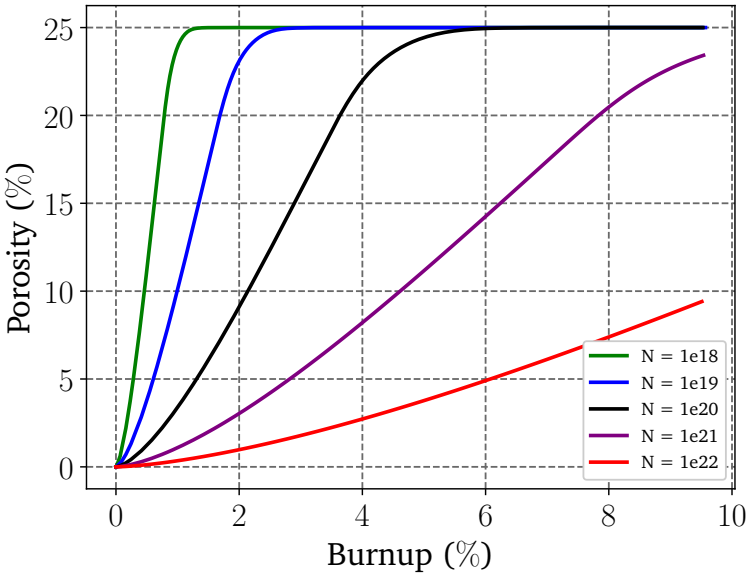

Figure 3.7: Comparison of porosity evolution for new model with varying bubble number density, N.

Figure 3.8 shows the effect of the bubble number density on the fission gas release prediction. As expected with an increase in the number density of bubbles and subsequent decrease in porosity, the fission gas release is reduced. In the extreme with a value of N = 1e22, Figure 3.8 shows that fission gas release is completely inhibited.

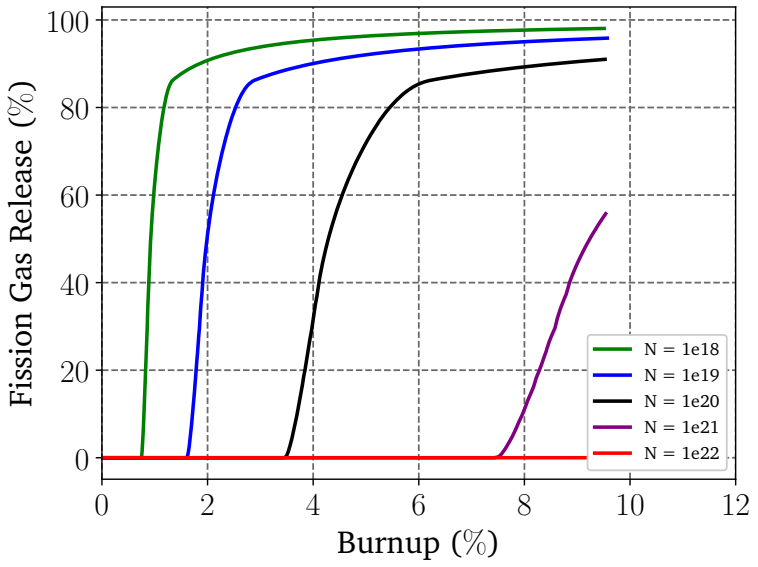

Figure 3.8: Comparison of fission gas released for new model with varying bubble number density, N.

Model	Run Time(s)	# Linear Iterations	# Nonlinear Iterations
With UPuZr Creep	5281	28955	4975
Elastic Fuel	2458	12986	2330

Table 3.1: Comparison of convergence quantities for simulations with and without UPuZr creep

Figures 3.9 and 3.10 show the effect of the surface energy of the fuel-bubble interface, γ, on the porosity evolution and fission gas release predictions. In a similar way to the bubble number density, as the value of γ decreases, the porosity evolution is quickened and thus the fission gas release is also accelerated. An increase in the value of γ results in a decreasing of the porosity evolution and delaying fission gas release.

Although, the sensitivity of the Bison predictions to N and γ is similar, the magnitude of the changes in these parameters needed to demonstrate these effects is very different. The changes in N are two orders of magnitude whereas the changes in γ are only a factor of 2. Therefore, the uncertainties in the value of γ are more significant and should be minimized through either experimental measurements or lower-length scale calculations to provide the "best estimate" value as soon as possible.

The possible simplification of the current metal fuel models in order to improve robustness was revisited with the new swelling model. Specifically, the elimination of the UPuZr creep material model, which with the original model caused the fission gas release to not occur, was tried again. Figures 3.11 and 3.12 show the porosity and fission gas release predictions,respectively, for the X447 model both with and without the UPuZr creep model. It can be seen that the results are identical. Therefore, this may now be a useful modification to metal fuel models for specific scoping calculation where UPuZr creep may not be an important contribution. In addition, a significant improvement in performance was observed and is summarized in Table 3.1. The time step size has generally been limited due to the sensitivity of the UPuZr creep model and these results were obtained with those limits still in place. The maximum time step size could probably be increased in the elastic fuel simulation and not drastically change the results which would further increase the performance benefits.

3.4 Conclusions

The goal of this work was to implement a new volumetric swelling model for UPuZr to improve the robustness of metallic fuel simulations. A mechanistic-based swelling model was added to Bison and applied to simulations of

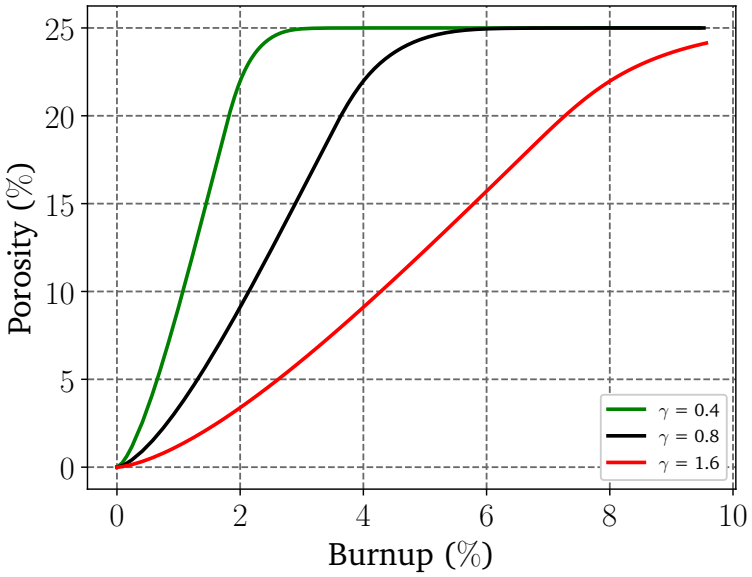

Figure 3.9: Comparison of porosity evolution for new model with varying surface energy of the fuel-bubble interface, γ.

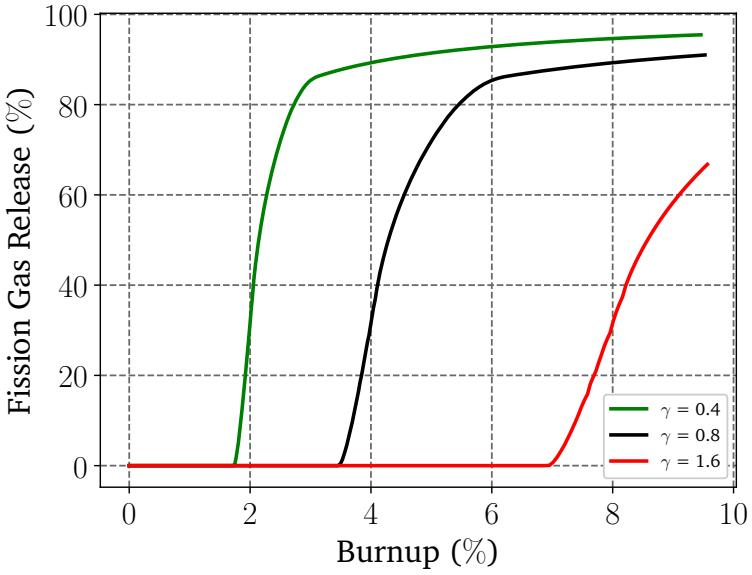

Figure 3.10: Comparison of fission gas released for new model with varying surface energy of the fuel-bubble interface, γ.

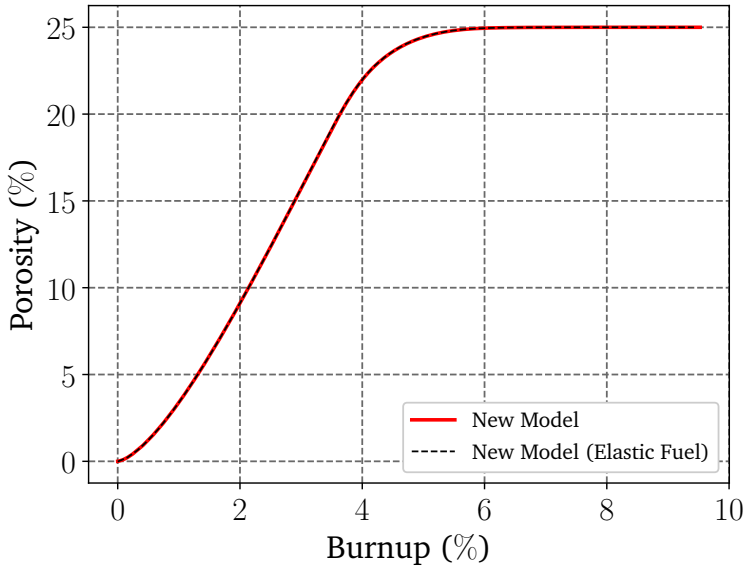

Figure 3.11: Comparison of porosity evolution with new swelling model and modeling the fuel with and without UPuZr creep.

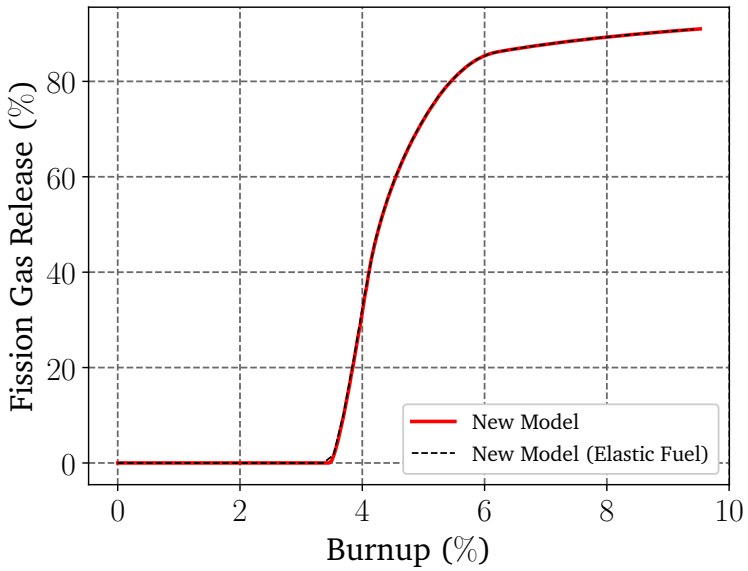

Figure 3.12: Comparison of fission gas release with new swelling model and modeling the fuel with and without UPuZr creep.

EBR-II experiments. The new swelling model allowed a metal fuel simulation including Zr redistribution to run to $\sim 5\%$ burnup whereas the original metal fuel swelling model generated warnings and terminated the simulation very near the start of the run.

EBR-II simulations without Zr redistribution make up the majority of the results presented in this report. The Bison results using the new model were similar to the original model in this case, but did not suffer the sensitivity to the hydrostatic stress that the original model exhibited. Thus, simplifications to metal fuel simulations, such as using elastic fuel (i.e., ignoring fuel creep), worked well and provided a significant improvement in performance.

Finally, the parameters in the new swelling model, N and γ, that control the volumetric swelling were investigated. The Bison predictions of porosity evolution and fission gas release are sensitive to both of these parameters. However, the value of γ has a somewhat larger effect on the Bison results than N and should be the focus of additional research.

3.5 Future Work

Future work to improve the swelling model described in this report will be undertaken using a combination of lower-length scale calculations and experiments. As seen in Eq. 7.11, γ has a strong impact on the predicted swelling from fission gas bubbles. Although Ref. [2] cited a value of $\gamma = 0.8$ J/m^2, in attempting to find the original source of this value through the references listed, it could not be determined where the original measurement or calculation of this value was performed. It is thus believed that this was an assumption based on a reasonable value for a typical surface energy. To improve the model, a value for the bubble-solid surface energy will be calculated using molecular dynamics, using an existing interatomic potential for this system.

Additional future work to improve the prediction of gaseous swelling will be performed using both lower length scale modeling and experimental data. Several assumptions underlying the newly developed swelling model are described in Section 3.2.1. The model will be improved to relax those assumptions, with highest priority placed on the assumptions that are believed to have the greatest impact on the model's predictions.

Assumption 1: The number density of bubbles is constant and their size is uniform. In classical nucleation theory, the nucleation rate is an extremely sensitive function of parameters such as the surface energy. Therefore, it is difficult to obtain quantitatively accurate predictions of bubble number density, even at the the early stages of swelling before bubbles begin to coalesce. From Eq. 7.11, $\left(\frac{\Delta V}{V_0}\right)_g \propto \frac{1}{\sqrt{N}}$, so the impact of N is not as strong as that of γ; however, because of the strong dependence of N on γ and other parameters, it can easily vary by several orders of magnitude. Thus, addressing the uncertainty due to assumption 1 is given a priority of **high**.

The model will initially be parameterized using literature data for bubble density from existing experimental measurements. Cluster dynamics simulations will be used to determine initial bubble number density and determine how the bubble number density affects swelling in the early stages. For validation of the cluster dynamics modeling, there is no existing experimental measurement of bubble density at low burnup, before bubble coalescence would be expected to significantly impact the bubble number density. Therefore, experimental measurements of bubble density at low burnup will be added to the post-irradiation examination plan for U-10Zr fuel which will be irradiated in the Advanced Test Reactor (ATR). These samples are planned for irradiation as part of ATR cycle 168A (currently planned for December 2019-March 2020).

At the later stages of swelling, coalescence of growing bubbles may significantly affect the bubble number density, particularly since porosity reaches a relatively high value of 25% before it is assumed that the porosity becomes fully interconnected and further gas produced is directly released from the fuel. To determine the effect of coalescence on N, a combination of cluster dynamics simulations and microstructure-level phase-field simulations of growing bubbles will be performed. For a given initial bubble number density, the bubble number density $N(p)$ will be determined as a function of porosity p. Then, the model of Eq. (7.11) will be modified to use the porosity-dependent number density $N(p)$.

Assumption 2: The gas within the bubbles can be treated as an ideal gas. The behavior of the gas within the bubbles is expected to deviate from ideal gas behavior only when the bubbles are very small ($r < 10$ nm). However, the bubbles are only this small at low burnup, and swelling at such low burnup is not expected to significantly affect fuel performance. As the bubbles grow larger, pressure within them decreases, and the ideal gas equation of state becomes valid. Therefore, addressing the uncertainty caused by Assumption 2 is given a priority of **low**.

Assumption 3: The gas/vacancy ratio in the bubbles is in equilibrium. In the case where there is an under- or over-supply of vacancies, the condition of equilibrium gas/vacancy ratio may not be met, and the size of the bubbles is smaller or larger, respectively, than predicted by the original analytical solution which is used to derive Equation 7.11.

For the case of an under-supply of vacancies, an approximate analytical solution for the average bubble radius is given in Ref. [1] as

$$R(t) = R_{eq}(t) - Kt \tag{3.5}$$

where $R(t)$ is the average bubble radius as a function of time, $R_{eq}(t)$ is the average radius of bubble with equilibrium gas/vacancy ratio, and K is a constant dependent on vacancy diffusivity, bubble number density, production rate of gas atoms, and equilibrium vacancy concentration. However, it is not known whether conditions in U-Pu-Zr fuel lead to an over-supply or under-supply of vacancies. It is also unknown what functional form should be used in the case of over-supply. Thus, addressing the uncertainty caused by assumption 3 is given a priority of **high**. A phase-field model of gas bubbles embedded in a solid matrix, which includes gas atoms and vacancies, is currently under development. This model will be parameterized using atomistic calculations for required parameters, such as the bubble-solid surface energy (previously described) and vacancy diffusivity, with initial bubble number density determined using cluster dynamics simulations. Simulations of bubble growth will be conducted to determine if Eq. 3.5 is valid for the conditions of bubble growth in U-Pu-Zr fuel, or if a different functional form is required. The value of K (or other parameters if a different functional form is required) will be determined based on phase-field simulations, and the Bison swelling model will be updated to reflect the revised average bubble size.

Assumption 4: All the gas produced in the fuel is transported immediately to bubbles and remains there; thus, the time required for new fission gas atoms to diffuse from the fuel to the bubbles and the re-solution of fission gas atoms from the bubbles are neglected. Because of these assumptions, the amount of gaseous swelling is over-estimated. Both effects are expected to be more important at lower temperatures, because at lower temperatures the diffusivity of fission gas atoms is lower, so atoms are slower to diffuse back into the bubbles [1]. Because metallic fuel operates at lower temperatures relative to UO_2, diffusion and re-solution are expected to be important effects on swelling, and addressing the uncertainty introduced by Assumption 4 is given a priority of **high**. The fraction of gas atoms in bubbles re-deposited to the matrix, f_b, is given by [1]:

$$\frac{1-f_b}{f_b^{2/3}} = \frac{b}{CN^{2/3}D_{Xe}(Y_{Xe}\dot{F}t)^{1/3}} \tag{3.6}$$

where C is a constant and D_{Xe} is the diffusivity of Xe atoms in the solid. Lower-length scale simulations will be used to test the validity of this functional form and determine the value of the constant C. Cluster dynamics can be used to determine the effect of diffusion and re-solution to the amount of fission products remaining in the solid matrix. To investigate this phenomenon with phase-field modeling, the previously mentioned phase-field model of will need to be modified to incorporate re-solution of gas atoms into the matrix.

Assumption 5: The solid is assumed to be un-stressed. If the solid is instead in a state of hydrostatic stress, for an equilibrium bubble, the pressure inside the bubble P is given by the Laplace-Young equation as

$$P = -\sigma_H + \frac{2\gamma}{R} \tag{3.7}$$

where σ_H is the hydrostatic stress in the solid (the negative sign is due to the fact that the sign convention for compressive stresses is negative). The effect of stress in the solid is to shift the bubble pressure upward slightly, which may be a stronger impact as the bubbles become larger. The modification that would result to Equation 7.11 would not require lower length scale parameterization. The effect on predicted swelling is expected to be low to moderate. Therefore, addressing the uncertainty caused by Assumption 5 is given a priority of **medium**. Experience with the previous swelling model that incorporated hydrostatic pressure in the solid was that considerable difficulty in the Bison nonlinear solver resulted when hydrostatic pressure was included; this is expected to be the largest barrier to implementation.

Assumption 6: All swelling is due to intragranular bubbles; the effect of intergranular bubbles is neglected. In Ref. [5], fission gas bubbles in U-Pu-Zr fuel were studied. It was found that there was not a significant amount of intergranular bubbles in the high-temperature zone, which consists primarily of the γ-U phase. Because local swelling is proportional to $T^{3/2}$, the total volumetric swelling is dominated by bubbles in the high-temperature region. Because few intergranular bubbles were observed in the high-temperature region, this lends support to the assumption that the effect of intergranular bubbles can be neglected. However, more significant amounts of intergranular bubbles were found in the intermediate temperature zone, and thus it may not be valid to completely neglect intergranular bubbles. Thus, addressing the uncertainty associated with Assumption 6 is given a priority of **medium**.

Bibliography

[1] D.R.Olander. *Fundamental aspects of nuclear reactor fuel elements*. Technical Information Center, Energy Research and Development Administration, 1976.

[2] Aydin Karahan. *Modeling of thermo-mechanical and irradiation behavior of metallic and oxide fuels for sodium fast reactors*. PhD thesis, Massachusetts Institute of Technology, June 2009.

[3] T. Ogata and T. Yokoo. Devlopment and Validation of ALFUS: An Irradiation Behavior Analysis Code for Metallic Fast Reactor Fuels. *Journal of Nuclear Technology*, 128(1):113–123, 1999.

[4] A. Karahan and J. Buongiorno. A new code for predicting the thermo-mechanical and irradiation behavior of metallic fuels in sodium fast reactors. *Journal of Nuclear Materials*, 396:283–293, 2010.

[5] D. Yun, J. Rest, and A. M. Yacout. Assessment of a mechanistic model in U-Pu-Zr metallic alloy fuel fission-gas behavior simulations. In *Proceedings of ICAPP 2012*, Chicago, IL, 2012.

Chapter 4

Implement Low-Temperature Swelling Model for Metallic Fuel

A. M. Jokisaari

An additional new model for low-temperature swelling in U-Pu-Zr fuels, `UPuZrPorosityEigenstrain`, was developed and is scheduled to be merged into Bison in early FY20. This materials model computes a volumetric strain to account for low-temperature swelling due to the presence of the α-uranium phase. Until now, the U-Pu-Zr fuel swelling model in Bison incorporated only one fuel swelling mechanism, gaseous swelling, and underpredicts swelling behavior with burnup for EBR-II fuel. The new model accounts for low-temperature swelling based on observations of α-uranium and fuel alloys.

4.1 Low-Temperature Swelling Introduction

Low-temperature swelling in U-Pu-Zr fuel operates via a different mechanism from gaseous and solid fission product swelling and much remains to be understood. Here, a model and Bison implementation are developed for low-temperature swelling based on observations of α-uranium and fuel alloys. Using the EBR-II X441assessment case, the effect of the new low-temperature swelling model on the evolution of fuel slug porosity is studied. It is found that the low temperature swelling mechanism improves agreement between the model predictions of fuel deformation with experimental results of EBR-II fuel at low burnup. In addition, the new model predicts the formation of a highly porous fuel region at or near the fuel slug surface, which is observed experimentally. This region is not predicted with the gaseous swelling model, supporting the incorporation of the low-temperature swelling model.

For material containing the α-uranium phase, porosity appears to form rapidly with burnup due to cavity formation [1]. This porosity formation appears to be temperature-dependent, with less occurring at lower temperatures and more at higher temperatures [1], and appears to be similar to the swelling behavior of unalloyed or low-alloyed α-uranium [2]. Between approximately 623 K and 873 K, α-uranium forms extensive internal cavities, causing major swelling [2]. At lower temperatures within this range, these cavities appear ragged, suggesting grain boundary tearing likely due to stresses induced by anisotropic irradiation growth of α-uranium crystals [3]. Minor alloying additions of insoluble elements (e.g., Fe, Si) appear to reduce the swelling rate [2, 4, 5]. Notably, the addition of Pu only, which is soluble up to 16% in α-uranium, does not improve the swelling behavior [6, 7]. These results indicate that the presence of dispersed second phases in α-uranium reduce swelling behavior.

The U-Zr and U-Pu-Zr fuels were developed after extensive EBR-II operational experience with U-Fs fuel, where Fs denotes "fissium" [8]. The U-Fs and U-Pu-Fs alloys exhibit better dimensional stability under irradiation than pure uranium or U-Pu binary alloys [9, 10], i.e., less swelling and irradiation growth. Similar to other fuel alloys, the alloying elements form precipitates [11, 12]. Uranium-fissium fuels form the equilibrium α/δ phases in reactor at temperatures below the γ phase boundary [12]. For U-5Fs driver fuel irradiated at temperatures below 833 K, tearing porosity similar to that observed in α-uranium and U-Zr is observed [12].

To our knowledge, no data exists characterizing the swelling rate as a function of temperature for U-Zr fuel similar to the data that exists for pure and low-alloyed uranium. However, swelling rates for U-Fs appear to be similar to those for low-alloyed uranium [2, 12], and fission gas release with respect to fuel volume increase appears to be the same

Table 4.1: Polynomial parameters for Eq. 4.4 in the LTS model.

Coefficient	Value
a	-2.65845×10^{-9}
b	1.06170×10^{-5}
c	-1.68844×10^{-2}
d	1.33644×10^{1}
e	-5.26459×10^{3}
f	8.25666×10^{5}

for U-Fs, U-Pu-Fs, and U-Zr, [13] indicating the same swelling mechanisms at work. Thus, it appears that uranium-based metallic fuels that exhibits the α phase with precipitates will exhibit similar low-temperature swelling behavior, forming the basis for this model.

4.2 Model

The new low-temperature swelling model defines a temperature-dependent swelling rate, R, with respect to the local burnup. The swelling rate is defined as

$$\sigma(T) \equiv \frac{d\theta_{LT}(T)}{d\beta}, \tag{4.1}$$

where θ_{LT} is the low-temperature swelling. In this model, the equation for σ is given by fitting a fifth-order polynomial to the data in Ref. [2] within upper and lower bounding temperatures, denoted as T_{high} and T_{low}, respectively. Because the fit is intended to capture a single peak within the bounding temperatures, the fit is linearly extrapolated outside the bounding temperatures, that is,

$$\sigma(T) = \frac{d\sigma}{dT}|_{T_{low}}(T - T_{low}) + \sigma(T_{low}), \qquad T < T_{low} \tag{4.2}$$

$$\sigma(T) = aT^5 + bT^4 + cT^3 + dT^2 + eT + f, \qquad T_{low} \leq T \leq T_{high} \tag{4.3}$$

$$\sigma(T) = \frac{d\sigma}{dT}|_{T_{high}}(T - T_{high}) + \sigma(T_{high}), \qquad T > T_{high} \tag{4.4}$$

where the coefficients are provided in Table 4.1. If the calculated $\sigma < 0$, then $\sigma = 0$ is used. In this work, $T_{low} = 675$ K and $T_{high} = 845$ K.

In the model, certain aspects of the porosity and swelling are user-defined. A maximum porosity that the fuel attains before fission gas release, P_{max}, and an initial porosity that the fuel is fabricated with, P_{init}, are specified. The total porosity that can then form in the fuel, P_{form}, is $P_{form} = P_{max} - P_{init}$. Thus, the total swelling that can form in the fuel, θ_{form}, is

$$\theta_{form} = P_{form}/(1 - P_{form}). \tag{4.5}$$

The current local swelling in the fuel, θ_t, that includes low temperature swelling and gas swelling, is calculated with an incremental formulation as

$$\theta_t = d\theta_{LT} + \theta_{LT,t-1} + \theta_g \tag{4.6}$$

where $d\theta_{LT}$ is the low-temperature swelling increment for this time step and $\theta_{LT,t-1}$ is the accumulated low-temperature swelling through the previous time step. The low-temperature swelling increment is calculated as

$$d\theta_{LT} = \sigma(T)d\beta, \tag{4.7}$$

where $d\beta$ is the burnup increment from the previous time step to the current time step. With this incremental formulation, the swelling is path-dependent and not a state function of temperature, e.g., if the fuel cools and the swelling rate decreases after swelling formation, the total swelling will not be reduced by recalculating with the lower swelling rate.

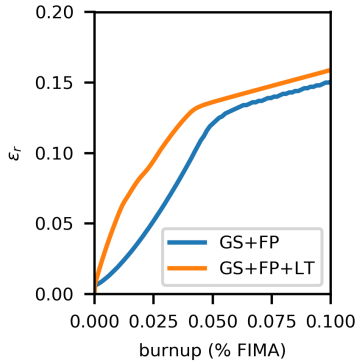

Figure 4.1: The radial strains for the original fission gas plus solid fission product swelling (GS+FP) and the new model with low temperature swelling (GS+FP+LT) at the bottom of the fuel.

Because there is a limitation on θ_{form}, $d\theta_{LT}$ is modified if $\theta_t > \theta_{form}$,

$$d\theta_{LT} = \theta_{form} - \theta_{LT,t-1} - \theta_g, \tag{4.8}$$

such that total gaseous swelling calculated is included and the maximum swelling is not exceeded. Thus, the total swelling formed in the fuel, θ_t, is

$$\theta_t = d\theta_{LT} + \theta_{LT,t-1} + d\theta_g + \theta_{g,t-1} \tag{4.9}$$

The total current porosity in the fuel, P_t, is calculated as

$$P_t = \frac{\theta_t}{1-\theta_t} + P_{init}. \tag{4.10}$$

4.3 Results and Discussion

In this comparison, two-dimensional axisymmetric simulations of the EBR-II X441 group A fuel slug and cladding are performed. The fuel has a composition of U-19Pu-10Zr in weight percent. The radial and axial strains and the evolution of the porosity are studied. Comparisons are made, when possible, to experimental data. The original Bison model is denoted as "GS+FP," while the new model with the low temperature swelling included is denoted as "GS+FP+LT."

The addition of the low-temperature swelling model changes the radial and axial strains, denoted as ε_r and ε_z, respectively. The addition of the low-temperature swelling causes faster radial swelling, as seen in Fig. 4.1 for the bottom of the fuel. The effect is most prominent at the bottom of the fuel, followed by the top, and is least at the middle of the fuel. The axial strain accumulation is also accelerated with the GS+FP+LT model, as shown in Fig. 4.2. However, while the total amount of strain accumulated before fission gas release (apparent by a change in the slope of the strain) for the two models is approximately same in the radial direction, the total axial strain is less for the GS+FP+LT model.

The radial and axial strains are compared to available EBR-II data [1]. A comparison of the EBR-II data and simulated values at a low burnup of 0.4% are shown in Fig. 4.3. The simulated axial and radial strains are greater with the addition of the low-temperature swelling. The GS+FP prediction for ε_r is significantly under any measured value, while the GS+FP+LT predictions for ε_r and ε_z are both within the range of experimental measurements, depending on the exact composition of the experimentally measured fuel.

At a burnup of 0.9% (Fig. 4.4), the GS+FP model underpredicts ε_z and especially ε_r, while the GS+FP+LT model predicts ε_z within the range of experimental data. The value of ε_r is still underpredicted, but is larger. It is evident that while the addition of the new low-temperature swelling model improves the prediction toward EBR-II data, there is still a significant underprediction of radial and swelling with increasing burnup, likely due to underprediction of gas swelling.

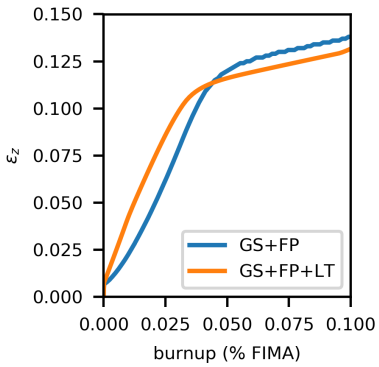

Figure 4.2: The overall axial strain for the original fission gas plus solid fission product swelling (GS+FP) and the new model with low temperature swelling (GS+FP+LT).

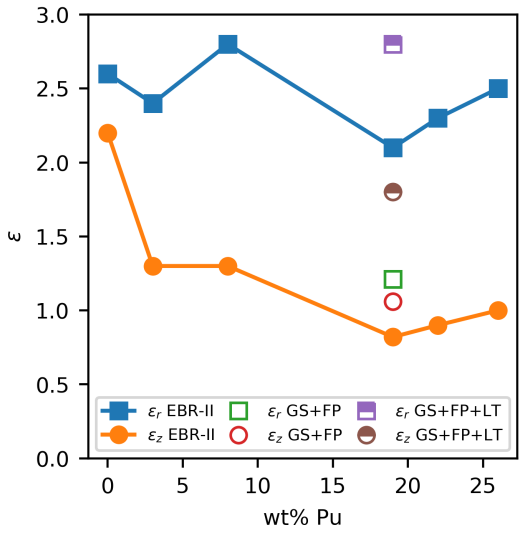

Figure 4.3: A comparison of EBR-II data to simulated data for radial and axial strains at a burnup of 0.4%.

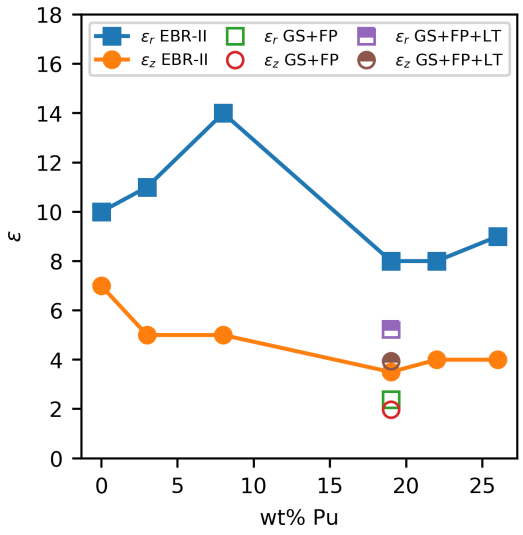

Figure 4.4: A comparison of EBR-II data to simulated data for radial and axial strains at a burnup of 0.9%.

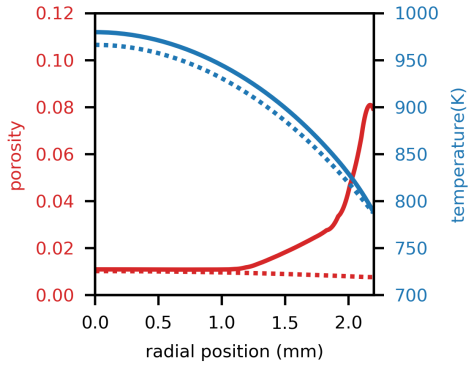

Figure 4.5: Radial porosity and temperature profiles for the X441 group A assessment at a burnup of 0.4% at the fuel slug midpoint. The solid lines indicate the GS+FP+LT results, while the dashed lines indicate the GS+FP results.

After the initial power ramp, the low-temperature swelling model predicts the development of a highly porous rim on the outer edge of the fuel slug. Radial porosity and temperature profiles are shown in Fig. 4.5 at the fuel slug midpoint for a burnup of 0.4%. The dashed lines indicate the results of the GS+FP model, while the solid lines indicate the results of the GS+FP+LT model. The porosity is significantly greater and rises sharply toward the outer edge of the fuel slug with the GS+FP+LT model. The peak low-temperature swelling rate occurs around 750 K and decreases rapidly; the temperature at the outer edge of the fuel is within the range of activity of low temperature swelling.

This highly porous structure on the outer edge of the fuel or as a porous ring within the fuel is observed experimentally in EBR-II fuel [1]. It occurs in both U-Zr and U-Pu-Zr fuels, though the exact morphology varies depending on burnup, experiment, and composition. In particular, the edge porosity appears to be a ragged structure, indicating involvement of the α phase. Currently, the cause of this porous edge structure or ring structure is unknown; however, the qualitative agreement between the experimental and simulated observations suggests that low-temperature swelling may be responsible for this structure. Further experimental characterization of phase and composition, as well as knowledge of the local temperature, is needed to ascertain if this mechanism is the cause of all ring and edge porosity, or if another mechanism might be at active. While the model appears to have the correct order of magnitude of the swelling rate with respect to burnup and temperature, comparisons of predicted and measured porosity can also

help to reduce the uncertainty in the rate of the porosity formation with respect to burnup and temperature for different U-Pu-Zr fuel compositions.

4.4 Conclusion

In this work, a simple low-temperature swelling model for U-Pu-Zr fuel is proposed and tested in combination with the existing gaseous swelling and solid fission product swelling models within Bison. The low-temperature swelling model causes a burnup-dependent porosity to develop within a temperature range of 645 K - 875 K. The rate of swelling with respect to burnup is based on that of low-alloyed uranium, given experimental observations of swelling and fission gas release rates for low-alloyed uranium, U-Fs, and U-Pu-Zr fuels. The swelling mechanism is not well understood, but is likely due to the development of intergranular tears (cavitation) as a result of internal stresses arising from irradiation-induced growth strains in polycrystalline α-uranium.

The model is tested via the EBR-II X441 group A assessment case within Bison. It is found that the addition of the low-temperature swelling model improves Bison predictions with respect to EBR-II data, especially at very low burnups (0.4%), At higher burnups (0.9%), the model still underpredicts swelling. It appears that the low-temperature swelling model improves fuel performance predictions at low burnup, but gaseous swelling is not sufficiently captured, which will cause additional swelling throughout the fuel as burnup continues. However, the predicted formation of a highly porous region at the outer fuel surface or in a ring within the fuel is similar to experimental observations of EBR-II fuel. The qualitative agreement between experimental and simulated observations lends support to the addition of this low-temperature swelling model. However, further experimental investigations of the local phase and temperature should be performed to determine if another mechanism could also account for these structures. Other investigations can help reduce the uncertainty in the rate of the porosity formation with respect to burnup and temperature for different U-Pu-Zr fuel compositions.

Bibliography

[1] Gerard L Hofman, RG Pahl, CE Lahm, and DL Porter. Swelling behavior of u-pu-zr fuel. *Metallurgical Transactions A*, 21(2):517–528, 1990.

[2] RD Leggett, TK Bierlein, and B Mastel. Irradiation behavior of high purity uranium. Technical Report HW-79559, Hanford Laboratories, 1963.

[3] SH Paine and JH Kittel. Preliminary analysis of fission-induced dimensional changes in single crystals of uranium. Technical Report ANL-5676, Argonne National Laboratory, 1958.

[4] J Lehmann, P Paoli, and N Azam. Etude du gonflement d'alliages d'uranium sous irradiation. *Journal of Nuclear Materials*, 27(3):285–309, 1968.

[5] WR McDonell, GR Caskey, and CL Angerman. High-performance uranium-metal fuels for savannah river reactors. In *Proceedings of the Symposium: 50 Years of Excellence in Science and Engineering at the Savannah River Site*, 2000.

[6] JH kittel and LR Kelman. Effects of irradiation on some uranium-plutonium alloys. Technical Report ANL-5706, Argonne National Laboratory, 1958.

[7] Gerard L Hofman. *Metallic Fuels*, pages 1–53. Wiley, 2015.

[8] WJ Carmack, DL Porter, YI Chang, SL Hayes, MK Meyer, DE Burkes, CB Lee, T Mizuno, F Delage, and J Somers. Metallic fuels for advanced reactors. *Journal of Nuclear Materials*, 392(2):139–150, 2009.

[9] KF Smith. Irradiation of uranium-fissium alloys and related compositions. Technical Report ANL-5736, Argonne National Laboratory, 1957.

[10] KF Smith and LR Kelman. Irradiation of cast uranium-plutonium base alloys. Technical Report ANL-5677, Argonne National Laboratory, 1957.

[11] RW Bohl and MV Nevitt. A study of uranium-fissium alloys containing technetium. Technical Report ANL-6495, Argonne National Laboratory, 1962.

[12] JH Kittel, JA Horak, WN Beck, and RJ Fousekt. Irradiation behavior of uranium-fissium alloys. Technical Report ANL-6795, Argonne National Laboratory, 1971.

[13] JH Kittel, JE Ayer, WN Beck, MB Brodsky, DR O'Boyle, ST Zegler, FH Ellinger, WN Miner, FW Schonfeld, and RD Nelson. Plutonium and plutonium alloys as nuclear fuel materials. *Nuclear Engineering and Design*, 15:373–440, 1971.

Chapter 5

Implement Lower Length Scale Informed Swelling Model for Metallic Fuel

B. W. Beeler

A new model for volumetric swelling in U-Pu-Zr fuels, `UPuZrGaseousEigenstrain`, was developed and merged to Bison, which computes a volumetric strain to account for gaseous swelling in U-Pu-Zr metal fuel systems with input from a lower length scale calculation. This report documents that effort and constitutes completion of the NEAMS FY19 milestone titled "Implement lower length scale informed swelling model for metallic fuel".

5.1 Gaseous Swelling

The derivation for the fuel swelling model for U-Pu-Zr used here was originally presented in [1]. The model is able to simplify the gaseous swelling porosity into an analytical solution by making the following assumptions:

- Fission gas diffusivity is infinite so that all fission gas is born in the bubbles
- The number density of bubbles is constant and their size perfectly spherical
- The gas within the bubbles can be treated as an ideal gas
- The gas/vacancy ratio in the bubbles is in equilibrium, i.e. the bubbles are not over- or under-pressurized
- Re-solution of fission gas atoms from the bubbles is neglected
- The solid is assumed to be un-stressed

Following these assumptions, the number of gas atoms in each bubble A_b at some time $t+\Delta t$ can be calculated directly from the total number of fissions,

$$A_b(t+\Delta t) = A_b(t) + \frac{Y_{gas}\bar{F}}{N_b}(1-A_r)(1-I(p)) \tag{5.1}$$

where Y_{gas} is the yield of gas atoms per fission, N_b is the number density of bubbles (bub/m^3), A_r is a fixed constant representing the amount of fission gas retained in the solid, and $\bar{F}$ is the average number of fissions between t and $t+\Delta t$,

$$\bar{F} = 0.5 * \left[\dot{F}(t) + \dot{F}(t+\Delta t)\right]\Delta t, \tag{5.2}$$

where $\dot{F}$ is the fission rate density.

Also included in 7.12 is the impact of interconnectivity of the bubbles I on the total number of gas atoms per bubble. In the absence of a mechanistically informed interconnection model, the total bubble interconnection can be estimated from the porosity by,

$$I(p) = \frac{p_{term} - p(t)}{p_{term} - p_{init}} \tag{5.3}$$

where p_{init} and p_{term} is the interconnection initiating and terminating porosity respectively, and p is the bulk porosity at time t. p_{init} and p_{term} can be set via the input parameters `interconnection_initiating_porosity` and `interconnection_terminating_porosity`. 7.14 ensures a linear transition of interconnection from 0 to 1.0, capturing the smooth transition from non-interconnected to fully interconnected porosity.

The bubble radius can be simply calculated as a function of the total number of fissions,

$$R = \sqrt{\frac{3k_B T Y_{gas} \dot{F} t}{4\pi 2\gamma N}}, \tag{5.4}$$

where k_B is the Boltzmann constant, T is the temperature (K), $\gamma = 0.8$ is the surface tension of the fuel (J/m^2) [2], $Y_{gas} = 0.3017$ is the gaseous fission product yield, $\dot{F}$ is the fission rate density, t is time, and N is the number density of bubbles (bubbles/m^3).

Given the radius, the total eigenstrain can be calculated as,

$$\left(\frac{\Delta V}{V_0}\right)_g = \frac{4\pi}{3} R^3 N \tag{5.5}$$

Several checks are performed on the value calculated by [eq:swelling], ensuring that swelling due to gas bubbles only increases, and is not larger than the maximum permissible swelling calculated from p_{term},

$$\left(\frac{\Delta V}{V_0}\right)_g^{max} = \frac{p_{term} - p_{initial}}{1 - (p_{term} - p_{initial})} \tag{5.6}$$

where $p_{initial}$ is some initial porosity, e.g. fabrication porosity.

The porosity due to gas can be calculated from the swelling eigenstrain as,

$$p_{gas} = \frac{\left(\frac{\Delta V}{V_0}\right)_g}{1 + \left(\frac{\Delta V}{V_0}\right)_g}, \tag{5.7}$$

and the total porosity can then be calculated from the gaseous eigenstrain as,

$$p = p_{initial} + p_{gas}. \tag{5.8}$$

Finally, the input parameter `anisotropic_factor` can be optionally specified between 1 and -1 to preferentially apply the volumetric strain in either the x and y directions in 3D meshes, or in the radial and axial dimensions in 2DZ geometry. The factor is applied such that the trace of the volumetric swelling is the same as purely isotropic swelling, but preferential in particular dimensions:

$$\varepsilon_{ij} = \left(\frac{\Delta V}{V_0}\right)_g \begin{bmatrix} 1+f & 0 & 0 \\ 0 & 1-f & 0 \\ 0 & 0 & 1 \end{bmatrix} \tag{5.9}$$

5.2 Lower Length Scale Connection

The goal of this work was to incorporate information from lower length scale calculations into the engineering scale model. A candidate for this multi-scale information transfer is the surface tension in the fuel, γ in Equation 5.4

5.2.1 Historical

The surface energy utilized in Bison models was tracked back in the literature to a paper by Tsuboi [3]. This manuscript utilized the value of 0.8 J/m^2, without reference and without justification, simply stating that this was the value that was used. Subsequently, this value was utilized as the surface tension for metallic fuel.

5.3 Surface Tension via Molecular Dynamics

There is a UZr interatomic potential capable of describing a number of properties of gamma UZr [4]. By investigating voids, one can approximate the average surface energy (tension) of a given system. The systems we investigated range from bcc U to bcc Zr, with a number of intermediate concentrations, from 1000 K to 1300 K. Surface energy of U-10Zr (23 atomic percent) is about 1.5 J/m^2 over the temperature range investigated. This is approximately 2X the previous historical value. This was met with skepticism of the applicability of the potential to surface systems So, we advanced the technical sophistication to *ab initio* molecular dynamics (AIMD) simulations that would not rely on an interatomic potential. Figure 5.1 shows a representation of the molecular dynamics void calculation and Figure 5.2 shows surface energy (tension) as a function atomic percent Zr at various temperatures.

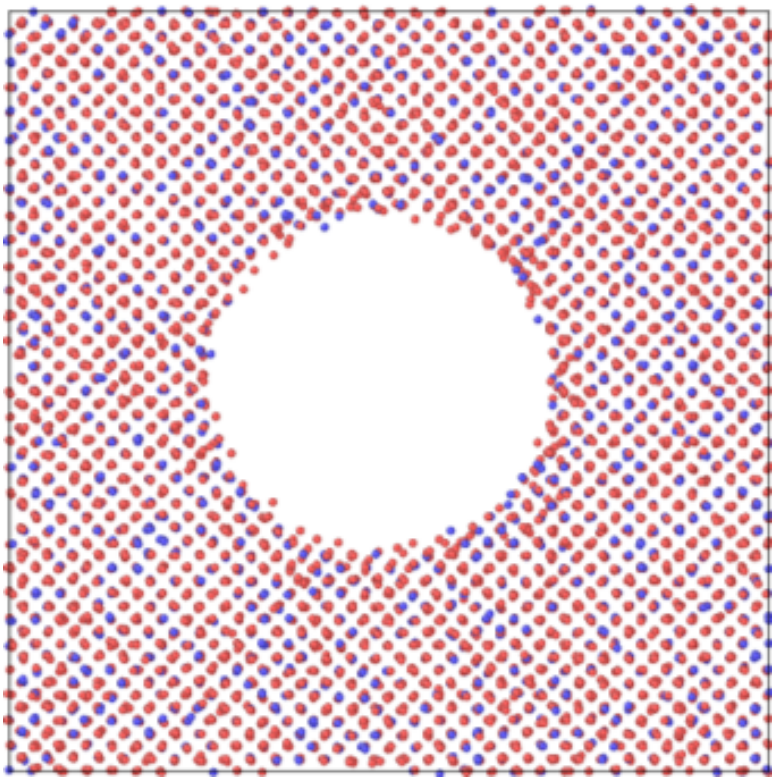

Figure 5.1: An example void in U-10Zr at 1200 K. The void is approximately 3 nm in diameter.

5.4 *Ab Initio* Molecular Dynamics (AIMD)

AIMD is significantly more computationally expensive than classical MD simulations, restricting the system size to about 128 atoms (compared to about 50,000 atoms for classical MD). As such, investigating voids is unrealistic and untenable, restricting investigations to planar surfaces. First, one must determine the equilibrium volume and energy at the given temperatures of interest. Figures 5.3 and 5.4 show energy per atom and lattice constant of equilibrated systems of bcc UZr at 1200 K. The calculations to generate these simple little charts took about 200k cpu-hrs. This provides a basis to investigate surfaces.

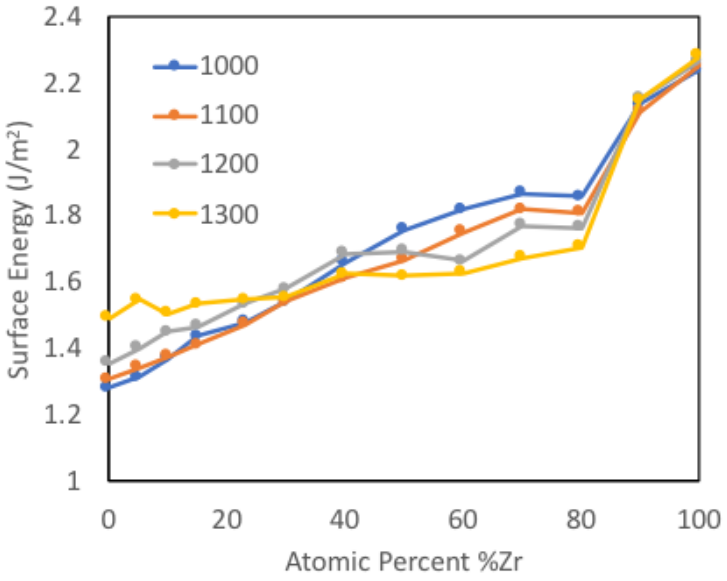

Figure 5.2: Surface energy as a function of atomic percent Zr for temperatures from 1000 K up to 1300 K.

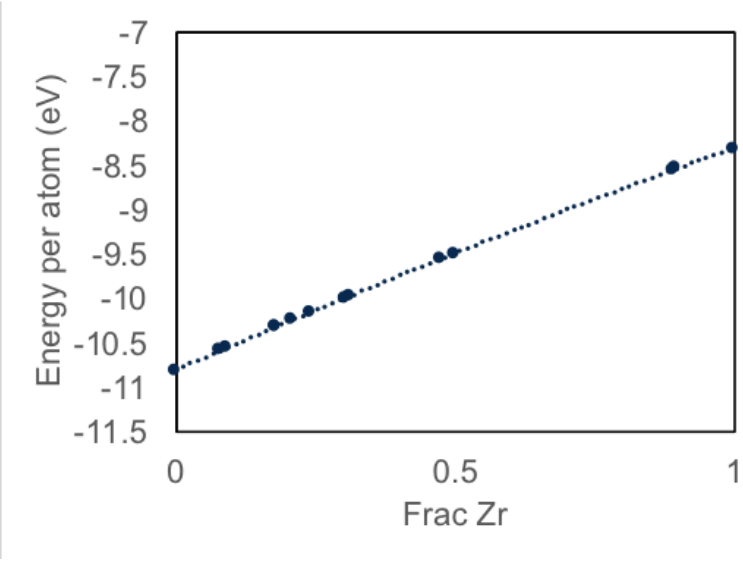

Figure 5.3: Energy per atom of UZr alloys at 1200 K as a function of Zr content.

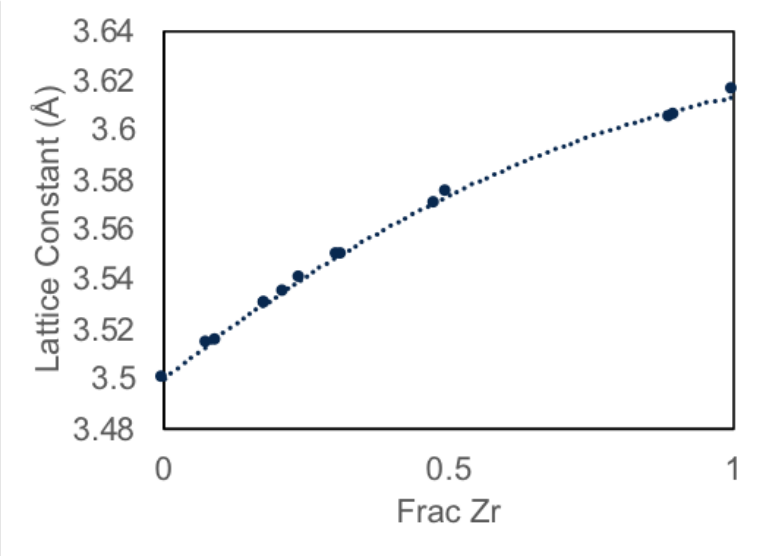

Figure 5.4: Lattice constant of UZr alloys at 1200 K as a function of Zr content.

5.5 AIMD Surfaces

This work investigated the (100) (Fig. 5.5) and (110) (Fig. 5.6) surfaces in bcc UZr. For each composition, we utilized two unique surfaces. This is likely insufficient for accurate statistics, as each individual surface is comprised of at most 25 atoms. Surface energies range from 1.71 J/m^2 to 2.04 J/m^2, in the region of U-10Zr, values are approximately 1.75 J/m^2. These are two unique surfaces, but do not represent an average, and so can compare MD (100) and (110) surfaces to extrapolate to an average surface energy. For MD surfaces, surface energies for (100) and (110) range from 1.4 to 1.7 for U-7Mo to U-30Mo (void average of 1.5 J/m^2). Thus, it is expected that these surfaces are near-average, and a value of 1.75 J/m^2 can be used at 1200 K. The full scope of compositions at 1200 K are shown in Fig. 5.7.

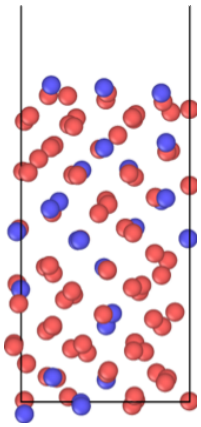

Figure 5.5: Example of a (100) surface in U-10Zr from an AIMD simulation.

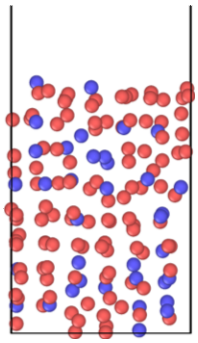

Figure 5.6: Example of a (110) surface in U-10Zr from an AIMD simulation.

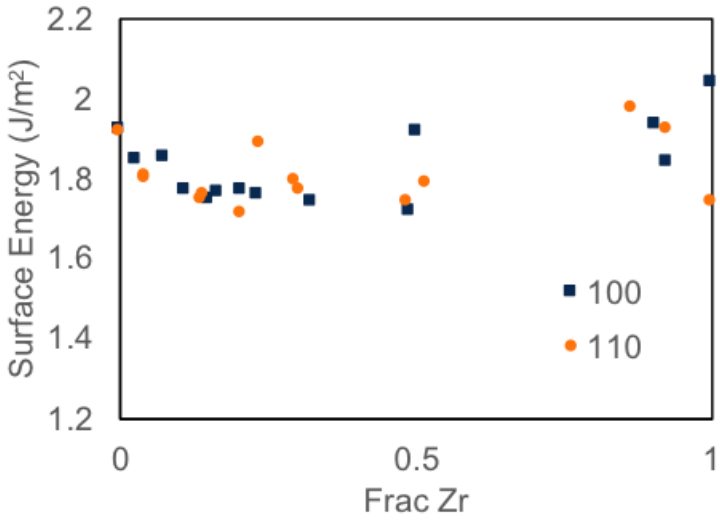

Figure 5.7: Surface energy of UZr at 1200K as a function of Zr content.

5.6 Extension to other Temperatures

This work is on-going, and therefore will continue throughout the year. We've obtained (100) and (110) surface energies for most compositions 1100 K and 1300 K, but these numbers still being refined. There exists a slight trend toward increasing surface energy with increasing temperature, but this trend is not quite statistically significant, due to the pronounced scatter in the data. It seems likely that a surface energy between 1.5 and 2.0 J/m^2 will be applicable over the entire composition and temperature range of relevance. Current results at 1100 K and 1300 K are shown in Figs. 5.8 and 5.9.

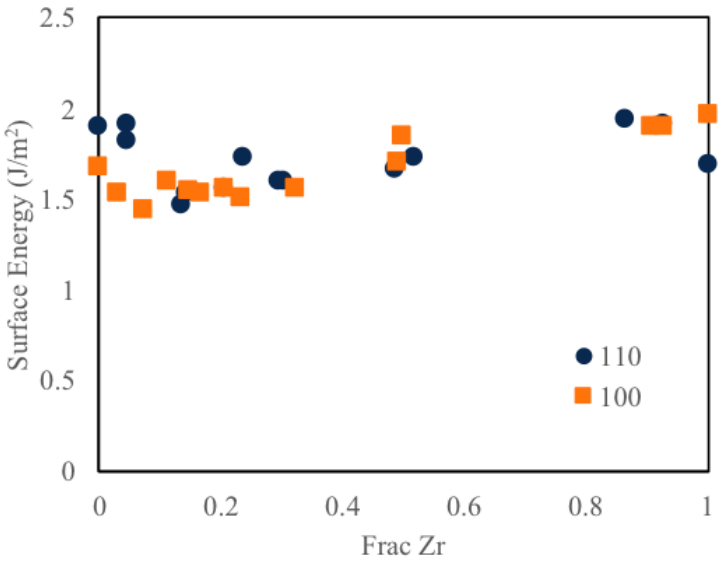

Figure 5.8: Surface energy of UZr at 1100K as a function of Zr content.

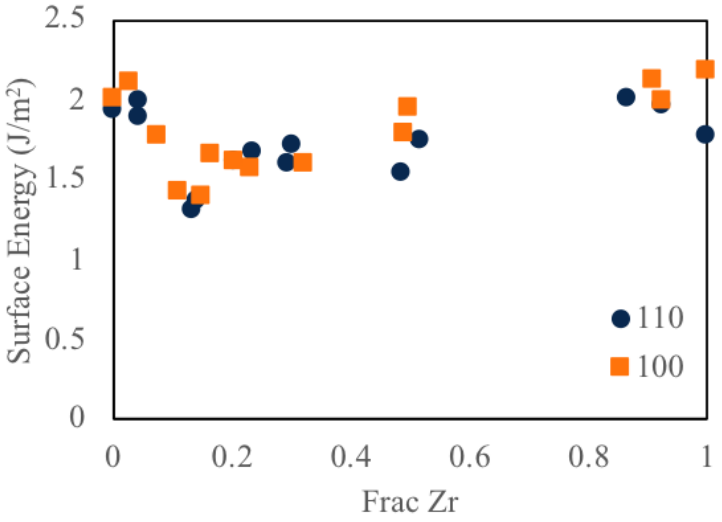

Figure 5.9: Surface energy of UZr at 1300K as a function of Zr content.

5.7 Summary

The historical value for surface energy seems to be without an experimental or modeling basis. Molecular dynamics simulations of voids in UZr point to an average surface energy of 1.5 J/m^2. *Ab initio* molecular dynamics calculations point to a slightly higher value for surface energy, approximately 1.75 J/m^2. These updated values can be utilized in the MARMOT and Bison swelling models.

Figure 5.10 shows the effect of fuel surface tension on fission gas release for a given value of the number of bubbles per volume, N = 1e20. As mentioned in a previous section of this report, the fission gas release predictions in Bison are more sensitive to changes in the fuel surface tension (γ) than with the number of bubbles per volume (N). Therefore, establishing a "best estimate" for the fuel surface tension parameter should be a high priority for improving the metallic fuel modeling capability in Bison.

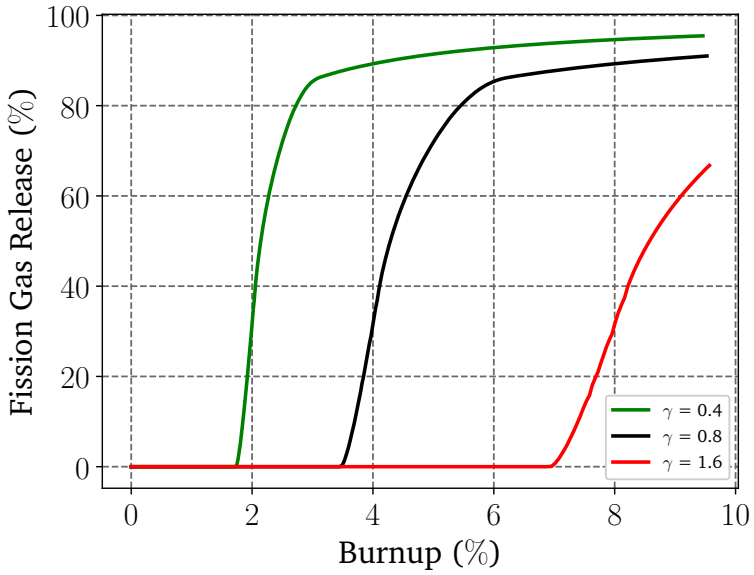

Figure 5.10: Comparison of fission gas release as a function of fuel surface tension.

Bibliography

[1] D.R.Olander. *Fundamental aspects of nuclear reactor fuel elements*. Technical Information Center, Energy Research and Development Administration, 1976.

[2] Aydin Karahan. *Modeling of thermo-mechanical and irradiation behavior of metallic and oxide fuels for sodium fast reactors*. PhD thesis, Massachusetts Institute of Technology, June 2009.

[3] Y. Tsuboi, T. Ogata, M. Kinoshita, and H. Saito. Mechanistic model of fission gas behavior in metallic fuel. *J. Nucl. Mater.*, 188:312, 1992.

[4] A. Moore, B. Beeler, C. Deo, M. Baskes, and M. Okuniewski. Atomistic modeling of high temperature uranium-zirconium alloy structure and thermodynamics. *J. Nucl. Mater.*, 467:802, 2015.

Chapter 6

Implement Diffusional Eutectic Melting FCCI Model for Metallic Fuel

A. M. Jokisaari

6.1 Introduction

A new model for fuel-clad chemical interaction (FCCI) for U-Pu-Zr fuels based on diffusional transport of material has been developed via lower length scale efforts and has been implemented into Bison; the implementation is scheduled to be merged in early FY20. The model, which takes the form of an auxiliary kernel, `DiffusionalEutecticThicknessFCCI`, replaces the existing `EutecticThicknessFCCI` auxiliary kernel. Both models predict the thickness of a penetration layer resulting from the presence of a low-temperature U-Fe eutectic in the phase diagram; as time above the eutectic temperature increases, the melt layer (or penetration) thickness increases. The major difference between the new model and the existing model is that the new model predicts a non-linear penetration rate that is inversely proportional to the square root of time, while the existing model assumes a constant penetration rate. Details of the model are described in the companion FY19 lower length scale milestone document; this section covers the Bison implementation only.

6.2 Model and Bison discretization

For a temperature, T, greater than the U-Fe eutectic temperature, $T_e = 998$ K, the new eutectic thickness model predicts a penetration depth, D, of eutectic liquid as a result of fuel-cladding chemical interaction as

$$D(t) = R\sqrt{t}, \tag{6.1}$$

where t is time and R is a constant for a given temperature in Kelvin. Note that this model assumes a constant temperature.

The Bison implementation must handle non-constant temperature histories. For example, the local temperature may be less than T_e for some time before increasing above T_e; or the local temperature may decrease below T_e after some time above T_e. The temperature may also vary while $T > T_e$. To handle these cases, the Bison model transforms Eq. 6.1 into an incremental form. The equation for the penetration depth is discretized as

$$D(t_n) = \theta_{n-1}\Delta t + D(t_{n-1}), \tag{6.2}$$

where n is the current time step, $n-1$ is the previous time step, Δt is the time step increment, and $theta$ is the rate of change of the layer thickness. The equation for θ is given as

$$\theta = \frac{\partial D}{\partial t} = \frac{R}{2\sqrt{t_e}}, \tag{6.3}$$

where t_e is the amount of time that $T \geq T_e$, found by summing the time step increments over which T is continuously greater than or equal to T_e, unless the time step is the first in which $T \geq T_e$. In that case, $t_e = \Delta t/2$. If the temperature has

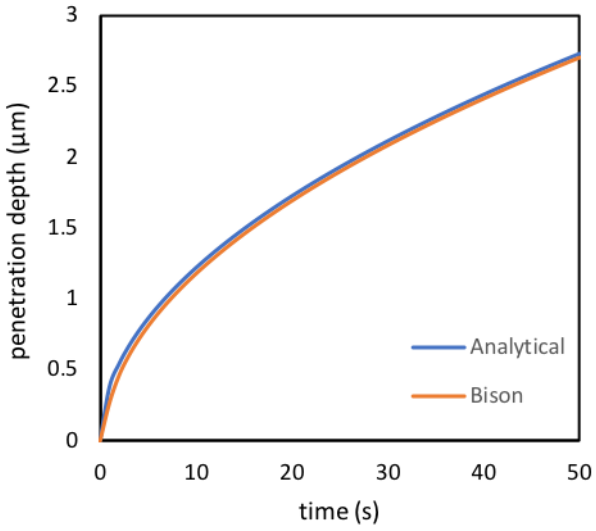

Figure 6.1: Comparison of the penetration layer thickness at 1000 K calculated by the analytical model (Eq. 6.1) and the Bison implementation.

been above T_e and then drops below T_e, it is assumed that solidification occurs instantaneously and the layer thickness and t_e are both returned to zero. The value of R is calculated for the given temperature at the current time step, the details of which are described in the companion lower length scale milestone document. In the Bison implementation, it is assumed that this will not affect the correctness of the results; however, the next iteration of the model will include a derivation incorporating the effect of non-constant temperature.

6.3 Comparison of Bison implementation results to analytical model

In this comparison, the results predicted from the analytical model in Eq. 6.1 are compared to the results calculated with the Bison implementation for constant temperatures. Figure 6.1 shows the results for 1000 K, barely above the eutectic temperature, while Fig. 6.2 show the results for 1400 K, barely below the melting temperature of uranium (1405 K). The discretization scheme is chosen to reduce the error at longer times at the expense of underpredicting the thickness of the layer at the first time step, which is the time at which the layer is thinnest. The error at the first time step is approximately 29%, but rapidly decreases to less than 2% and continues to decrease to under 1%. Comparison of the model to experimental data is found in the companion lower length scale milestone document.

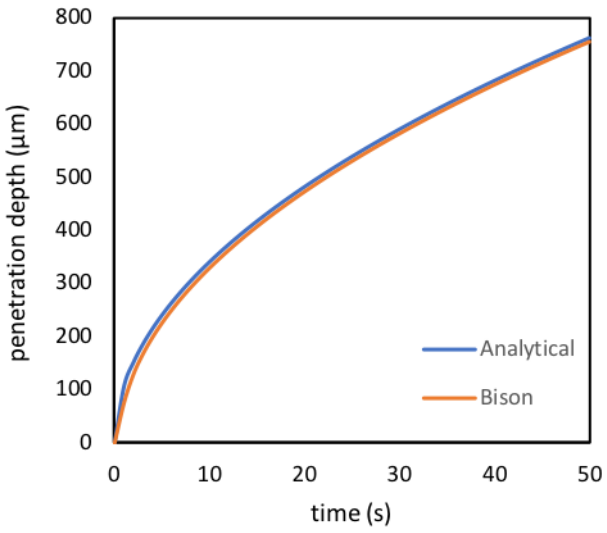

Figure 6.2: Comparison of the penetration layer thickness at 1400 K calculated by the analytical model (Eq. 6.1) and the Bison implementation.

Chapter 7

Metallic Fuel Validation Plan

A. Casagranda
S. R. Novascone
A. X. Zabriskie

The purpose of this manuscript is to show examples of our recent assessment efforts, and more importantly, document our metallic fuel validation plan for Bison. We start with a brief history of the EBR-II reactor where the majority of metallic fuel operating experience and research was conducted. We also discuss the highest-priority modeling needs for future commercial metallic fast reactors and the experimental testing facility, the Versatile Test Reactor (VTR).

An initial Bison metallic fuel assessment case based on the EBR-II X441 experiment is described next. The physics included in this assessment as well as the simplifying assumptions that were made are detailed. In addition, a comparison of the Bison results with experimental data is presented to illustrate the areas where Bison is in good agreement with the data and where additional research and development is needed.

Finally, an overall plan to validate the Bison metallic fuel modeling capability is presented. The plan describes validation needs for the currently implemented Bison models as well as the process to be applied to models implemented in the future. A subset of the overall validation plan will be selected as a focus for FY20. The FY20 plan will demonstrate the general model validation process on the highest priority Bison features for both commercial reactor and the VTR designs.

7.1 Metallic Fuel Background

7.2 EBR-II operational history

The Experimental Breeder Reactor program operated for approximately 30 years (1964–1994) and accomplished several important objectives related to sodium cooled fast reactors and metallic fuels [1, 2]. The first goal of EBR-II was to demonstrate that a closed fuel cycle was possible. This meant that the reactor would generate power while breeding fissionable plutonium from U-238. In addition, the fuel would be reprocessed, re-fabricated and reinserted into the reactor for additional power production. All of these processes were performed on-site thus eliminating the need for transportation of radioactive materials off-site or requiring fresh fuel to be delivered. This goal was achieved in 1969 at which point $\sim 35,000$ fuel pins had gone through these steps successfully.

Following the closed fuel cycle demonstration, EBR-II was used for several years as the main research and development facility for fast reactor fuels and materials. Over this time the metallic fuel composition and design as well as the cladding materials and geometry were varied in order to achieve higher burnups without cladding failures. Eventually, burnups of $\sim 20\%$ were reached in EBR-II using a U–Pu–Zr fuel combined with HT9 cladding. A number of experiments were performed during this time which measured fuel and cladding deformations, fission gas production and release, fuel cladding chemical interaction as well as post-irradiation examination of the fuel microstructure. This data is a valuable source for validating fuel performance modeling codes and, perhaps more importantly, serves as a guide for those looking to design advanced reactors.

In the final years of EBR-II operation, the reactor was utilized to establish the feasibility of the Integral Fast Reactor (IFR) concept. EBR-II was used to demonstrate the commercial viability of the IFR design and experiments

were performed to highlight the inherent safety of metallic fuels. In 1986 both a loss of flow and a loss of heat sink accident were conducted at EBR-II. During both accidents no operator intervention was required and the reactor passively shut down. Despite the excellent operational history of EBR-II and demonstrated intrinsic safety, the EBR program was canceled in 1994 and the reactor was shutdown.

Since that time, the United States has not developed a fast flux test facility to support advanced fast reactor commercial concepts currently being pursued. The Versatile Test Reactor (VTR) project aims to address this need by designing and building a fast reactor capable of providing both a fast and thermal flux environment for testing fuel, cladding and coolant materials for proposed reactor designs [3]. The Bison software will play an important role in predicting fuel performance as the plan for VTR, and other metallic fuel vendors, such as Oklo, evolves.

7.3 New Fast Reactor Validation Needs

Although there are several new fast reactor designs being proposed, the Bison validation effort will not be focused on a specific reactor and instead will attempt to be more widely applicable to all the proposed designs. A common concern is the primary barrier to fission product release, i.e., the cladding. Several concerns have been identified including availability, qualification, compatibility and consistency of material behavior with legacy data. Therefore, some designs have not made a final decision on the cladding material and are considering multiple choices.

Metallic fuel behavior is extremely complex and a number of phenomenon have not been fully understood. The EBR-II experimental data spans a wide range of fuel compositions and operating conditions. However, since the main goal of EBR-II was to achieve high fuel burnup, fundamental studies of the phenomena occurring was not a top priority. Therefore, in many cases, "engineered solutions" were used to address the limiting behavior with regards to burnup and more basic research of the phenomena was not pursued.

The currently proposed fast reactor designs typically use a U-yZr or U-xPu-yZr fuel composition. The common issues with these classes of metallic fuel are swelling, anisotropic deformation, Zr redistribution and phase changes, as well as chemical compatibility with the cladding. The priority for validating the Bison models for these phenomena will depend on both the safety importance of the behavior as well as the maturity of model implementation.

7.4 Initial Bison metallic fuel assessment

Primarily due to the limited amount of metallic fuel fast reactor measurements, and applicability to advanced reactor concepts, the focus of our early validation efforts have been and will continue to be the EBR-II program. The focus of these experiments was to establish requirements for running metallic fast fuel to high burnup and qualifying a fuel and cladding combination. As such, measurements of operating conditions is somewhat limited, as is post-irradiation examination of fuel and cladding. This fact limits comparisons between measurements and calculations to cladding strain, fuel elongation, and constituent redistribution.

To begin our assessment and establish a baseline for future validation calculations we decided to focus on experiment X441. We did some preliminary assessment of experiment X441 in FY18, but the purpose of revisiting X441 in FY19 was to study variations in fuel pin geometry and the corresponding effect on cladding strain. Figure 7.1 summarizes these experiments. Models were based on "as-designed" geometry with the following simplifying assumptions, which are imposed to achieve robust convergence and focus on the effects of geometry changes on cladding strain.

1. Constant power history
2. Constant fuel-cladding gap thermal conductance
3. No Zr redistribution in the fuel
4. Frictionless contact between fuel and cladding

The Figures 7.2, 7.3, and 7.4 show results from simulations of a subset of the experiments listed in Figure 7.1. These figures essentially show the effect of geometric variations in plenum to fuel volume ratio, smear density, and clad thickness on cladding strain measurements along with the effect of Zr content.

X441 Experimental Parameters

Group	Plenum/Fuel (Vol. Ratio)	Zr content (w/o)	Smear Density (% TD)	Clad Material	Clad Thickness (mils)
A	1.5	10	75	HT9	15
B	2.1	10	75	HT9	15
C	1.1	10	75	HT9	15
D	1.5	6	75	HT9	15
E	1.5	14	75	HT9	15
F	1.5	10	85	HT9	15
G	1.5	10	70	HT9	15
H	1.5	10	75	HT9	18

Figure 7.1: X441 experimental groups

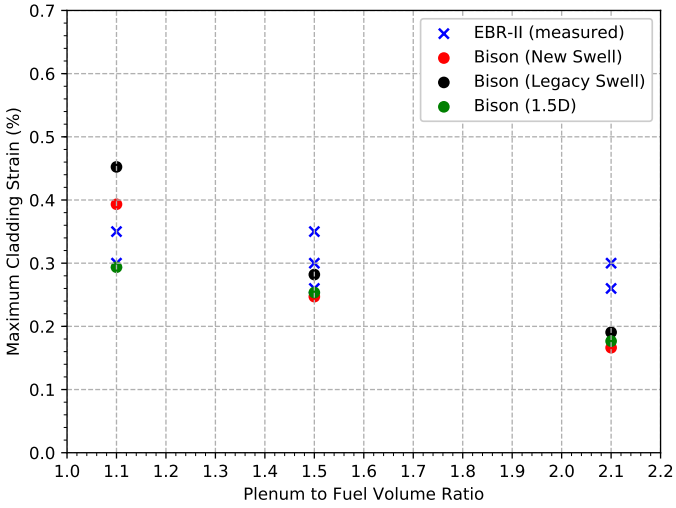

Figure 7.2: Maximum cladding strain vs. plenum to fuel volume ratio for a variety of Bison models and measurements from EBR-II. See Appendix A 7.13 for more information about new and legacy swelling models.

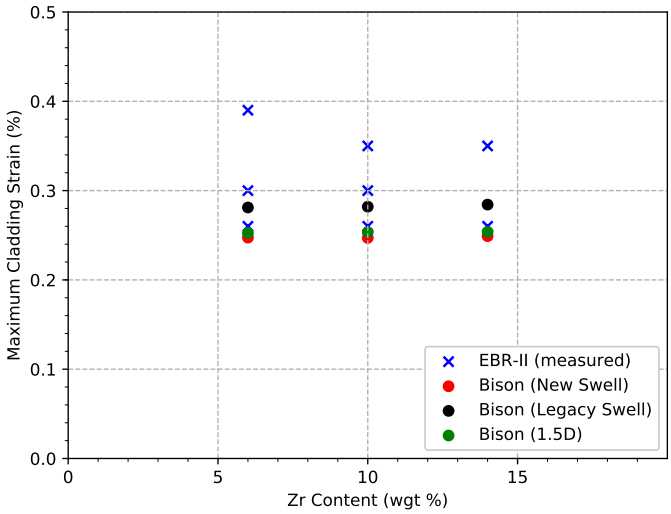

Figure 7.3: Maximum cladding strain vs. zirconium content for a variety of Bison models and measurements from EBR-II. See Appendix A 7.13 for more information about new and legacy swelling models.

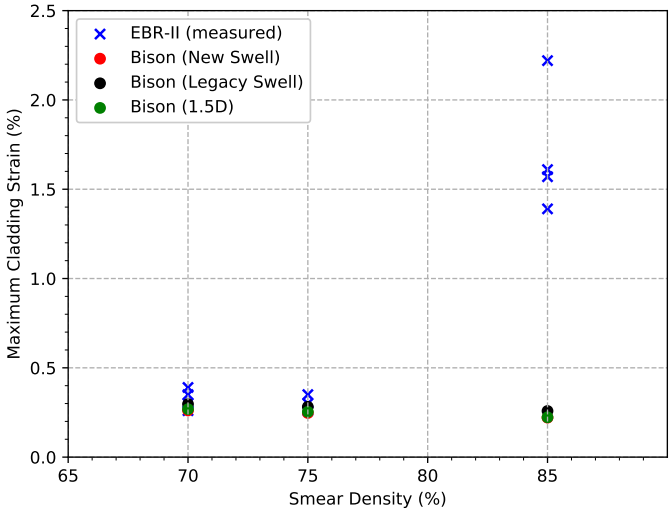

Figure 7.4: Maximum cladding strain vs. smear density for a variety of Bison models and measurements from EBR-II. See Appendix A 7.13 for more information about new and legacy swelling models.

7.5 Additional Case

With success in modeling X441, EBR-II's X512 experiment, also named OPT-1 [4], was chosen as a purely transient case to model testing transient capability. Only pin DP-55 was chosen to be modeled as an additional case. DP-55 was initially irradiated during X441. OPT-1 began with a 24 hour preconditioning phase at constant power followed by a ramp for about 5 minutes, before shutting down the reactor.

Initial conditions for a Bison model of OPT-1 were taken, as much as possible, from published post irradiation examination (PIE) data. The Bison OPT-1 model simulates a preconditioning phase followed by a transient ramp ending with a SCRAM. A 2D-RZ geometry fuel pin with a closed gap in glued contact served as the mesh for OPT-1. Heat transfer, tensor mechanics, and zirconium redistribution were all coupled with two-way feedback between all three equations. Fuel material properties depended on temperature and zirconium concentration. Cladding material properties depend on temperature.

The preconditioning phase served to stabilize temperature and zirconium concentration profiles in the fuel before the transient began.It was unknown before running a simulation if OPT-1's transient would affect the zirconium distribution. A side-by-side comparison of the pre-transient and peak transient zirconium profiles are presented in figure 7.5 with the radial axis scaled $20\times$. No noticeable effects in zirconium concentration occurred. As such, zirconium redistribution physics may be ignored during a transient comparable to OPT-1, though a correct initial profile is desirable to have proper material properties for a transient.

As each pin was not instrumented directly during the X512 EBR-II run, only COBRA calculated data for each pin is available for comparison. COBRA tabulated data [5] for DP-55 is compared to Bison's results in figure 7.6 with good agreement. No input parameters were calibrated to any results, as the Bison case was meant to be predictive just like the COBRA analysis was.

While results presented from these cases demonstrate that Bison can be used for metallic fuel calculations due to the generally favorable comparisons, it's clear that progress on model development and more detailed assessment relative to data sets like EBR-II are required. For example, Bison calculations tend to deviate from measurements when the strain in the cladding is high, as is the case for low plenum to fuel volume ratio and high smear density.

From our discussions with fuel experts, who worked on EBR-II and now work on the VTR program [6], it's apparent that the highest priority for a metallic fuel performance code is to accurately model steady-state and transient cladding mechanical performance. This requires accurate material models in both the fuel and cladding. In the following sections, we describe our plan for model development and assessment to meet our goal of demonstrating the foundation for metallic fuel validation and design calculations.

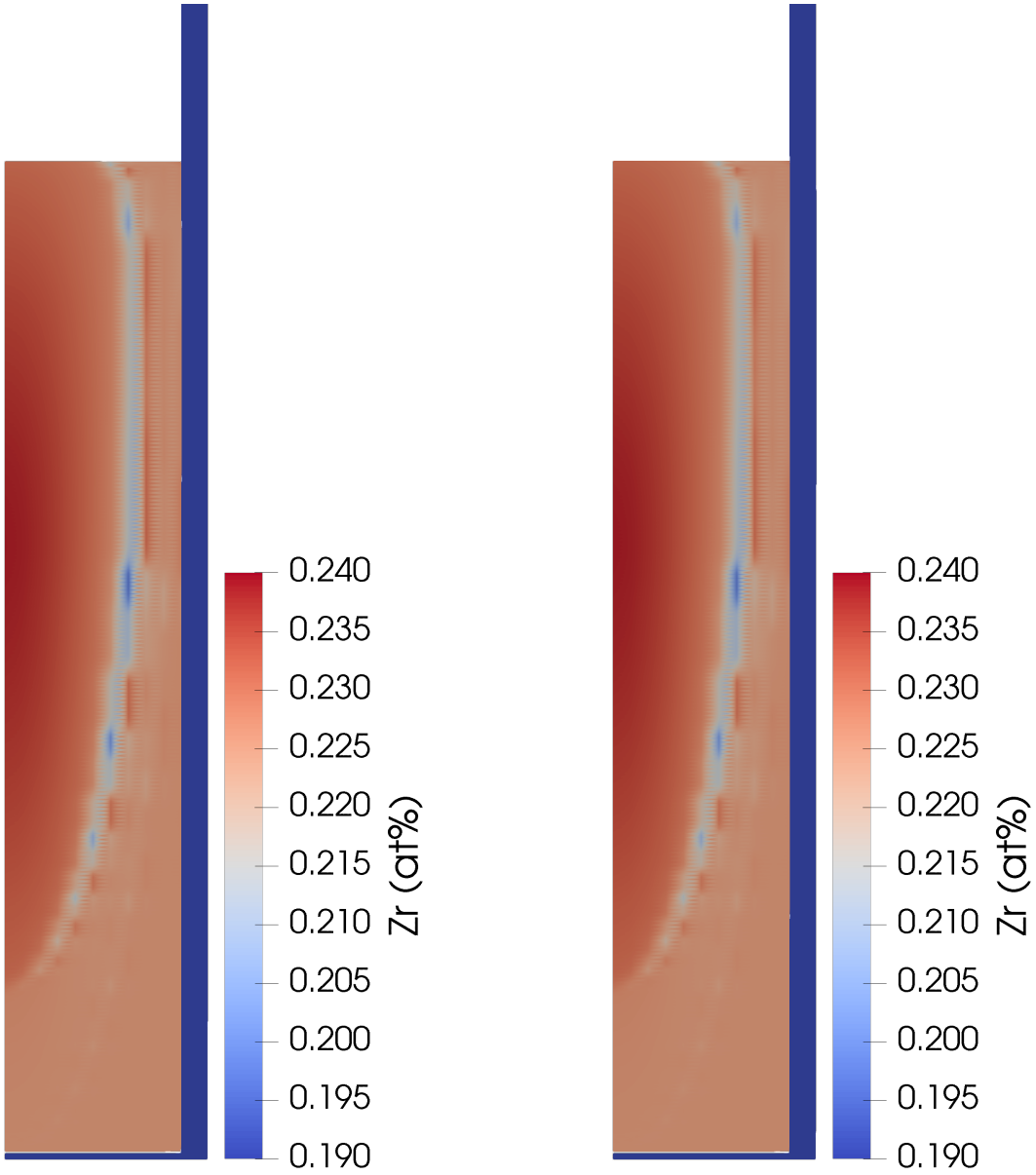

(a) (b)

Figure 7.5: No change in zirconium distribution from 24 hour preconditioning profile (a) to transient peak profile (b).

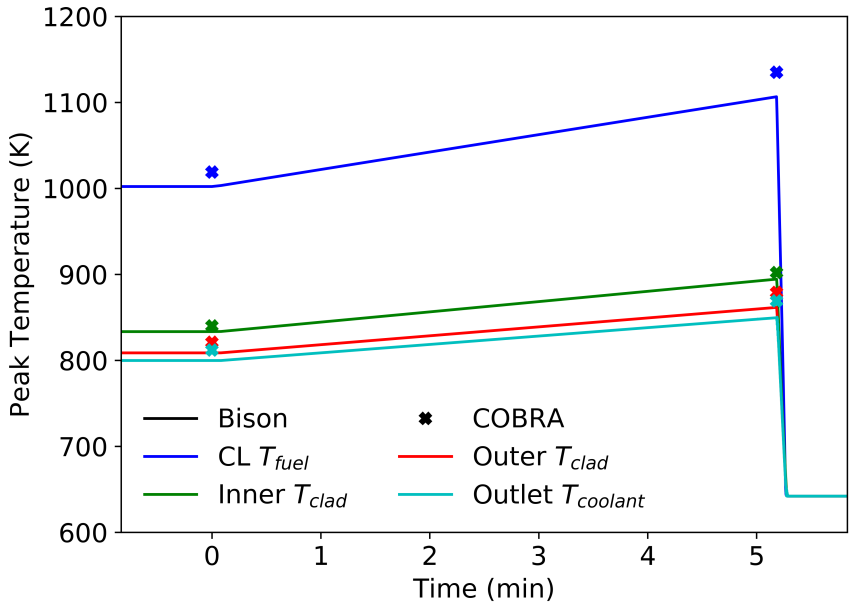

Figure 7.6: Peak temperature comparison of COBRA and Bison for OPT-1.

7.6 Validation

Our definition of validation is: A body of work built from simulating a wide variety of metallic fuel experiments and comparing to corresponding measurements that exhaustively accounts for uncertainty in the data and modeling approaches. We plan to achieve this by developing models that include the relevant physics, materials, and boundary conditions to compare with simulations of experiments from EBR-II, the Fast Flux Test Facility (FFTF), and for transients, TREAT. We feel this establishes a strong assessment foundation that can be used by other programs, such as Advanced Fuels Campaign (AFC) for advanced model development and VTR for validation and design calculations.

The material models for metallic fuels are complex and generally depend on composition, porosity, temperature and irradiation. Models implemented in Bison are described in more detail in Appendix A 7.13 and generally originate from the IFR Metallic Fuel Handbook [7]. As a higher-level, quick reference, Table 7.1 lists the physics and model parameters that we've identified as important to our overall assessment effort. The current default parameter values in the models are based on the original development of the model and the specific data and/or other codes that the model used to establish the defaults. It has been observed that those defaults do not provide good predictions for EBR-II experimental data (e.g., fission gas release). Figure 7.7 shows a comparison of the Bison fission gas release predictions using the default parameter values and a set of "curve fitted" parameters with the EBR-II experimental data. As mentioned, the default values do not match the experimental data very well. However, the "curve fitted" results are in good agreement with this single set of experimental data. A more general calibration of the model would require optimizing the parameter values for a wider range of experimental data (i.e., composition, smear density, etc...). Therefore, a rational approach for calibrating the models and validating them to the existing EBR-II data is proposed here.

Table 7.1: Physics and Model Parameters

Physics	**Model Parameters**
Fuel Elasticity	P, Porosity W_{Pu}, Plutonium weight fraction W_{Zr}, Zirconium weight fraction β_E, Degradation factor (E) β_p, Degradation factor (ν)
Fuel Creep	P, Porosity Q_i, Activation energies n, Stress exponent A_i, Material constants
Fuel Thermal Conductivity	W_{Pu}, Plutonium weight fraction W_{Zr}, Zirconium weight fraction
Fuel Volumetric Swelling	N, Bubble number density γ, Surface tension f, Anisotropic factor
Clad Creep	Q_i, Activation energies n, Stress exponent C_i, Material constants

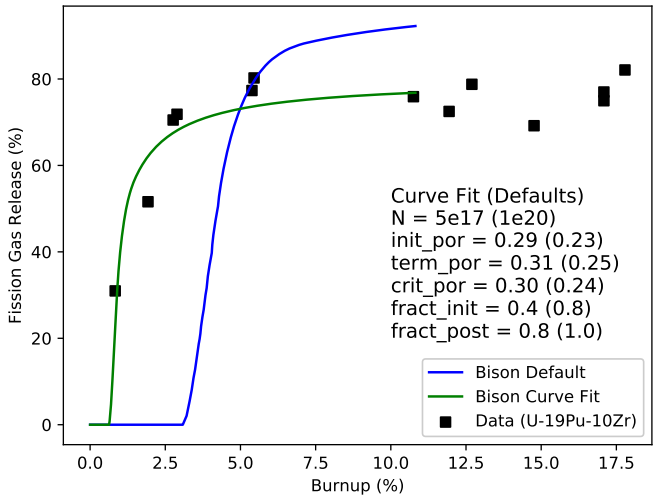

Figure 7.7: Comparison of the Bison default parameters and the results of a curve fit to EBR-II experimental data.

The way we choose to evaluate material models is to identify model inputs and conduct a sensitivity study. A sensitivity analysis using a tool such as the Dakota [8] software to determine the relative importance of each input is necessary to establish the baseline behavior of the model. This sensitivity study may be repeated in the future as subsequent physics models are calibrated. In addition, the sensitivity study provides feedback to experimental efforts designed to measure the most important material properties.

The next step involves identifying the best current set of experimental data related to the physics being investigated that spans a range of the most sensitive model inputs determined in the sensitivity study. This data set will then be used to calibrate the model over the widest range of conditions possible and test the robustness of the model.

The final step consists of using the calibrated model on a fuel pin or cladding-only simulation to determine the improvement of the Bison predictions from the default to the calibrated parameters on a more complex analysis. A standard set of output quantities for metallic fuel assessments will be established and used to evaluate Bison results over time. An initial partial list of output quantities is provided below as an example, which may be further expanded as required.

- Standard output for metallic fuel rods (similar to LWR standard outputs)
  - Fission gas release
  - Fuel elongation
  - Fuel radial/axial strain
  - Cladding radial displacements for full length of rod
  - Maximum cladding and/or fuel temperature
  - Profile of cladding and/or fuel centerline, fuel exterior and clad exterior temperature

While the material models documented in the IFR Metallic Fuel Handbook [7] are a good start for Bison, as part of the assessment/validation effort, we plan to incorporate models from other sources and evaluate all of these models via comparison to experiment measurement. For example, the Mark-V Safety Analysis report [9] and Nuclear Systems Materials Handbook (NSMH) [10] contains alternate material models we can use and compare with those from the IFR Metallic Fuel Handbook. We plan to further extend this broader evaluation of Bison to code-to-code comparisons with other metallic fuel codes, such as LIFE-Metal [11, 12, 13], Alfus [14, 15], MACSIS [16], SESAME [17] and possibly others. Where applicable, results from these alternate material models and codes will be shown along side Bison calculations using the IFR Metallic Fuel Handbook material models.

The notion of validating a fuel performance code for advanced reactors is best viewed as an emerging process that we expect to change as we progress. We will embrace these changes as we become more experienced in applying our methods and material models and, of course, as new information comes to light. With that in mind, we believe the assessment/validation direction described here is appropriate.

The effort required to perform this process on all the metallic fuel models in Bison is much greater than could be completed in a single fiscal year. Therefore, a subset of the physics described in the table above will be examined in FY20. A more detailed plan of the specific steps related to Bison metal fuel validation for FY20 is shown in the following sections.

7.7 Assessment focus for FY20

Here, we describe the specific assessments for FY20. We propose to assess cladding mechanical performance in isolation (separate effects tests) and fuel swelling behavior from the integrated fuel pins.

Regarding cladding, historically, in light water reactor fuel performance calculations, we've used cumulative damage index (CDI) to determine cladding performance limit. This approach relies on having a large statistical database. In the absence of this large database, as is the case for cladding used in metallic fuel, we plan to use results from separate effects measurements and simulations to establish a bound on cladding strain for steady-state and transient conditions. With focus on lower length scale-informed modeling, this effort will include advancing the state of cladding mechanical properties and models with documentation of the corresponding impact on cladding strain limit calculations. VTR personnel have expressed interest in this, and we plan to proceed with their feedback. A cladding strain limit of 1% for HT9 was proposed as a result of the EBR-II experiments [9]. We feel this was conservative and we plan to re-examine this strain limit in FY20. The list below outlines the specific cladding related modeling categories and the proposed model calibration and validation work.

1. Cladding Elastic-Plastic Behavior
   (a) Separate Effects Data - unirradiated & irradiated
   (b) Parameter study on yield stress, hardening modulus, K, n
2. Cladding Creep Behavior
   (a) Separate Effects Data - unirradiated & irradiated
   (b) Parameter study on activation energies, stress exponents, other material constants
3. Cladding Burst Testing
   (a) Develop assessment cases

Despite recent progress in numerical stability and the inclusion of more physical phenomena, current models in Bison continue to underestimate fuel swelling. It's important to accurately predict swelling, porosity interconnection (fission gas release), and cladding wastage due to fuel-cladding chemical interaction. The timing and combined effect of these phenomena impact cladding mechanical performance. In other words, the duration of cladding exposure to increased plenum pressure and contact with the fuel decreases the amount of time cladding will maintain its intended structural function. By applying lessons learned from prior years of model development and our increasing familiarity with EBR-II data, we plan to calibrate parameters in current models to duplicate EBR-II measurements and demonstrate this in multiple assessment cases. Furthermore, we plan to leverage lower-length scale knowledge and models to enable engineering scale model updates and defend model calibration. The list below provides the fuel related physics to be studied in FY20 and the proposed Bison activities.

1. Anisotropic Fuel Swelling
   (a) EBR-II Data - X423 Experiment
   (b) Parameter study on anisotropic_factor
2. Fission Gas Release

(a) EBR-II Data - Various Experiments

(b) Parameter study on swelling and fission gas release model inputs

3. EBR-II Assessment Cases

(a) Compare default and "calibrated" model parameter results

In the following sections, we describe our assessment approach by discussing separate effects experiments for the cladding and fuel swelling calibration. in Appendix B 7.14 we describe our approach for extracting and prioritizing the available EBR-II data for this assessment. Also note that a subset of experiments will be used for calibration and the remaining experiments are to be used for evaluation.

7.8 Separate Effects Experiments & Modeling

A focus of the validation effort should be on identifying experimental results that isolate specific material behavior (e.g., elastic-plastic, creep, swelling, mass diffusion, etc...) and utilize them to develop assessment cases. In many instances, the development of models based on in-reactor measurements or post-irradiation examination data can be misleading especially when the behavior has both an irradiation and non-irradiation component. The complexity of material response in an irradiation environment and lack of experimental data can lead to calibration of model parameters to a limited data set which may not be predictive.

The non-irradiation behavior of the material should be modeled and validated before addressing the irradiation component of the material behavior. The advantage of this approach is that the non-irradiation behavior, which is usually less complex, can always be easily obtained by setting the power and/or neutron flux to zero. This separation of non-irradiation and irradiation components of material behavior will also make it easier to debug issues that may arise related to material convergence or when comparing code predictions to experimental results.

7.9 Unirradiated CW SS316 elastic-plastic mechanical behavior - example

As an demonstration of both using experimental data to calibrate Bison and the use of a separate effects experiment, the following example is provided. The motivation for this effort was to include the elastic-plastic mechanical behavior of CW SS316 in a Bison cladding burst test to help improve the comparison of the Bison results with experimental data. Initially, only the creep behavior of the SS316 material was modeled in the burst test and the Bison predictions for cladding failure did not agree well with the data.

After a literature search for mechanical testing of SS316 in both irradiated and unirradiated conditions was made, several references were found [18, 19, 20, 21]. The first set of experiments to be modeled [18] used a relatively simple tensile testing method and specimen geometry (Figure 7.8). The testing was performed on both irradiated and unirradiated specimens of SS316 (irradiated in EBR-II at 375°C) at the irradiation temperature. The engineering stress-strain curves for the CW SS316 material is shown in Figure 7.9.

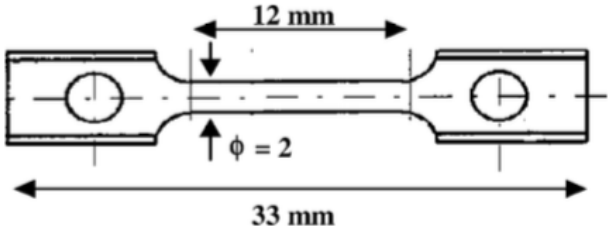

Figure 7.8: Cylindrical tensile test specimen geometry

A Bison model was developed to simulate the tensile test from this study. The tensile specimen mesh is shown in Figure 7.10. The appropriate boundary conditions were applied for symmetry since only one-quarter of the specimen is modeled. In addition, a displacement BC was applied at the top of the specimen to simulate the loading in the experiment. Figure 7.11 shows a contour plot of the total strain in the axial direction at the end of the simulation.

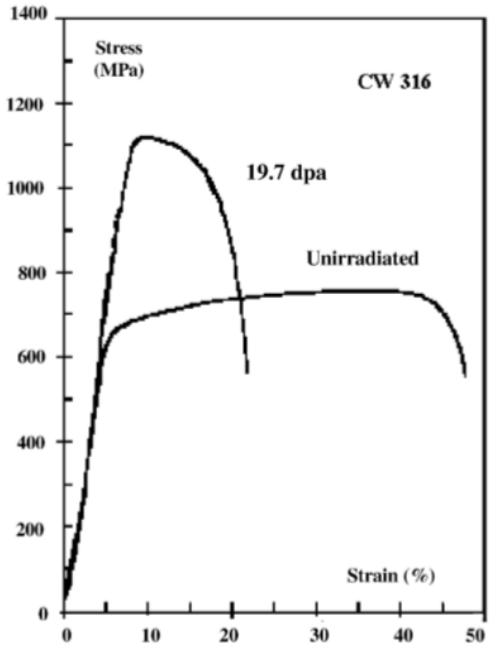

Figure 7.9: Engineering stress-strain data for CW 316 tested at 375°C [18]

It can be seen that near the center of the specimen "necking" is observed, which generally means that yielding has occurred and the deformation has localized. The engineering stress-strain prediction from Bison compared to the data (Figure 7.12) shows the onset of yielding, strain hardening and finally necking behavior. The agreement between Bison and the experimental data is reasonably good.

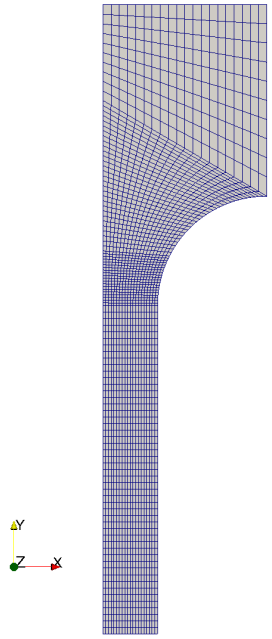

Figure 7.10: Bison tensile test specimen mesh

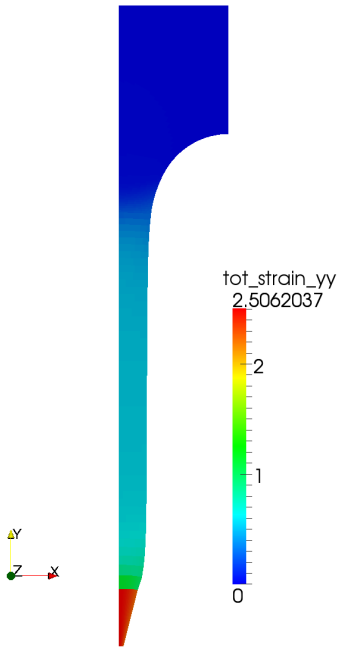

Figure 7.11: Total strain in axial direction at end of Bison simulation

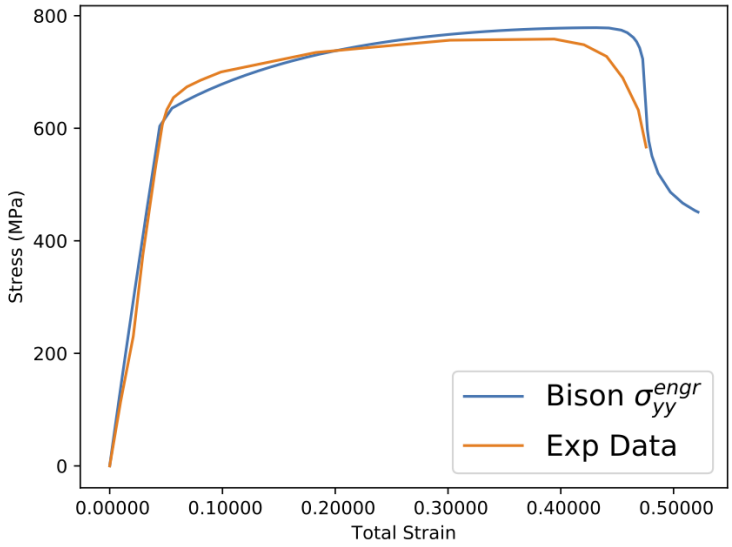

Figure 7.12: Engineering stress-strain results from Bison simulation

7.10 Fuel swelling parameter calibration plans

In our estimation, one of the most important models is fuel swelling, where porosity generation, pore interconnection, and subsequent fission gas release are modeled. In this section, we list the physical phenomena, the experiment that best sheds light on this phenomena, and model parameters that we plan to calibrate.

As a further example of the simple "curve fitting" process possible with any code (see section 7.6), the `anisotropic_factor` will be used to calibrate the Bison prediction of axial to radial strain (from fuel swelling) as a function of burnup to a single set of EBR-II experimental data. The X423 EBR-II experiment provides measurements of the axial to radial strain for a U-10Zr fuel up to a burnup of $\sim 2\%$. The experimental data and a set of Bison results are presented in Figure 7.13. As can be seen, the prediction of axial to radial strain with the default model parameters is rather poor compared to the X423 data. However, as the `anisotropic_factor` is increased from the default value of zero to 0.4, the Bison prediction improves. Unfortunately, using this simple approach, the effects of this change on other "quantities of interest" is not known and the optimal value of the `anisotropic_factor` might also change as additional data for other fuel compositions is considered. Therefore, the approach described in section 7.6 and outlined below is required to have a robust validation of Bison.

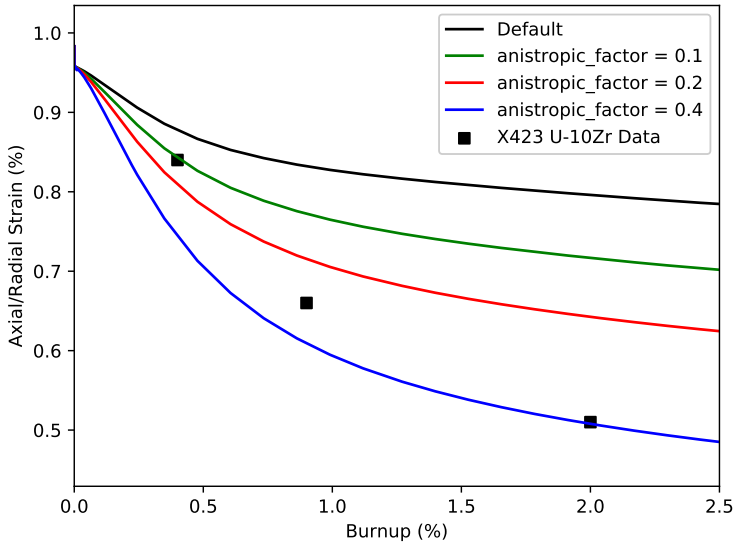

Figure 7.13: Comparison of experimental data and Bison predictions for axial to radial strain as a function of burnup

The steps for calibrating the metallic fuel material model parameters will involve an iterative process. For example, once a set of EBR-II experiments for fission gas release are collected and the relevant parameters for that behavior have been calibrated, subsequent calibrations of other models should involve checking that the fission gas release calibration has not been changed. The steps outlined below describe such a process. Note, specific experiments that highlight certain physics (fuel swelling and restructuring) and materials (U-10Zr) are listed in Appendix B 7.14.

- Calibrate metallic fission gas release model parameters
  - Select range of experimental data to use in calibration
    - Fuel composition, smear density, fuel/plenum ratio, etc...
  - Extract experimental data, create CSV file and setup plotting script
  - Calibrate model parameters to subsets of data (e.g., composition)
- Calibrate metallic anisotropic swelling model

- Select range of experimental data to use in calibration
- Extract experimental data, create CSV file and setup plotting script
- Calibrate model parameters to data
- Check fission gas release results with new anisotropic swelling parameters

7.11 Road blocks

In developing this plan, we've encountered a few obstacles worth noting. For example, there's a discrepancy between power history listed in the IMIS database and that listed by Argonne in the FIPD database; we must reach consensus on model inputs. Another potential issue that will influence the ability to accurately compare Bison predictions with experimental data is the assumptions currently being made in the initial Bison assessment models. The list is reproduced below for reference.

1. Constant power history
2. Constant fuel-cladding gap thermal conductance
3. No Zr redistribution in the fuel
4. Frictionless contact between fuel and cladding

Eliminating the currently-used assumptions in the X441 assessment will probably require more than a single FY to accomplish. In addition, once these assumptions are removed, the subsequent effect on solution convergence and model stability might be detrimental. The "downstream" effects will need to be determined and if necessary addressed; for example, representing physical factors that are sensitive to transients in power. As the FY20 planning is finalized, a subset of the above assumptions could be targeted for elimination depending on their significance and the resources available.

7.12 Summary of FY20 plan

- Arrive at consensus for model inputs
- Separate effects simulations on EBR-II cladding materials
- Establish a strain-based failure criteria for use with VTR design calculations ($\sim 2\%$)
- Swelling parameter calibration
- Run a number of EBR-II/FFTF/TREAT fuel pins with updated models for cladding and fuel swelling and compare to prior calculations and measurements to demonstrate success of approach
- Quantify uncertainty and identify sensitive physical properties
- Apply this approach to material models from other sources (NSMH)
- Present results alongside results from other metallic fuel codes (LIFE-Metal)

7.13 Appendix A - Material model details

Here we show the equations for some of the models we plan to focus on in FY20. For a complete model description, see the online documentation at bison.inl.gov.

7.13.1 Fuel Elasticity Model

The Young's modulus correlation can be derived using data from U-11Pu-6.3Zr cast fuel as:

$$E = E_u(1-\beta_E P)\left(\frac{1+0.17W_{Zr}}{1+1.34W_{Zr}} - W_{Pu}\right) \left(1-1.06\left[\frac{T-588}{T_{mu}}\right]\right) \tag{7.1}$$

where E_u = 1.6 $\times$ 10^5 MPa is the Young's modulus for pure uranium at the reference temperature of 588 K, P is the fractional porosity, W_{Zr} is the zirconium weight fraction, W_{Pu} is the plutonium weight fraction, T is the temperature in K and T_{mu} = 1405 K is the melting temperature of pure uranium. β_E is the Young's modulus degradation factor due to porosity and is typically 1.2.

The correlation for Poisson's ratio can be derived from the U-Zr correlation as:

$$\nu = \nu_u(1-\beta_p P)\left(\frac{1+3.4W_{Zr}}{1+1.9W_{Zr}}\right)\left(1+1.2\left[\frac{T-588}{T_{mu}}\right]\right) \tag{7.2}$$

where ν_u = 0.24 is the Poisson's ratio of pure uranium at the reference temperature of 588 K. β_p is the Poisson's ratio degradation factor due to porosity and is typically 0.8.

7.13.2 Fuel Creep Model

A model for the combined thermal and irradiation creep of UPuZr fast reactor fuel is available with the creep rate modeled as a function of time, fuel porosity, effective stress and fission rate. The constitutive relation is taken from [22] and is given as

$$\begin{aligned}\dot{\varepsilon} &= A_1\left(1+7.9p+470p^2\right)exp\left(\frac{-Q_1}{RT}\right)\sigma \\ &+ A_2\left(1-p^{0.67}\right)^{-4.5}exp\left(\frac{-Q_2}{RT}\right)\sigma^{4.5} \\ &+ A_3\dot{F}\sigma\end{aligned} \tag{7.3}$$

where $\dot{\varepsilon}$ is the creep rate (1/s), σ is the effective (Mises) stress in MPa, T is the temperature in K, p is the porosity, $\dot{F}$ is the volumetric fission rate (fissions/cm^3-s), Q_i are the activation energies (cal/mol), R is the universal gas constant (1.987 cal/mol-K) and A_{1-3} are material constants given as $A_1 = 5\times10^3$, A_2 = 6 and $A_3 = 7.7\times10^{-23}$.

The first term in equation 7.3 represents diffusional creep, the second term represents power law creep and the third term represents irradiation creep as it depends upon the fission rate. The activation energies for the thermal creep terms (Q_1 and Q_2) are given as $Q_1 = Q_2 = 52000$ cal/mol.

These U and Pu alloys have a phase change temperature of 923.15 K. Above this temperature, the creep rate equation changes to

$$\dot{\varepsilon} = A_4\left(1-p^{0.67}\right)^{-3}exp\left(\frac{-Q_3}{RT}\right)\sigma^3 + A_3\dot{F}\sigma \tag{7.4}$$

where A_4 is 8.0×10^{-2} and Q_3 is 28500 cal/mol.

7.13.3 Fuel Thermal Conductivity Model

The fuel thermal conductivity model is based on correlations for each constituent in the fuel. The thermal conductivity of the ternary fuel is given as

$$\begin{aligned}k_{U-Pu-Zr} &= (1-\sqrt{1-w_{pu}})k_{Pu} \\ &+ \sqrt{1-w_{Pu}}[(1-w_{Pu})k_{U-Zr} + w_{Pu}k_{c,Pu}]\end{aligned} \tag{7.5}$$

where w_{Pu} is the weight fraction of plutonium in the fuel and the U-Zr binary thermal conductivity is calculated by

$$\begin{aligned} k_{U-Zr} = &(1-\sqrt{1-f_{Zr}})k_{Zr} \\ &+\sqrt{1-f_{Zr}}(f_{Zr}k_{c,U-Zr}+(1-f_{Zr})k_U) \end{aligned} \tag{7.6}$$

and the adjusted weight fraction of zirconium for the binary formulations is given as

$$f_{Zr} = \frac{w_{Zr}}{w_{Zr}+w_U} \tag{7.7}$$

The correction term for the U-Zr binary is

$$k_{c,U-Zr} = f(f_{Zr}, T) \tag{7.8}$$

and the plutonium thermal conductivity correction is

$$k_{c,Pu} = f(w_{Pu}, T) \tag{7.9}$$

and the thermal conductivity correlations in W/m-K for U (k_U), Pu (k_{Pu}) and Zr (k_{Zr}) are given as simple functions of temperature.

7.13.4 Fuel Volumetric Swelling Model

The class in Bison called UPuZrVolumetricSwellingEigenstrain (Legacy in figures 7.2, 7.3, and 7.4).) model is based on a derivation originally described elsewhere [23]. The model is based on the mechanical force balance for an equilibrium fission gas bubble given as:

$$p = \frac{2\gamma}{r_b} - \sigma_h + \sigma_{cr} \tag{7.10}$$

where p is the pressure of the fission gas in a bubble, γ is the surface tension of the fuel, r_b is the fission gas bubble size, σ_h is the hydrostatic stress in the fuel and σ_{cr} is the creep strength stress of the fuel. Assuming that the gas in the bubble is governed by the ideal gas law and rearranging to solve for the volume of the bubble leads to an expression for the volumetric strain due to swelling as:

$$\left(\frac{\Delta V}{V_0}\right)_g = \frac{3.59\times10^{-24}FT}{1.01\times10^7-\sigma_h} \tag{7.11}$$

where T is the temperature in Kelvin, F is in fission/m^3 and σ_h is in Pa.

In FY19, a new gaseous swelling model was implemented called UPuZrGaseousEigenstrain (New in figures 7.2, 7.3, and 7.4). The new model computes a volumetric strain to account for gaseous swelling in UPuZr metal fuel. The derivation for the fuel swelling model for UPuZr used here was originally presented in [24]. The model is able to simplify the gaseous swelling porosity into an analytical solution by making the following assumptions:

- Fission gas diffusivity is infinite so that all fission gas is born in the bubbles
- The number density of bubbles is constant and their size perfectly spherical
- The gas within the bubbles can be treated as an ideal gas
- The gas/vacancy ratio in the bubbles is in equilibrium, i.e. the bubbles are not over- or under-pressurized
- Re-solution of fission gas atoms from the bubbles is neglected
- The solid is assumed to be un-stressed

Following these assumptions, the number of gas atoms in each bubble A_b at some time $t+\Delta t$ can be calculated directly from the total number of fissions,

$$A_b(t+\Delta t) = A_b(t) + \frac{Y_{gas}\bar{F}}{N_b}(1-A_r)(1-I(p)) \tag{7.12}$$

where Y_{gas} is the yield of gas atoms per fission, N_b is the number density of bubbles (bub/m^3), A_r is a fixed constant representing the amount of fission gas retained in the solid, and $\bar{F}$ is the average number of fissions between t and $t+\Delta t$,

$$\bar{F} = 0.5 * \left[\dot{F}(t) + \dot{F}(t+\Delta t)\right] \Delta t, \tag{7.13}$$

where $\dot{F}$ is the fission rate density.

Also included in 7.12 is the impact of interconnectivity of the bubbles I on the total number of gas atoms per bubble. In the absence of a mechanistically informed interconnection model, the total bubble interconnection can be estimated from the porosity by,

$$I(p) = \frac{p_{term} - p(t)}{p_{term} - p_{init}} \tag{7.14}$$

where p_{init} and p_{term} is the interconnection initiating and terminating porosity respectively, and p is the bulk porosity at time t. p_{init} and p_{term} can be set via the input parameters interconnection_initiating_porosity and interconnection_terminating_porosity. Equation 7.14 ensures a linear transition of interconnection from 0 to 1.0, capturing the smooth transition from non-interconnected to fully interconnected porosity.

The bubble radius can be simply calculated as a function of the total number of fissions,

$$R = \sqrt{\frac{3k_B T Y_{gas} \dot{F} t}{4\pi 2\gamma N}}, \tag{7.15}$$

where k_B is the Boltzmann constant, T is the temperature (K), $\gamma = 0.8$ is the surface tension of the fuel (J/m^2) [25], $Y_{gas} = 0.3017$ is the gaseous fission product yield, $\dot{F}$ is the fission rate density, t is time, and N is the number density of bubbles (bubbles/m^3).

Given the radius, the total eigenstrain can be calculated as,

$$\left(\frac{\Delta V}{V_0}\right)_g = \frac{4\pi}{3} R^3 N \tag{7.16}$$

Several checks are performed on the value calculated by 7.16, ensuring that swelling due to gas bubbles only increases, and is not larger than the maximum permissible swelling calculated from p_{term},

$$\left(\frac{\Delta V}{V_0}\right)_g^{max} = \frac{p_{term} - p_{initial}}{1 - (p_{term} - p_{initial})} \tag{7.17}$$

where $p_{initial}$ is some initial porosity, e.g. fabrication porosity.

The porosity due to gas can be calculated from the swelling eigenstrain as,

$$p_{gas} = \frac{\left(\frac{\Delta V}{V_0}\right)_g}{1 + \left(\frac{\Delta V}{V_0}\right)_g}, \tag{7.18}$$

and the total porosity can then be calculated from the gaseous eigenstrain as,

$$p = p_{initial} + p_{gas}. \tag{7.19}$$

Finally, the input parameter anisotropic_factor can be optionally specified between 1 and -1 to preferentially apply the volumetric strain in either the x and y directions in 3D meshes, or in the radial and axial dimensions in 2DR geometry. The factor is applied such that the trace of the volumetric swelling is the same as purely isotropic swelling, but preferential in particular dimensions:

$$\varepsilon_{ij} = \left(\frac{\Delta V}{V_0}\right)_g \begin{bmatrix} 1+f & 0 & 0 \\ 0 & 1-f & 0 \\ 0 & 0 & 1 \end{bmatrix} \tag{7.20}$$

7.13.5 Clad Creep Model

The thermal and irradiation creep of HT9 clad material is taken from [7] in which the first two terms are for secondary thermal creep and the last term represents the irradiation creep contribution [26].

$$\dot{\varepsilon}_{cr} = C_5 \exp(-\frac{Q_4}{RT})\bar{\sigma}^2 + C_6 \exp(-\frac{Q_5}{RT})\bar{\sigma}^5 + [B + A\exp(-\frac{Q}{RT})]\phi\bar{\sigma}^{1.3} \tag{7.21}$$

where T is the temperature (K), σ is the effective stress (MPa), ϕ is the neutron flux (n/cm^2-s) and $\dot{\varepsilon}_{cr}$ is the effective thermal and irradiation creep strain rate ($1/s$). Table 7.2 lists the creep coefficients and activation energies for equation 7.21.

Table 7.2: Parameters used in the HT9 Creep Model.

Parameter	**Value**
A	2.59×10^{14}
B	1.83×10^{-4}
C_5	1.17×10^{9}
C_6	8.33×10^{9}
Q	73000 (cal/mol)
Q_4	83142 (cal/mol)
Q_5	108276 (Cal/mol)

7.14 Appendix B - EBR-II Data Extraction

In this appendix, a sampling of the type of experimental data available in the EBR-II database is presented. A consistent process for extracting the data from the database and/or publications will be developed in FY20. This process will include the following steps:

1. Identify the source of the data
   (a) EBR-II database directory, filename and page
   (b) Publication reference and figure/table number
2. Extract the data using consistent format and units (CSV and SI units)
3. Add the data to the Bison repository
   (a) Consistent location (directory and naming)
   (b) Provide an example for using the data and/or plotting it (Matplotlib)

The following is a grouping of EBR-II related citations in the general categories listed below. In addition, Table 7.3 shows specific phenomena and materials tested in various EBR-II experiments.

- Axial fuel growth, FGR, cladding deformation [27]
- Wastage [28]
- Tube burst testing [29, 30, 31]
- Zr Redistribution [32]
- HT-9 Cladding [33, 34, 26, 35]
- Fuel swelling [36]

Table 7.3: Physics matched with specific experiments/pins

Physics	Material	Experiment
Fuel swelling and restructuring	U-10Zr	X423
Cladding failure	HT9 and U-10Zr	X447/X430
Anisotropic fuel swelling	U-xPu-yZr	X419/X423/X425
Fission gas release	U-xPu-yZr	X419/X423/X425
Sodium infiltration	U-xPu-yZr	X430

The EBR-II database contains a large collection of PDF files with legacy experimental data from various EBR-II fuel rod experiments. After searching through these documents several times, Table 7.4 has been created to provide a listing of the files and information to be extracted as time permits. Table 7.4 is considered a "living" document that will be added to and used to track the progress of extracting relevant EBR-II experimental data.

Table 7.4: EBR-II Data Extraction Listing

Exp Folder	File Name	Page (s)	Data to Extract
X419	Post-Irradiation exam of IFR.pdf	4,10, 38	Fuel length changes, FGR data for pins T-012 and T-193, Zr redistribution data for pin T-197
X419	Post-irradiation exam.pdf	3-4,15-16,17-24	Axial and Volume strain as func of Pu content, FGR, Zr redistribution for 2 different Pu contents
X419	GASR data for 5 el.pdf	all	FGR data (plenum pressure and volume)
X419a	GASR data.pdf	all	FGR data (plenum pressure and volume)
X419b	Laser Axial Profilometry.pdf	all	Cladding diameter profiles as function of axial length
X419b	Plenum Vol. and Press. retransmittal.pdf	all	FGR data (plenum pressure and volume)
X423	Report Determination of temp and phase dist etc....pdf		Axial power distribution, porosity distribution, phase distribution by pin
X423	GASR*.pdf		FGR data (plenum pressure and volume)
X423b	GASR*.pdf		FGR data (plenum pressure and volume)
X425	Post-Irradiation Exam.pdf		FGR, Zr redistribution, fuel strains
X425b	Safety Package for continued irradiation.pdf		Biaxial stress rupture data for HT9 and CW 316SS, presentation materials w/possible data
X425b	Element contact profilometry 18 el.pdf		Cladding profile traces
X425b	Contact profilometry 43 el.pdf		Cladding profile traces
X425c	Contact profilometry 18 el.pdf, Contact profilometry 43 el.pdf		Cladding profile traces
X427	GASR*.pdf		FGR data (plenum pressure and volume)
X430	Sodium infiltration into fuel.pdf		Na infiltration data

Bibliography

[1] L. C. Walters. Thirty years of fuels and materials information from EBR-II. *Journal of Nuclear Materials*, 270:39–48, 1999.

[2] J. I. Sackett. Operating and test experience with EBR-II, the IFR prototype. *Progress in Nuclear Energy*, 31:111–129, 1997.

[3] S. Sen, G. Youinou, M. Salvatores, G. Palmiotti, P. Finck, and C. Davis. A Versatile Coupled Test Reactor Concept. Technical Report INL/CON-16-40086, Idaho National Laboratory, February 2017.

[4] J. I. Sackett letter dated March 25, 1992 to E. J. Hughes. Preliminary look at: EBR-II transient test OPT-1, 1992.

[5] H. Tsai, J. P. Herzog, L. L. Briggs, and M. C. Billone. Data package for the irradiation of IFR overpower transient test OPT-1 (X512) in EBR-II. Technical Report IPS-58-00-00, 1991.

[6] S. L. Hayes, D. Porter, and D. Crawford. Metallic fuel validation meeting notes. Personal Communication, June 2019.

[7] Compiled by: IFR Property Evaluation Working Group. Metallic fuels handbook. Argonne National Laboratory, June 1988.

[8] B. M. Adams, L. E. Bauman, W. J. Bohnhoff, K. R. Dalbey, M. S. Ebeida, J. P. Eddy, M. S. Eldred, P. D. Hough, K. T. Hu, J. D. Jakeman, J. A. Stephens, L. P. Swiler, D. M. Vigil, and T. M. Wildey. Dakota, a multilevel parallel object-oriented framework for design optimization, parameter estimation, uncertainty quantification, and sensitivity analysis: Version 6.0 user's manual. Technical Report SAND2014-4633 Version 6.3, Sandia National Laboratories, 2015.

[9] L. L. Briggs, L. K. Chang, and D. J. Hill. Safety Analysis and Technical Basis for Establishing an Interim Burnup Limit for Mark-V and Mark-VA Fueled Subassemblies in EBR-II. Technical Report ANL-NSE-1, Argonne National Laboratory, May 2018.

[10] M. F. Marchbanks, R. A. Moen, and J. E. Irvin. Nuclear systems materials handbook. Technical Report HEDL-SA-871, Hanford Engineering Development Lab., Richland, Wash, 1972.

[11] V. Z. Jankus and R. W. Weeks. LIFE-II A Computer Analysis of Fast-Reactor Fuel-Element Behavior as a Function of Reactor Operating History. *Nuclear Engineering and Design*, 18:83–96, 1972.

[12] J. Rest. Kinetics of fission-gas-bubble-nucleated void swelling of the alpha-uranium phase of irradiated U-Zr and U-Pu-Zr fuel. *Journal of Nuclear Materials*, 207:192–204, 1993.

[13] D. Yun, J. Rest, G. L. Hofman, and A. M. Yacout. An initial assessment of a mechanistic model, GRASS-SST, in U-Pu-Zr metallic alloy fuel fission-gas behavior simulation. *Journal of Nuclear Materials*, 435:153–163, 2013.

[14] T. Ogata M. Kinoshita, H. Saito, and T. Yokoo. Analytical study on deformation and fission gas behavior of metallic fast reactor fuel. *Journal of Nuclear Materials*, 230:129–139, 1996.

[15] T. Ogata and T. Yokoo. Devlopment and Validation of ALFUS: An Irradiation Behavior Analysis Code for Metallic Fast Reactor Fuels. *Journal of Nuclear Technology*, 128(1):113–123, 1999.

[16] W. Hwang, C. Nam, T. S. Byun, and Y. C. Kim. MACSIS: A Metallic Fuel Performance Analysis Code for Simulating In-Reactor Behavior Under Steady-State Conditions. *Nuclear Technology*, 123(2):130–141, 1998.

[17] T. Kobayashi, M. Kinoshita, S. Hattori, T. Ogawa, Y. Tsuboi, M. Ishida, S. Ogawa, and H. Saito. Development of the SESAME Metallic Fuel Performance Code. *Nuclear Technology*, 89(2):183–193, 1990.

[18] C. Pokor, Y. Brechet, P. Dubuisson, J.-P. Massoud, and X. Averty. Irradiation damage in 304 and 316 stainless steels: experimental investigation and modeling. Part II: Irradiation induced hardening. *Journal of Nuclear Materials*, 326:30 – 37, 2004.

[19] Masayuki Kamaya and Masahiro Kawakubo. True stress-strain curves of cold worked stainless steel over a large range of strains. *Journal of Nuclear Materials*, 451:264 – 275, 2014.

[20] Jin Weon Kim and Thak Sang Byun. Analysis of tensile deformation and failure in austenitic stainless steels: Part I – Temperature dependence. *Journal of Nuclear Materials*, 396:1 – 9, 2010.

[21] Jin Weon Kim and Thak Sang Byun. Analysis of tensile deformation and failure in austenitic stainless steels: Part II – Irradiation dose dependence. *Journal of Nuclear Materials*, 396:10 – 19, 2010.

[22] T. R. G. Kutty, C. B. Basak, A. Kumar, and H. S. Kamath. Creep beahviour of δ-phase of U-Zr system by impression creep technique. *Journal of Nuclear Materials*, 408:90–95, 2010.

[23] Pavel Medvedev. Fuel performance modeling results for representative FCRD irradiation experiments: Projected deformation in the annular AFC-3A U-10Zr fuel pins and comparison to alternative designs. Technical Report INL/EXT-12-27183 Revision 1, Idaho National Laboratory, 2012.

[24] D.R.Olander. *Fundamental aspects of nuclear reactor fuel elements*. Technical Information Center, Energy Research and Development Administration, 1976.

[25] Aydin Karahan. *Modeling of thermo-mechanical and irradiation behavior of metallic and oxide fuels for sodium fast reactors*. PhD thesis, Massachusetts Institute of Technology, June 2009.

[26] Ho Jin Ryu, A. M. Yacout, Yeon Soo Kim, and G. L. Hofman. Review of HT9 Cladding Creep Correlations for Advanced Liquid Metal Fast Reactors. In *Transactions of the American Nuclear Society*, volume 94, pages 797–798. ANS, 2006.

[27] R. G. Pahl, D. L. Porter, C. E. Lahm, and G. L. Hofman. Experimental Studies of U-Pu-Zr Fast Reactor Fuel Pins in EBR-II. Technical Report CONF-8809202–2, Argonne National Laboratory, 1988.

[28] H. Tsai, A. B. Cohen, M. C. Billone, and L. A. Neimark. Irradiation Performance of U-Pu-Zr Metal Fuels for Liquid-Metal-Cooled Reactors. Technical Report CONF-950426–6, Argonne National Laboratory, 1994.

[29] H. Yamada. The Effect of Axial Stress on the Transient Mechanical Response of 20% Cold-Worked Type 316 Stainless-Steel Cladding. *Nuclear Technology*, 42(3):324–331, 1979.

[30] N. Scott Cannon and Gary L. Wire. Controlled Biaxial Strain-Rate Testing of 20% Cold-Worked Type 316 Stainless Steel Fast Reactor Claddin. *Nuclear Technology*, 63(1):50–62, 1983.

[31] D. R. Duncan. Effect of Prior Irradiation Creep on the Subsequent Burst Strength of 20% Cold-Worked Type 316 Stainless-Steel Cladding. *Nuclear Technology*, 39(2):199–206, 1978.

[32] Y. H. Sohn, M. A. Dayananda, G. L. Hofman, R. V. Strain, and S. L. Hayes. Analysis of constituent redistribution in the γ (bcc) U-Pu-Zr alloys under gradients of temperature and concentrations. *Journal of Nuclear Materials*, 279:317–329, 2000.

[33] Yiren Chen. Irradiation Effects of HT-9 Martensitic Steel. *Nuclear Engineering and Technology*, 45(3):311–322, 2013.

[34] R. G. Pahl, C. E. Lahm, and S. L. Hayes. Performance of HT9 clad metallic fuel at high temperature. *Journal of Nuclear Materials*, 204:141–147, 1993.

[35] D. Yun, A. M. Yacout, and A. E. Wright. Thermo-mechanical modeling of U-Pu-Zr metallic fuel. In *Transactions of the American Nuclear Society*, volume 106, pages 1205–1206. ANS, 2012.

[36] Gerard L. Hofman, R. G. Pahl, C. E. Lahm, and D. L. Porter. Swelling Behavior of U-Pu-Zr Fuel. *Metallurgical Transactions A*, 21A:517–528, 1990.

Chapter 8

Database Preparation and Correlation Implementation

Y. Miao
A. Oaks
A. M. Yacout

This chapter summarizes the efforts made by Argonne National Laboratory (ANL) for metallic fuel capability development and validation for the Bison code [1]. These efforts include the preparation of experimental data to support current and future Bison metallic fuel model validation and the implementation of a few metallic fuel correlations. The existing experimental data that are valuable for Bison validation were mainly collected during the previous Integral Fast Reactor (IFR) program, including the extensive data collected in the Experimental Breeder Reactor II (EBR-II) and out-of-pile whole-pin transient experiments performed at ANL. These data have been organized and improved to facilitate the Bison validation work. On the other hand, the metallic fuel simulation capabilities in Bison have been expanded by implementing a series of correlations that have been calibrated and/or validated before using the experimental data. The implemented correlations help improve Bison's performance in predicting fuel-cladding chemical interaction (FCCI) as well as fission gas swelling and release behavior in metallic fuels.

8.1 EBR-II Experiment Data for Bison Validation

8.1.1 EBR-II Fuels Irradiation & Physics Database (FIPD)

Sodium-cooled fast neutron reactors (SFRs) fuels knowledge in the US, including both metallic and oxide fuels, are based on the data collected at EBR-II and Fast Flux Test Facility (FFTF) reactors. The binary and ternary metallic fuel data were mainly produced during the IFR program. This knowledge base includes general reactor information, ANL reports, IFR reports, run reports, memos, post irradiation examination (PIE) reports, drawings, experiments qualification reports, publications in journals and conferences, information regarding measured properties (e.g., IFR metallic fuels handbook [2]), and documents of out of pile experiments. Also, measurement documents like micrographs, profilometry data, fission gas release data, and other data are available.

Early efforts to combine all these data into a database, which is known as IMIS (IFR Materials Information System), were not completed. Since the last decade, industry and institutions have been showing increasing interest in developing metallic fuel based fast reactors, which will benefit from a fast reactor database including accurate and detailed operating and performance parameters. Motivated by this increasing demand, U.S. DOE's Advanced Reactor Technology (ART) program has supported efforts to recover and preserve metallic fuel data generated throughout the US SFR program, including the development of the EBR-II FIPD database [3].

FIPD is an organized collection of EBR-II test pin data and documentation. The database includes pin operation conditions calculated using a collection of ANL analysis codes developed during the IFR program, including axial distributions for power, temperatures, fluences, burnup, and isotopic densities. The database also contains pin measured data from post-irradiation examination, including pin fission gas release and gas chemistry measurements, and axial distributions from profilometry, gamma scans, and neutron radiography. There is also an extensive collection of doc-

uments associated with different pins and experiments, including raw PIE data, design descriptions, safety analysis, and operational reports.

The Bison metallic fuel team has got access to FIPD so that the relevant EBR-II data can be collected for current and future Bison validation.

8.1.2 Organization and Improvement of FIPD data

The development of the FIPD database is an ongoing project supported by the ART program. Meanwhile, the quality assurance (QA) of FIPD is also being performed. Therefore, data organization is essential to ensure that appropriate data are utilized in Bison validation. On the other hand, the Bison metallic fuel team is among the first users of the FIPD. Data improvements and customization have also been made according to the feedback from the team in order to facilitate the Bison validation efforts.

The most important improvements are based on the feedback about the accuracy of the power values in FIPD. The power values recorded in FIPD are adopted from the RCT output files of EBR-II runs (RCT is a software that post-processes the depletion-dependent results of neutronics calculations to reconstruct intra-assembly distributions of multigroup fluxes, power densities, burnup, and nuclide number densities). In these RCT output files, the power of each run is computed by dividing deposited energy of the corresponding run with the duration of that run. The EBR-II run duration is calculated by simply subtraction the start and end calendar days. That is, the run duration values used in RCT power computation are rounded into days. However, in reality, some very short EBR-II runs only last for hours (e.g. Run 154B). As a result, the power given in RCT files (and also FIPD and IMIS) may be higher or lower than the real value due to the rounded run duration. Some FIPD users, including the Bison metallic fuel validation team, have applications that are highly sensitive to power level and consequent temperature level (e.g. constituent migration model of metallic fuel). Therefore, correction is required to be made to provide more accurate power levels.

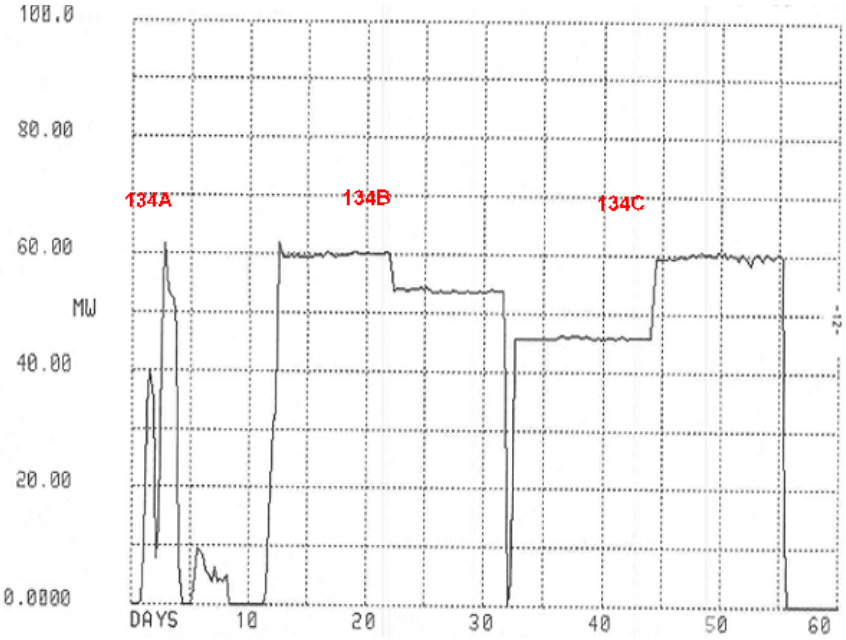

Figure 8.1: DAS power history of EBR-II Run 134 showing the complicated power history (available in FIPD [3]).

EBR-II run duration information with higher time resolution is available from two sources: EBR-II run reports and EBR-II Digital Data Acquisition System (DAS) records [4]. The EBR-II run duration can be rounded to hours using run reports or minutes using DAS records. The run reports have been added into FIPD. The DAS power has also been added into FIPD as a part of the GLASS (Germanium-Lithium Argon Scanning System) data [5]. During the investigation of these run reports and DAS data, some EBR-II runs seem to have more complicated history (see Figure 8.1 as an example). Thus, the maximum power and effective maximum power duration can be given to capture the kinetics sensitive to maximum temperatures, whereas the average power and actual duration can be used to reflect

a more averaged behaviors. For those users who need to capture more detailed power changes, a power history can be provided to satisfy the most complicated needs. The raw DAS power data contains fluctuations due to noise and measurement uncertainty, which may cause stability issues when directly used in Bison simulations. Simplified DAS power values can be generated as piecewise data by referring to run reports. These simplified power data capture the majority of EBR-II power transients without fluctuation. The aforementioned four approaches are shown in Figure 8.2 using EBR-II Run 154A as an example.

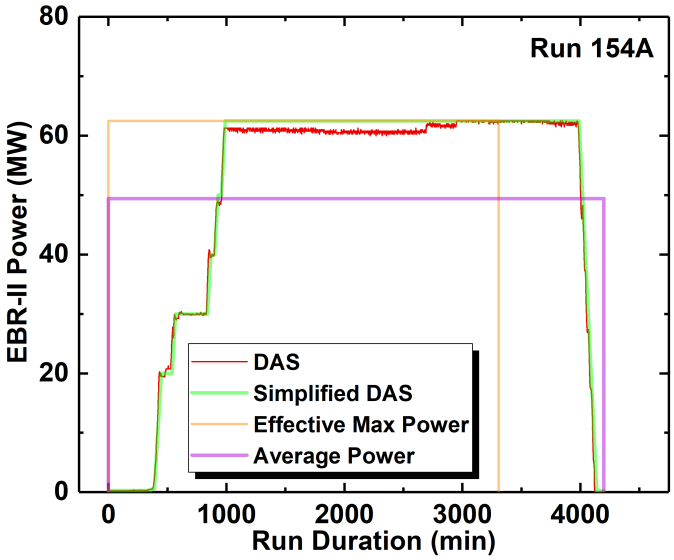

Figure 8.2: Different approaches to use the power history of EBR-II Run 154A.

The relevant data of X419, X441, and X447 pins, which are thought to be valuable for Bison metallic fuel model development and validation, were corrected and improved using all of the aforementioned approaches, and made available to the Bison metallic fuel team in FY2019.

8.2 Whole-Pin Furnace Data for Bison Validation

8.2.1 Summary of Transient Fuel Failure Test Methods

A series of transient fuel failure tests were performed for metallic fuels (binary U-10Zr and ternary U-xPu-10Zr) during the IFR program. Based on the facility information, these tests can be divided into three categories: in-pile transient tests, in-cell transient tests, and ex-cell transient tests. The in-pile transient tests were conducted in the reactors including the Transient Reactor Test Facility (TREAT) and the Experimental Breeder Reactor II (EBR-II). For the in-cell tests, two types of transient testing setups were established, which were dedicated to in-pile-irradiated fuels with different dimension. The Fuel Behavior Test Apparatus (FBTA) was designed to test a segment of in-pile-irradiated fuel with cladding, whereas the Whole Pin Furnace (WPF), as implied by the name, was established to perform transient testing for the whole irradiated fuel pins encapsulated in cladding. On the other hand, the ex-cell tests were mainly focused on the behavior of fresh fuels free of burnup.

The characteristics of each type of transient fuel failure tests are listed in Figure 8.3. In this report, the Whole-Pin Furnace (WPF) tests are focused on. These WPF tests are similar to the FBTA tests, but involved a larger heating zone so that the whole fuel pin instead of a segment of irradiated fuel can be accommodated and tested. As a result, the WPF tests are expected to produce data that are more comparable to the real situation occurring in a fast reactor under transient conditions. Compared to the in-pile transient fuel failure tests performed in EBR-II and TREAT, WPF provides an intermediate solution for both temperature and time regimes, as shown in Figure 8.4.

Categories	In-Pile		In-Cell		Ex-Cell
	TREAT	EBR-II	WPF	FBTA	
Test Articles					
Cladding Types					
Irradiated Fuel					
Whole Pins					
Multiple Pins					
Complex Assemblies					
Sodium Cooling					
Full-Length Pins					

Figure 8.3: Comparison of different transient fuel failure testing methods [6]: the color of the cells indicates the availability of the specific test articles for each testing method (green means available; red means unavailable).

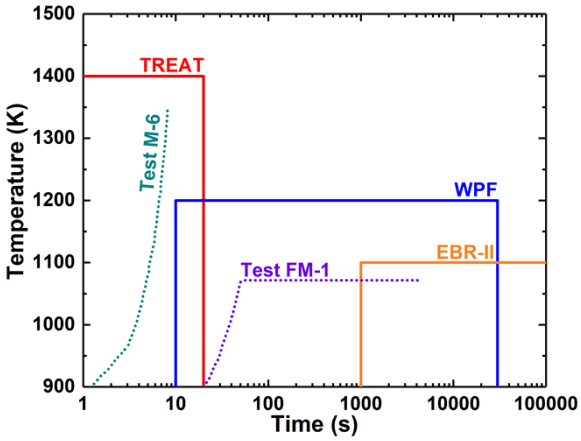

Figure 8.4: Comparison of testing time and temperature regimes of WPF with in-pile transient testing platforms (FM-1 is a typical WPF test while M-6 is a typical TREAT test) [7].

Therefore, in this report, the detailed experimental setup and conditions of WPF will first be introduced. Followed are the available data of these WPF tests. Then the potential Bison validation efforts based on these WPF data are discussed. In the end, the previous LIFE-METAL [8] simulation efforts based on these WPF data will be described as valuable references for future Bison simulations with similar scopes.

8.2.2 Whole-Pin Furnace Experiment Setup

The WPF system was established in the Alpha-Gamma Hot Cell Facility (AGHCF) at Argonne National Laboratory (then ANL-E). The objectives of the WPF tests are threefold: (1) to determine the cladding failure thresholds, mechanisms, and modes of the in-pile irradiated metallic fuel pins under simulated reactor accident conditions with emphasis on long-term (minutes to days) loss-of-flow and/or loss-of-heat sink events; (2) to provide data to enable the further development and validation of fuel-pin failure models for fuel performance codes; and (3) to enable the temperature condition and time duration bridging those in TREAT and EBR-II transient tests (as shown in Figure 8.4).

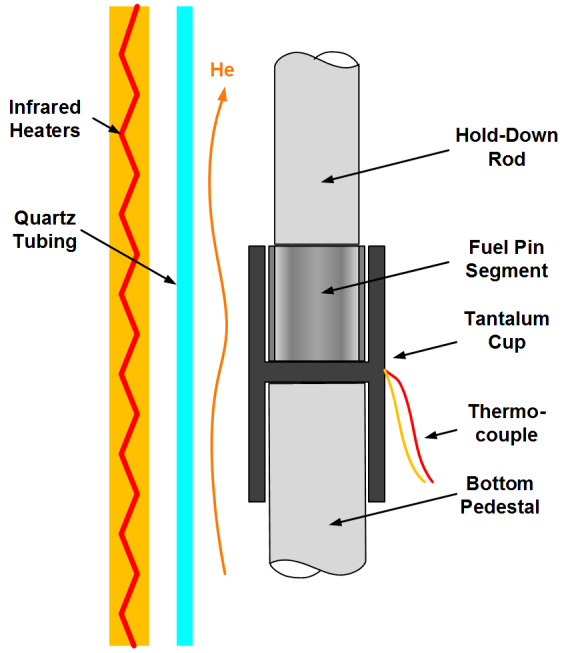

Figure 8.5: Experiment setup of the Fuel Behavior Test Apparatus (FBTA) [9]

Prior to the establishment of the WPF system, a series of out-of-pile transient tests for in-pile-irradiated metallic fuel with cladding had been conducted in the FBTA facility (Figure 8.5). However, due to the limitation in sample dimension of the FBTA facility, only a segment of fuel slug with cladding sectioned from an in-pile-irradiated metallic fuel pin could be tested. With the WPF system, an intact fuel pin with cladding could be tested to provide references obtained under conditions that are more similar to in-pile conditions.

The WPF system was designed to perform two types of tests, (1) run-to-breach tests, and (2) safety demonstration tests. Those run-to-breach tests, which are the focus of this report, involve heating an intact in-pile-irradiated fuel pin at a high temperature (e.g. 800°C) expected in accident scenarios and holding the temperature until the cladding failure. The safety demonstration tests, on the other hand, were designed to prove that certain fuel designs can survive some specific transient events. The design of the WPF system is shown in Figure 8.6. A metallic fuel pin that was irradiated in a fast neutron reactor (e.g. EBR-II) is entirely encapsulated in a stainless steel tube. Six K-type thermocouples are also installed inside the stainless steel tube to monitor the temperatures at different axial positions. Outside the stainless steel tube, an S-type thermocouple is attached on the tube to control the heating of the fuel pin. On the top of the stainless steel tube, two pressure transducers are installed to monitor the breach of cladding by detecting pressure increase caused by the released plenum gas. The entire stainless steel capsule tube is located in a quartz tube with He coolant flowing inside. The quartz tub is heated in a 65 cm long heating chamber powered by four longitude infrared filament lamps. The furnace is capable of operating at 1100°C for extended periods or 1650°C for short periods at a

ramping rate up to 30°C/s. The furnace has a long heating region with near-uniform power and temperature profile as shown in Figure 8.7. Additionally, the released plenum gas is also analyzed by a mass spectroscopy.

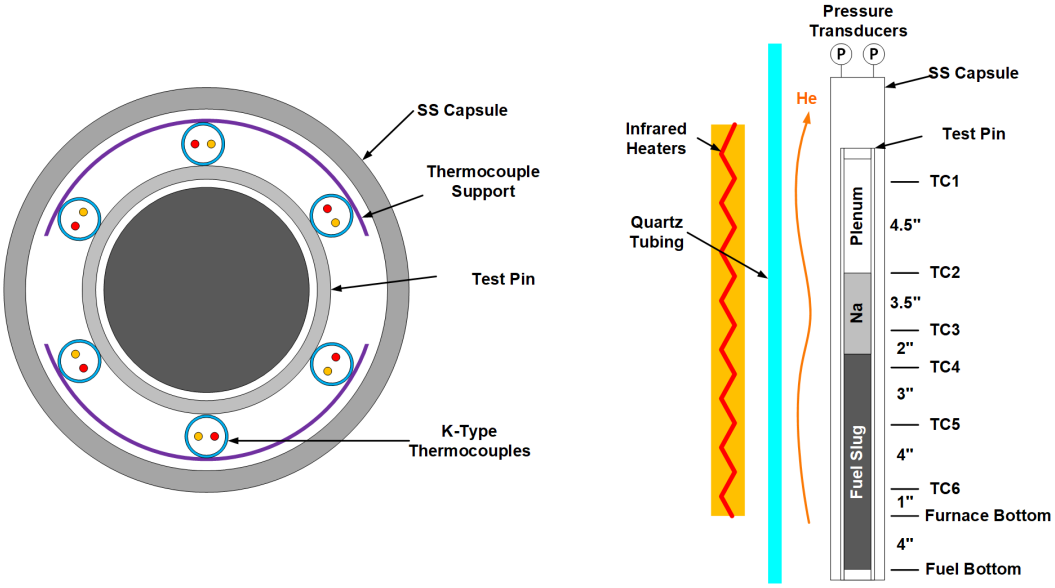

Figure 8.6: Experiment Setup of the WPF system (FM-1) [9]

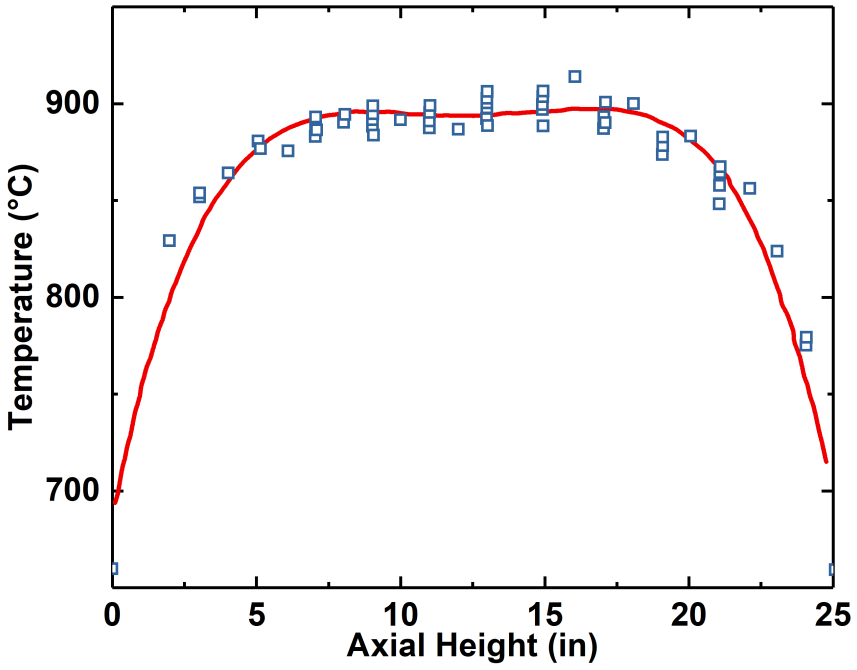

Figure 8.7: A typical temperature profile of the WPF system [10]: the blue squares are measured values, while the red curve is the fitting result.

Using the WPF system, a series of run-to-breach tests were performed for those metallic fuel pin irradiated in EBR-II as a part of the IFR program.

8.2.3 WPF Data Availability

Seven tests were completed in the WPF system for both binary and ternary metallic fuel pins irradiated in EBR-II. The information of these WPF tests can be found in Table 2.

Table 8.1: Completed Whole-Pin Furnace (WPF) tests for U-xPu-10Zr pins [9]

Test	Exp/Pin	x	Cladding	P/F Ratio	Bu (at.%)	Temperature ($°C$)	Types
FM-1	X425/T418	0	HT9	1.0	3.0	820	Run-to-breach
FM-2	X425/T461	19	HT9	1.0	3.0	820	Run-to-breach
FM-3	X430A/T680	26	HT9	1.4	2.2	820	Run-to-breach
FM-4	X441A/DP22	19	HT9	1.5	11.4	770	Run-to-breach
FM-5	X441A/DP15	19	HT9	1.5	11.4	4°C/s to 780	Safety Demo
FM-6	X441A/DP39	19	HT9	1.0	11.3	650-670	Safety Demo
FM-7	X429B/T539	19	SS316	1.0	13.5	650-670	Safety Demo

A variety of metallic fuel pins irradiated in EBR-II, with different Pu contents, cladding materials, plenum to fuel (P/F) ratios, and burnups were tested in the WPF system. Test FM-1 was the first in-cell experiment of the WPF system, which demonstrated the capacity of the system. Tests FM-2 through FM-4 were failure mode tests which were designed to investigate the failure mechanism and kinetics of metallic fuel pins during accident scenario. Test FM-5 was a safety proof test which showed that the EBR-II Mark-V driver fuel can survive the most severe EBR-II design basis accident transient without failing and with minimal cladding damage. Tests FM-6 and FM-7 demonstrated that high-burnup U-19Pu-10Zr metallic fuel can operate for 36 hours at temperature up to 650°C without eutectic formation at the fuel-cladding interface.

The data of WPF experiments will be stored along with FBTA experiments data in the Out-of-Pile Transient Database (OPTD), which is being developed by ANL [9]. The OPTD database is anticipated to be released in FY2020. In this early stage, the OPTD will only include archived documents of those FBTA and WPF experiments, including a collection of records ranging from informal/internal memoranda to formal programmatic progress reports and publications. The related hard copy records were collected, scanned, and saved as text-searchable PDF files in OPTD. The database will be expected to continue to expand in the future when more records are found and when data organization/digitization is performed. The Bison metallic fuel validation team will get access to the OPTD once it is released. Meanwhile, as the current version of OPTD is a document-only database, we have made efforts to organize and digitize some of the WPF experiment data we think will be valuable for Bison validation, including experiments FM-1, FM-4 and FM-6. These data have been made available to the Bison metallic fuel team so that the team can start working on the validation effort before the official release of the OPTD.

8.2.4 Possible Bison Validation Efforts based on WPF Data

The initial conditions of the WPF transient testing are the final conditions of those metallic fuel pin irradiated in EBR-II under steady-state conditions, whereas the test pins experience high temperature only during the simulated accident scenario conditions in the WPF system. Therefore, the WPF test results can potentially be used to validate both steady-state and power transient correlations in advanced fuel performance codes such as Bison. Here, some representative potential applications of the WPF data in Bison validation will be discussed. In addition, as these WPF experiments were originally designed and conducted to provide information for the model calibration and validation of the LIFE-METAL fuel performance code, the corresponding efforts are also provided in this report for references.

The initial conditions of the fuel pins tested in the WPF transient experiments can be found in the FIPD (see Figures 8.8 and 8.9 for an example). For example, Pin T418 from the X425 subassembly, which was tested in the FM-1 WPF test, was irradiated in EBR-II from Run 139A through Run 140B up to a $\sim$2.9 at.% burnup. The data of this pin in the FIPD can be used as important initial conditions for transient simulations. Also, those steady-state correlations and models in the fuel performance codes can also be calibrated or validated. On the other hand, the results of these

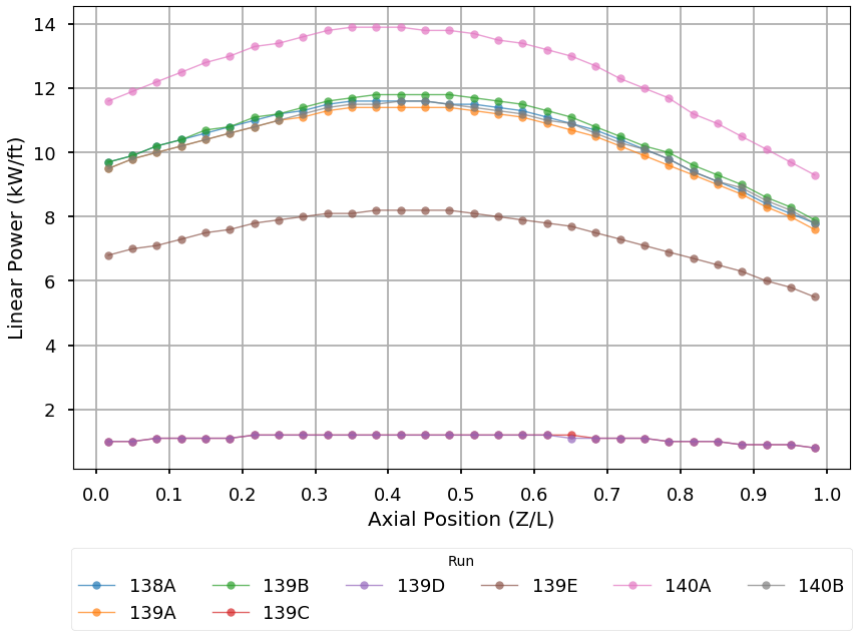

Figure 8.8: Linear power of Pin T418 from X425 subassembly in FIPD [3].

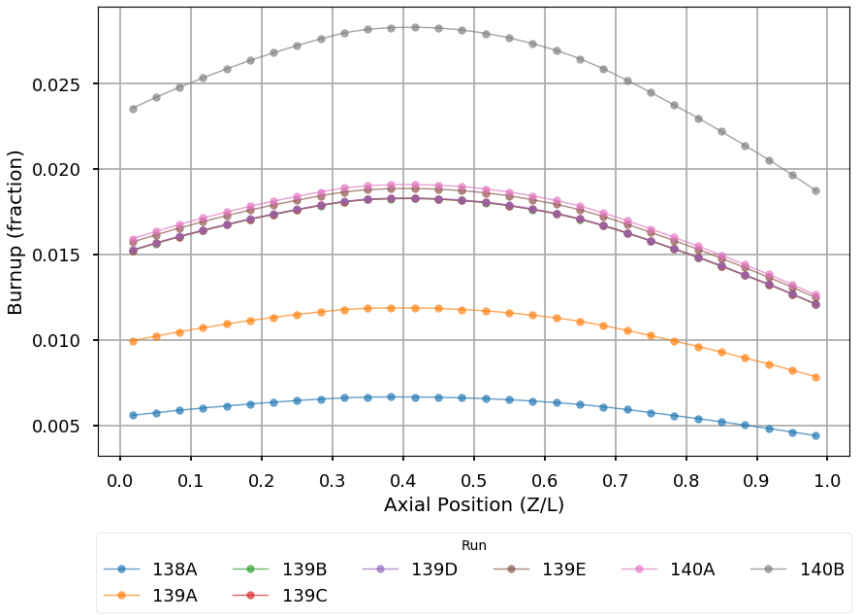

Figure 8.9: Atomic burnup of Pin T418 from X425 subassembly in FIPD [3].

WPF test results can mainly be used to calibrate or validate the power transient correlation and models in these fuel performance codes.

Fission gases (Xe and Kr) accumulate within the fuel during fuel depletion, forming bubbles which interconnect to release gas into the plenum, providing the initial status of the WPF test. During the FM-1 WPF test, the fuel pin was heated beyond the eutectic melting point of the fuel-cladding system. During this procedure, as the fuel temperature is high, the kinetics of thermally-activated fission gas diffusion may be activated and lead to extra gaseous swelling and gas release. Phenomena include fission gas bubble expansion at high temperatures due to creep, fission gas bubble migration and coalescence at high temperatures, etc. On the other hand, in the fuel area that is affected by eutectic melting, the retained fission gas can be directly released into the plenum. Therefore, through direct measurement/analysis of the released plenum gas (volume and composition), a reference is available for the calibration of both steady-state and power transient correlations/models for fission gas behavior.

The major results of the WPF transient experiments, especially the run-to-breach tests (Tests FM-1 through FM-4), are focused on the failure mechanism and kinetics of the fuel cladding at high temperatures due to a combination of fuel cladding mechanical and chemical interaction (FCMI/FCCI). As these run-to-breach experiments were conducted at temperatures higher than the eutectic melting points of fuel-cladding, the FCCI during these WPF transient tests is dominated by the eutectic penetration instead of wastage formation and growth. Therefore, these tests can be valuable references for the calibration and validation of eutectic penetration models/correlations. Also, at the high temperatures available in these transient tests, both fuel slug and plenum gas experience thermal expansion, resulting into enhanced FCMI to the cladding that experiences eutectic thinning simultaneously. Both hoop stress and cumulative damage fraction can be simulated to calibrate and validated related models/correlations.

WPF transient experiments were designed and performed originally to support the development of the LIFE-METAL fuel performance code. LIFE-METAL was extensively used to simulate these experiments and produce a lot of data. These previous validation experiences as well as the previously developed models/correlations can be valuable reference for the development of the Bison fuel performance code. Because FM-1 is a low-burnup pin, no prominent FCMI occurred at the breach point, the failure was solely induced by the plenum gas pressure. The pressure continues to decrease during the test because of the expansion of the cladding at high temperature and under high pressure. However, as the eutectic penetration has a rate of approximately 0.043 μm/s, the continuous thinning of the cladding leads to an increase in hoop stress. The failure criteria used here is cumulative damage fraction (CDF), a short time/transient CDF model was used in the LIFE-METAL simulation. The LIFE-METAL code is capable of accurately predicting the failure time of the test pin in the FM-1 transient test [11]. A summary of the LIFE-METAL simulation of WPF tests can be found in Ref. [12]. Similar simulations can also be performed by Bison once the corresponding models and correlations are developed.

8.3 Implementation of FCCI Correlations

FCCI in metallic fuel is a complex diffusion process the involves multiple components. In the typical metallic fuel with HT9 cladding system, the FCCI mainly includes two phenomena, the formation of a fission product (FP) enriched layer and the depletion of carbon in HT9. Both the FP layer and carbon-depleted layer have degraded mechanical properties compared to the original HT9 cladding and are therefore termed "wastage". Therefore, FCCI effectively reduces the thickness of the cladding and therefore affects the fuel performance such as the fuel-cladding mechanical interaction (FCMI) and cladding creep and failure mechanisms. In EBR-II experiments such as X441 and X447, it was found that the thickness of FCCI wastage can be over 100 μm at $\sim$10% burnup, which is a significant fraction of the original cladding thickness. Therefore, reliable prediction of the FCCI kinetics is an essential part of a metallic fuel performance code. During the IFR program, a series of metallic fuels have been irradiated in EBR-II. Post-irradiation examinations (PIEs) of these fuels produced numerous measurement data of the FCCI wastage thickness under a variety of irradiation conditions. A few FCCI wastage correlations have been developed at ANL based on these PIE data. The description and implementation of these FCCI correlations will be provided in this section.

8.3.1 Correlations Development

As previously mentioned, FCCI is a complex multi-component diffusion process that involves a series of parameters. As a diffusion process, it is affirmatively dependent to irradiation time and temperature. On the other hand, because fission products are important for the formation of the wastage layer, the FCCI is dependent on the burnup of the fuel

as it measures the amount of fission product atoms available for wastage formation. Three different empirical FCCI correlations have been developed at ANL based on the wastage thickness measurement of the metallographs of sectioned fuel irradiated in EBR-II (available in FIPD as PIE data). All of them, described here, have been implemented into the Bison code.

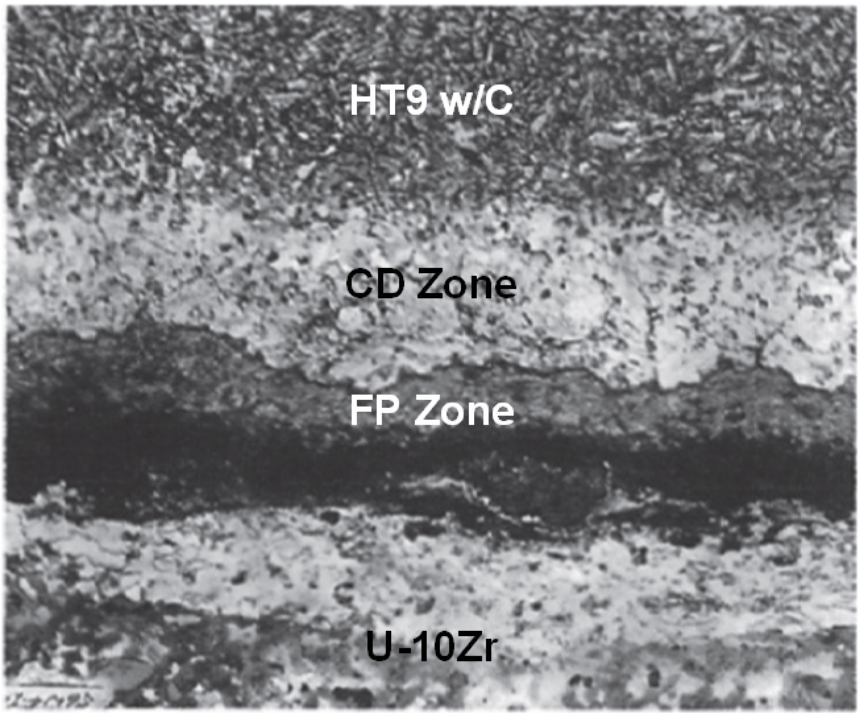

Figure 8.10: A metallograph of the cladding wall, showing the carbon-depletion (CD) zone and the fission product (FP) zone [13].

Before introducing the details of each correlation, the wastage thickness must be defined. The metallograph of a typical irradiated pin is shown in Figure 8.10. This fuel has a U-10Zr fuel slug and HT9 cladding with an initial smeared density (SD) of 75%. In this metallograph, the carbon-depletion (CD) zone shows a lighter contrast compared to the normal HT9 cladding, while the fission product (FP) zone has a darker contrast then the CD zone. The thickness of the CD and FP zones can be defined as δ_{cd} and δ_{fp}, respectively. In addition, when FPs diffuse into cladding to form the wastage layer, cladding elements (mainly Fe) also diffuses into the fuel. The Fe diffusion leads to the local thinning of the cladding and formation of U-Fe composition in the fuel slug. Although not explicitly shown in the metallographs, the thinning of the cladding, δ_h, can also be quantified from the metallographs by counting the missing thickness of the cladding. Here, δ_h definitely needs to be subtracted from the cladding thickness for effective stress calculation. Meanwhile, as the FP layer is fragile and cannot take any loading, δ_{fp} also needs to be fully subtracted. The CD zone, however, is literally a low-carbon steel with reduced mechanical strength compared to HT9. Therefore, the factor, f_{cd}, is used to measure the effective reduction in mechanical strength of CD HT9. On the other hand, for each metallograph, multiple measurements can be made at different circumferential locations. The maximum measured values need to be used as this represents the maximum stress situation. Therefore, the measured FCCI wastage thickness, δ_w, has the following expression,

$$\delta_w = max\left(\delta_h + \delta_{fp} + f_{cd} \cdot \delta_{cd}\right) \tag{8.1}$$

In this project, f_{cd} was selected because it was previously found to give the overall best fit to measured cladding hoop strain and failure statistics. As δ_h values are usually marginal compared to the other two components, it was sometimes neglected during the correlation fitting. On the other hand, the fitting of FCCI correlations requires accurate temperature, flux and burnup data. Both FIPD [3] and Carmack's simulations [14] were used to fit the data.

The first correlation [15] is dependent on temperature (T), irradiation time (t), and fast neutron flux (ϕ). The burnup is implicitly taken into account by involving the neutron flux. In this correlation, the growth rate of wastage

(m/s) is computed as,

$$\frac{\Delta w}{\Delta t} = \frac{1}{2}(D_0 exp(-Q/RT) + D_{i0}\phi)^{\frac{1}{2}} t^{-\frac{1}{2}} \tag{8.2}$$

where ϕ is the neutron fast flux $(n/m^2 \cdot s)$, R is gas constant $(J/mol \cdot K)$, T is temperature (K), t is time (s), and D_0 (m^2/s), Q (J/mol), and D_{i0} (m^4) are empirical parameters. This correlation is the default FCCI correlation used in the current version of LIFE-METAL. For HT9 cladding, the parameters were fitted based on U-19Pu-10Zr Pins DP16 and DP21 and U-10Zr Pins DP70 and DP75. Note that δ_h was neglected during the fitting of this correlation.

The second correlation [16] is dependent on temperature (T), irradiation time (t), and atomic burnup (Bu). The growth rate of wastage (m/s) has the following expression,

$$\frac{\Delta w}{\Delta t} = 2Bu(k_0 exp(-Q_b/RT)) t^{-\frac{1}{2}} \tag{8.3}$$

where Bu is the atom percent burnup, R is gas constant $(J/mol \cdot K)$, T is temperature (K), t is time (s), and k_0 $(m/s^{\frac{1}{2}})$ and Q_b (J/mol) are empirical parameters. This correlation was most recently developed and thus includes the measurement of δ_h. The parameters were mainly fitted for U-10Zr fuel and HT9 cladding, based on Pins DP04, DP11, DP69, DP70, DP75, and DP81 irradiated in X447/A experiment.

The last correlation [17] is dependent on temperature (T), irradiation time (t), atomic burnup (Bu), and fast neutron flux (ϕ). In this correlation, burnup is included to represent the available FPs while fast flux is used to quantify radiation-enhanced diffusion. The growth rate of wastage (m/s) is governed by the following equation,

$$\frac{\Delta w}{\Delta t} = 2Bu(D_0 exp(-Q/RT) + D_{i0}\phi)^{\frac{1}{2}} t^{-\frac{1}{2}} \tag{8.4}$$

This correlation was also fitted without taking δ_h in to consideration. For the U-10Zr and HT9 fuel system, the parameters were based on Pins DP04, DP11, DP70, and DP75 irradiated in X447/A experiment.

8.3.2 Implementation and Benchmark

All these three FCCI correlations have been implemented into Bison as the "MetallicFuelWastage" module. The units have all been converted to SI as required by Bison implementation. The current sets of parameters available in the Bison code for these three correlations are usually for HT9 cladding with binary or ternary metallic fuels. Parameter sets fitted for other cladding materials such as SS316 and D9 are also available and can be added into the Bison code if needed in the future.

Benchmarking for the implemented correlations was performed by using Bison to simulate six pins (DP04, DP11, DP69, DP70, DP75, and DP81) irradiated in X447/A experiments. The recently improved FIPD data were used as the input parameters, such as power and flux history, for these simulations (see Figure 8.11 for average linear power history informed by the DAS data). It is worth mentioning that these FCCI correlations were all calibrated using the effective full power time so that Equations 8.2 through 8.4 can be integrated to a simple form for fitting. Therefore, the Bison predicted results are expected to slightly differ from the results produced during fitting.

The time evolution of peak cladding temperature of the six pins predicted by Bison is illustrated in Figure 8.12. The prediction is consistent with the designed $\sim$650°C peak cladding temperature as well as the related FIPD data. The Bison simulation of Pin DP75 is discussed here as an example. After the EBR-II irradiation, Pin DP75 was sectioned at nine axial positions (x_f/L_f = 0.19, 0.44, 0.68, 0.81, 0.90, 0.92, 0.93, 0.98, 1.00). The peak cladding temperatures (i.e. inner surface temperature) of all these nine investigated axial positions predicted by Bison are shown in Figure 8.13. Based on the power history from the improved FIPD data, the time evolution of atomic burnup of all these axial positions can be found in Figure 8.14, which is consistent with the designed $\sim$10% atomic burnup. The Bison predicted FCCI wastage thickness at the end of the X447/A irradiation is also directly compared with the metallography measurement data in Figure 8.15.

The predicted FCCI wastage thickness was found consistent with the measurement of the metallographs (measurement values from Ref. [16]), especially when the FCCI wastage is thick (i.e. high burnup, high flux, and high temperature). A comprehensive comparison between the Bison computed values and experimentally measured values is shown in Figure 8.16. For those lower measured wastage thickness values, which were mainly collected in the pins only irradiated in X447 experiment or at low axial positions, the implemented correlations sometimes overestimate the wastage thickness values. This overestimation may originate from one simplification method used to develop these

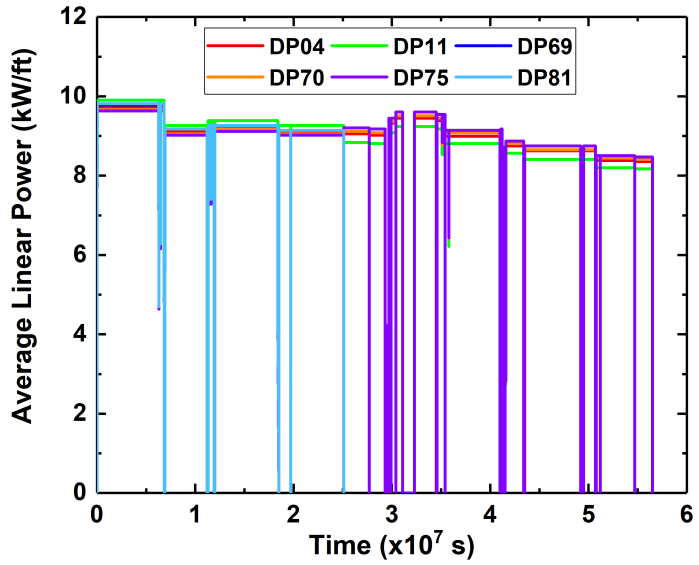

Figure 8.11: Power history of the six pins irradiated in X447/A experiment from improved FIPD data.

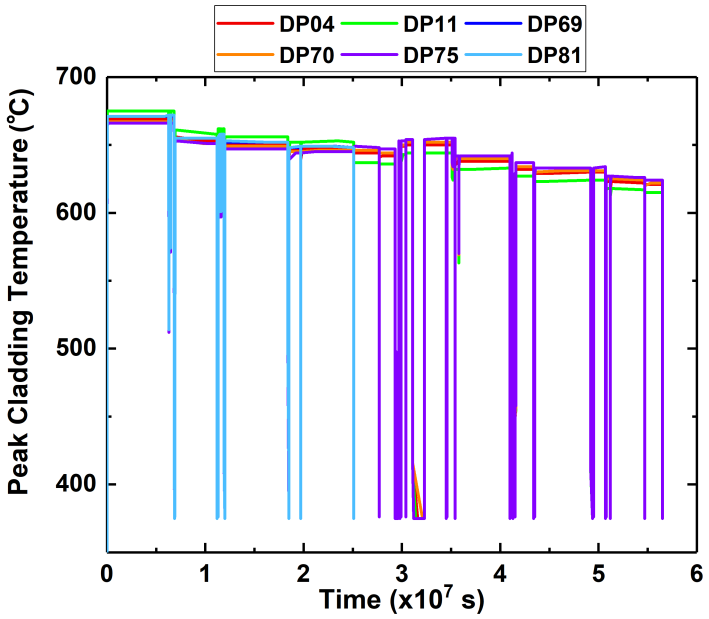

Figure 8.12: Time evolution of peak cladding temperature for the six X447/A pins predicted by Bison

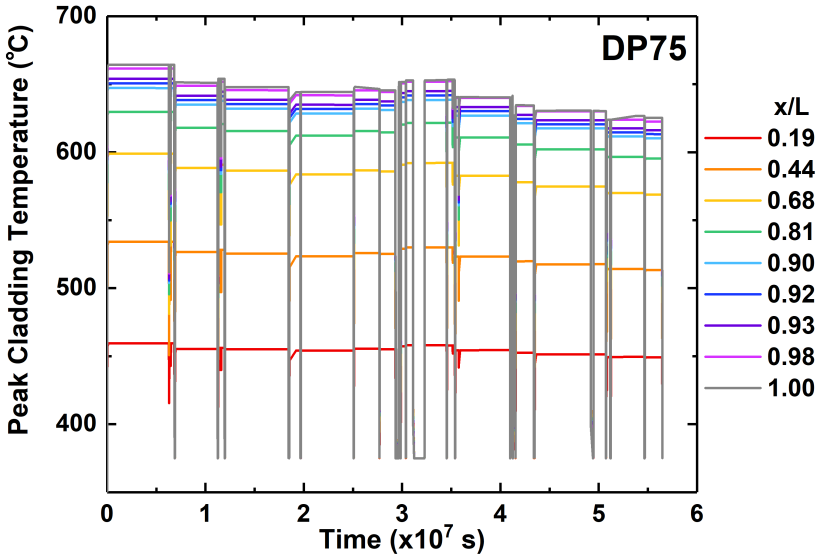

Figure 8.13: Time evolution of peak cladding temperatures at sectioned axial positions of Pin DP75 irradiated in X447/A

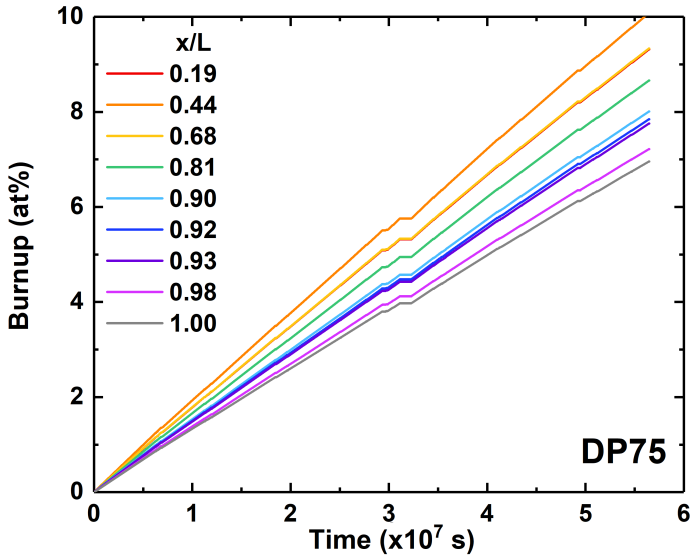

Figure 8.14: Time evolution of atomic burnup at sectioned axial positions of Pin DP75 irradiated in X447/A

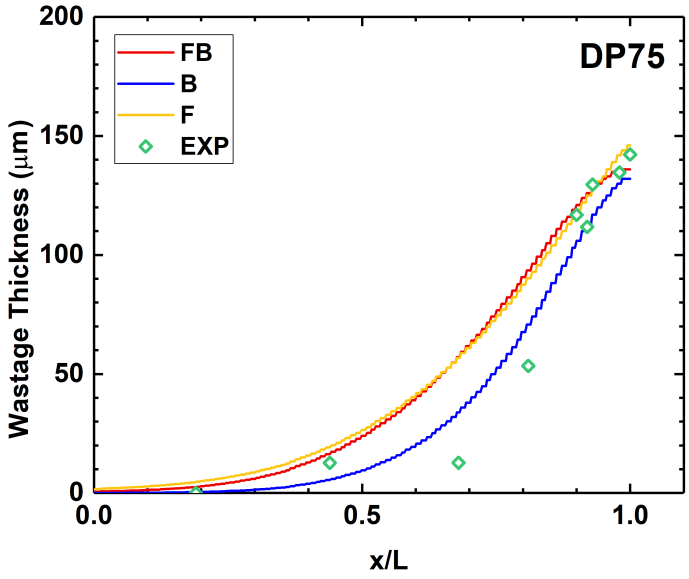

Figure 8.15: Comparison between Bison predicted FCCI wastage thickness and experimental measurements of Pin DP75 irradiated in X447/A

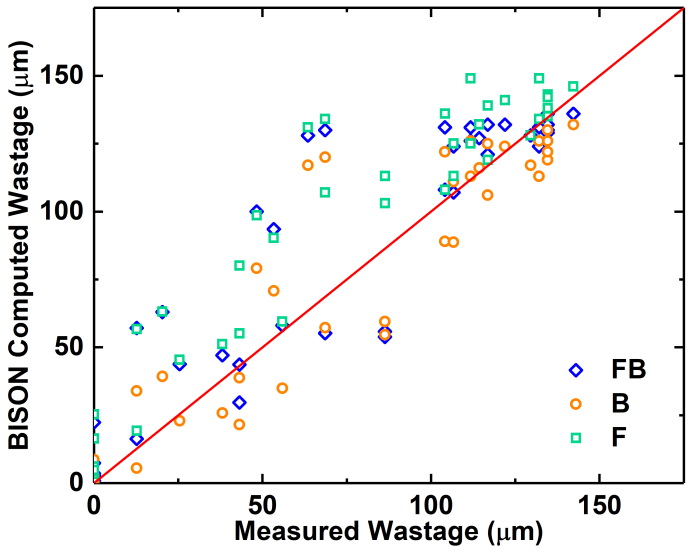

Figure 8.16: Comparison between Bison computed wastage thickness with experiment values[16].

correlations. In a realistic situation, FCCI is expected to start after the fuel-cladding gap is closed. This gap closure usually occurs between 1% to 2% atomic burnup. As the accurate gap closure time is dependent on fission rate and temperature, it is challenging to accurately capture this value. When these correlations are fitted, it is assumed that the FCCI formation starts in the beginning of the irradiation regardless to the gap closure phenomenon. By using this approach, the predicted FCCI thickness may be overestimated at low burnup and are more accurate at high burnup. This approach makes sense as FCCI is only an issue when the thickness is high enough; and the overestimation at low burnup ensures the fuel performance evaluation is conservative.

In the future, Bison simulation can be used to help determined the gap closure time so that new FCCI correlations that are only activated after gap closure can be developed to provide improved fuel performance evaluation data. On the other hand, the FCCI correlations implemented into Bison enable the prediction of wastage thickness. Future development of Bison metallic fuel capabilities are needed to correlate this wastage thickness with the degradation of the cladding performance.

8.4 Swelling and Gas Release Correlations Improvement and Evaluation

Compared to oxide fuels such as UO_2 and MOX, the gaseous swelling is more prominent in metallic fuels. In-pile irradiation experiments of both binary and ternary metallic fuels showed rapid gaseous swelling at quite low atomic burnup ($<\sim$2 at.%). Once the gaseous swelling reaches a $\sim$36% volumetric strain, the fission gas bubbles become readily interconnected and then form open pores as pathways for fission gas release. In that case, the volumetric gaseous swelling becomes "saturated". Beyond that point, the additional dimensional increase of the fuel is contributed by accumulation of solid fission products, which is predicted to produce $\sim$1.5% or $\sim$1.2% volumetric strain per 1% atomic burnup depending whether the dissolution of FPs in liquid sodium is taken into consideration [18, 19]. The swollen metallic fuel slugs induce mechanical stress to the cladding material and thus cause its creep deformation (i.e. FCMI). This phenomenon is critical for metallic fuel performance prediction as the creep process may lead to cladding failure, which is usually quantified using cumulative damage faction (CDF). In the meantime, the release fission gas from these interconnected pores is accommodated in the reserved room within the cladding, which is usually referred to as the plenum. The accumulation of fission gas in the plenum builds up pressures inside the cladding and therefore causes cladding formation. These accumulated fission gas also plays an important role in the fuel failure mechanisms during transient as gas pressure increases linearly with temperature. Therefore, accurate prediction of the swelling and gas release is one of the most important features of a metallic fuel performance code.

8.4.1 Limitations of Existing Correlations

The first metallic fuel swelling and fission gas release correlation in Bison was developed by Medvedev [20] in early 2010s. In this model, a simplified ideal gas approach with a correction based on surface tension and fuel creep is used for gaseous swelling. On the other hand, a 33% volumetric swelling strain is set as the threshold for fission gas bubble interconnection and fission gas release. An 80% gas release fraction is used once this threshold is reached. The correlation captures some most important features of metallic fuels' swelling and gas release behavior and thus was successfully used in a series of pioneering efforts of simulating metallic fuel performance using Bison [20, 21].

However, the simplifications adopted during the correlation development do induce some inaccuracy. The most prominent issue of this correlation is the underestimation of the swelling rate before fission gas bubble interconnection. Using this correlation, Bison usually predicts that the gas bubble interconnection (i.e. 33% swelling strain) is reached at beyond 5% atomic burnup, which differs from the 1$\sim$2% atomic burnup observed in in-pile irradiation experiments [19]. This issue can be temporarily mitigated by employing a scale factor to artificially accelerate the swelling rate. This method was successfully used in FY2018 [22]. The swelling and gas release correlation with the correction factor was successfully used to assess the fuel performance of the Advanced Breeding Reactor (ABR-1000) with annular fuel design [22]. However, a permanent solution needs to be made by equipping Bison with swelling and fission gas release correlations with improved performance.

Meanwhile, LIFE-METAL is equipped with a complex swelling and fission gas release correlation that has been validated using the neutron radiography (NRAD) data [15]. More importantly, in the original gaseous swelling correlation of Bison, because the gaseous swelling strain is directly dependent on local hydrostatic stress (i.e. pressure), the adoption of this correlation may potentially leads to instability of the computation. In the LIFE-METAL correlation, a creep mechanism is utilized to prevent any prompt changes in swelling strain, which not only facilitates the stability

of computation but also makes the correlation more realistic. Therefore, efforts were made to implement the swelling and gas release correlation of the LIFE-METAL code into Bison in parallel to the development of a new metallic fuel swelling correlation.

8.4.2 Implementation of LIFE-METAL Correlation

The implementation of the LIFE-METAL correlation [13] includes the introduction of two new modules into the Bison code, "FgrUPuZrLM" and "UPuZrVolumetricSwellingEigenstrainLM". The former module computes the fission gas release rate, whereas the latter module computes the volumetric swelling strain due to both solid and gaseous FPs. The "FgrUPuZrLM" can be used with other swelling models, but the "UPuZrVolumetricSwellingEigenstrainLM" must be used with the "FgrUPuZrLM" module.

'FgrUPuZrLM' is a fission gas release model for binary and ternary metallic fuel based on the current porosity of the fuel, the current retained fission gas concentration in the fuel, and the fuel temperature. This fission gas release model was originally established and parameterized for the LIFE-METAL fuel performance code by ANL. In this fission gas release model, the fission gas release rate ($\frac{\Delta G_r}{\Delta t}$, $mol/m^3 \cdot s$) is calculated at every time step as the product of the fission gas amount retained in the fuel (G_s, mol/m^3) and a fission gas release factor (F_g, s^{-1}):

$$\frac{\Delta G_r}{\Delta t} = F_g \cdot G_s \tag{8.5}$$

The gas release factor is calculated using the following equation:

$$F_g = (1 - exp(Bu))Aexp(-\frac{Q_g}{R}\frac{1}{T})(1 + c_g\frac{P - 0.1}{P^{\frac{2}{3}}}) + F_{g,i} \tag{8.6}$$

$$F_{g,i} = \begin{cases} f(\varepsilon_s - \varepsilon_c) & \varepsilon_s > \varepsilon_c \\ 0 & otherwise \end{cases} \tag{8.7}$$

where, Bu is the atomic percent burnup, A (s^{-1}) is a pre-exponential coefficient, Q_g (J/mol) is the activation energy for gas released from non-interconnected bubbles, R ($J/mol \cdot K$) is the gas constant, T (K) is the temperature, c_g is a dimensionless constant, P is the porosity of the fuel, ε_s is the gas swelling strain, ε_c is the threshold gas swelling strain for bubble interconnection, and f (s^{-1}) is a constant determining the enhanced gas release rate after bubble interconnection.

On the other hand, "UPuZrVolumetricSwellingEigenstrainLM", computes a volumetric strain to account for solid and gaseous swelling in metallic fuel system. The gas swelling can be further categorized into the swelling strain contributed by van der Waals volume of the the gas atoms and the swelling strain contributed by ideal gas. Also, porosity (summation of as-fabricated porosity and gas swelling porosity) is available as a material property. This swelling model was originally developed for the LIFE-METAL fuel performance code by ANL. The original model was slightly modified with more optional features during the implementation into the Bison code.

Additionally, a simplified anisotropic model based on an anisotropic factor f is added to this swelling model to provide users a tool to adjust axial-to-radial swelling ratio to fit experiment observations. The volumetric swelling strain needs to be convert to logarithmic strain in three directions. If the swelling is isotropic:

$$\varepsilon_{xx} = \varepsilon_{yy} = \varepsilon_{yy} = \frac{1}{3}ln(1 + \varepsilon_{total}) \tag{8.8}$$

When the anisotropic factor f is involved:

$$\varepsilon_{xx} = \varepsilon_{zz} = \frac{f}{3}ln(1 + \varepsilon_{total}) \tag{8.9}$$

$$\varepsilon_{yy} = \frac{3 - 2f}{3}ln(1 + \varepsilon_{total}) \tag{8.10}$$

8.4.3 Assessment of Bison's Fission Gas Behavior Predictions

The assessment of the Bison's fission gas behavior predictions was performed by comparing all available models implemented in the Bison code. Three different sets of fission gas behavior correlations are available in Bison for metallic fuels: (1) the original fission gas behavior correlations developed by Medvedev [20]; (2) the fission gas swelling correlations developed by Matthews and Aagesen in FY2019 ("UPuZrGaseousEigenstrain" module in Bison); and (3) the LIFE-METAL correlation. In FY2018, ANL developed a corrected scale factor for Medvedev's correlation so that the low-burnup swelling rate can be comparable to experimental observations, which can be regarded as a variant of Medvedev's correlation [22]. In addition, as bubble density is a tunable preset parameter in the Matthews-Aagesen (M&A) correlation, two variants can be made by adopting preset bubble density values that are 0.1 and 10 times of the default value for sensitivity studies. Hence, there are three correlations and three variants available for assessment.

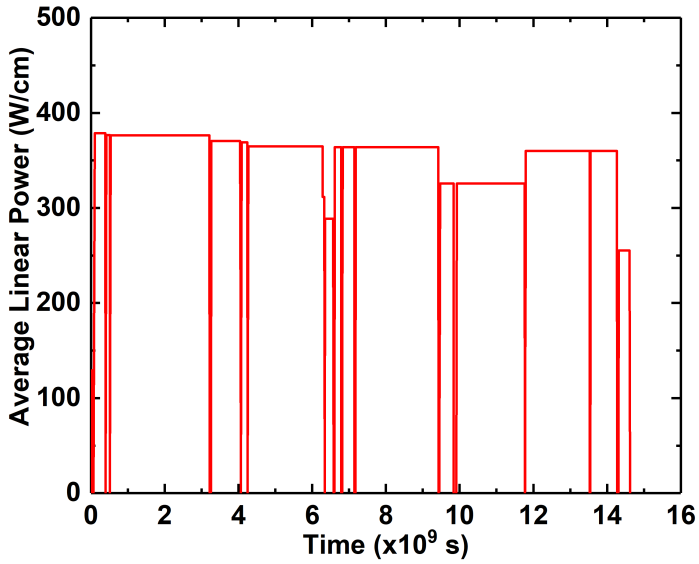

Figure 8.17: Time evolution of average linear power of Pin T333 of X423/A/B.

Pin T333 irradiated in X423/A/B experiment was selected for the assessment because NRAD images were taken for this pin after X423, X423A and X423B irradiations, respectively so that the swelling strains at three different burnup values were obtained. NRAD shows that the saturation of gaseous swelling occurs between 1% and 2% burnup. The operation conditions of this pin were adopted from the improved FIPD data. In Figure 8.17, the average linear power history of Pin T333 during X423, X423A and X423B is illustrated. The time evolution of coolant flow flux is also provided in Figure 8.18. All the six correlations including the three variants were adopted for Bison simulation of Pin T333.

The time evolution of volumetric swelling strain of different correlations is shown in Figure 8.19. As previously discussed, the original metallic fuel swelling correlation developed by Medvedev underestimates the swelling rate before bubble interconnection by approximately 50% under the T333 irradiation condition. Meanwhile, using the default parameters, the Matthews-Aagesen correlation (labeled as M&A) also predicts a swelling rate that is much lower than the measured value before the saturation of the gas swelling. Sensitivity assessment of the M&A correlation by tuning the preset bubble density shows that the adjustment has a significant effect on the predicted swelling strain values. Therefore, the M&A correlation is expected to predict a more realistic swelling rate by fitting the preset density according to the experiment observations. This preset density may also include some dependence to temperature. Meanwhile, it is also prominent that the swelling strain predicted by the M&A correlation is directly dependent on the temperature. As shown by these vertical lines in Figure 8.19, as predicted by the M&A correlation, the fuel rapidly contracts during the temperature drop between reactor runs and rapidly expands as the power/temperature is recovered.

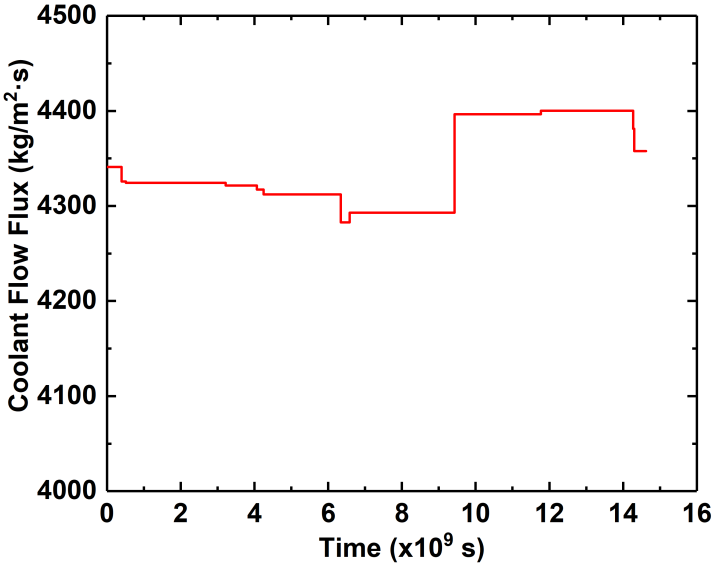

Figure 8.18: Time evolution of coolant flow flux of Pin T333 of X423/A/B.

This phenomenon is not physical as the shrinkage and expansion of fission gas bubbles is controlled by the creep of the fuel material. The steep dips in volumetric swelling strain may also cause potentially stability issues during computation, especially after the occurrence of FCMI. In Medvedev's correlation, although the gaseous swelling is also linear to temperature, the steep dips in volumetric swelling strain are nonexistent because the temperature effect only affects the incremental swelling strain. However, this also implies that Medvedev's correlation lacks a mechanism to account for fission gas bubble expansion during transient events.

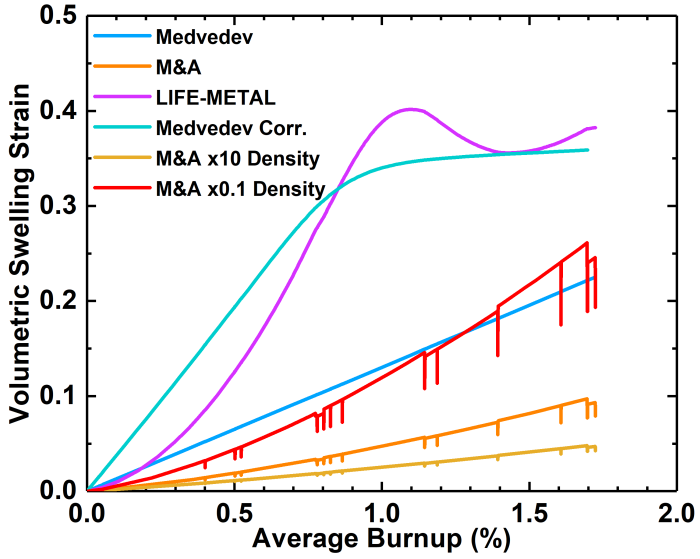

Figure 8.19: Volumetric swelling strains of T333 predicted by various correlations

The corrected Medvedev correlation predicts a swelling rate that is very close to the NRAD observation. However, the swelling before bubble interconnection is almost linear to the burnup, which slightly deviates from the experimental observations. The LIFE-METAL correlation, however, captures the experimentally measured swelling kinetics. As a creep mechanism is involved, the swelling strain is not subject to prompt changes. It is noticeable in Figure 8.19 that the swelling strain predicted by LIFE-METAL correlation fluctuates after reaching the preset 36% saturation gas swelling value. This fluctuation is due to the gas release mechanism governed by Equations 8.6 and 8.7. This fluctuation is probably consistent with the column shrinkage observed in in-pile irradiated metallic fuels [23]. Additionally, the amplitude of this fluctuation is adjustable by tuning f factor.

8.5 Summary

In FY2019, Argonne prepared and improved the experiment data for Bison validation. This effort includes the EBR-II experimental data for several IFR irradiation experiments and out-of-pile transient experimental data of several WPF experiments. These data were selected based on the discussion within the Bison metallic fuel team. Meanwhile, a series of validated metallic fuel correlations, such as FCCI wastage, irradiation swelling, and fission gas release correlations, have been implemented into the Bison code. Benchmarks of these implemented correlations were also performed using the PIE data collected during the IFR program. In addition, the performance of a series of swelling and fission gas release models of metallic fuel available in the Bison code, were evaluated and compared using the irradiation condition parameters and PIE data available in FIPD.

Based on the achievements made in FY2019, a sequence of future efforts have been identified for FY2020. First, more correlations can be implemented into the Bison code to make its metallic fuel simulation capabilities more comprehensive. The proposed correlations include the hot pressing model, eutectic penetration model, and wastage formation model for cladding outer surface, etc. Efforts can also be made to develop and implement a phase-specific gas swelling and release model based on mesoscale mechanistic models. Second, with the completed metallic fuel simulation capabilities, Bison can be used to simulate the transient experiments such as WPF. The simulations include both steady-state fuel operation in EBR-II and the transient heating in furnace and help validate various metallic models in Bison. Third, further preparation and improvements in FIPD and OPTD will be made to timely meeting the validation needs of the Bison code. Last but not least, a comprehensive comparison will be made between Bison and other metallic fuel performance code such as LIFE-METAL. This will help understand the advantages and limitations of the current Bison metallic fuel simulation capabilities and guide future development and validation efforts.

Bibliography

[1] RL Williamson, JD Hales, SR Novascone, MR Tonks, DR Gaston, CJ Permann, D Andrs, and RC Martineau. Multidimensional multiphysics simulation of nuclear fuel behavior. *Journal of Nuclear Materials*, 423(1-3):149–163, 2012.

[2] GL Hofman, L Leibowitz, JM Kramer, MC Billone, and JF Koenig. Metallic fuels handbook. Technical report, ANL-IFR-29, Argonne National Laboratory, 1985.

[3] AM Yacout, A Oaks, W Mohamed, and K Mo. FIPD: EBR-II fuels irradiation & physics database. Technical report, ANL-ART-124, Argonne National Laboratory, 2017.

[4] JM Allen, RW Hyndman, RA Call, EW Laird, MR Tuck, and KD Tucker. Functional description of the EBR-II digital data acquisition system. Technical report, ANL/EBR-029, Argonne National Laboratory, 1970.

[5] JDB Lambert, KC Gross, R Mikaili, SM Frank, DC Cutforth, and PL Angelo. Failed fuel identification techniques for liquid-metal cooled reactors. Technical report, CONF-950311-7, Argonne National Laboratory, 1995.

[6] TH Bauer, JM Kramer, RW Tilbrook, and AJ Goldman. A program to resolve the safety implications of fuel damage in the operation of advanced metal-fueled reactors. Technical report, ANL-IFR-103, Argonne National Laboratory, 1989.

[7] JM Kramer and TH Bauer. Fuel damage during off-normal transients in metal-fueled fast reactors. Technical report, CONF-900804-20, Argonne National Laboratory, 1990.

[8] AM Yacout and MC Billone. Current status of the LIFE fast reactors fuel performance codes. In *International Conference on Fast Reactors and Related Fuel Cycles: Safe Technologies and Sustainable Scenarios*, Palais des Congrès, Paris, France, March 4-7, 2013.

[9] C Tomchik and A Oaks. OPTD: Out-of-pile transient database. Technical report, ANL-ART-124, Argonne National Laboratory, 2018.

[10] YY Liu, HC Tsai, DA Donahue, DO Pushis, FE Savoie, JW Holland, AE Wright, C August, JL Bailey, and DR Patterson. Whole-pin furnace system: An experimental facility for studying irradiated fuel pin behavior under potential reactor accident conditions. Technical report, CONF-900804-24, Argonne National Laboratory, 1990.

[11] MC Billone. Personal communication. 1990.

[12] JM Kramer, YY Liu, MC Billone, and HC Tsai. Modeling the behavior of metallic fast reactor fuels during extended transients. *Journal of Nuclear Materials*, 204:203–211, 1993.

[13] T Ogata, YS Kim, and AM Yacout. *Comprehensive Nuclear Materials, Volume 3*, chapter 3.23 Metal Fuel Performance Modeling and Simulation, pages 713–753. Amsterdam: Elsevier., 2012.

[14] WJ Carmack. *Temperature and burnup correlated fuel-cladding chemical interaction in U-10Zr metallic fuel*. PhD thesis, University of Idaho, 2012.

[15] LL Briggs, LK Chang, and DJ Hill. Safety analysis and technical basis for establishing an interim burnup limit for Mark-V and Mark VA fueled subassemblies in EBR-II. Technical report, ANL-NSE-1, Argonne National Laboratory, 1995.

[16] MC Billone. Personel communication. 2017.

[17] MC Billone. Personal communication. 1994.

[18] T Ogata and T Yokoo. Development and validation of ALFUS: an irradiation behavior analysis code for metallic fast reactor fuels. *Nuclear Technology*, 128(1):113–123, 1999.

[19] GL Hofman, LC Walters, and TH Bauer. Metallic fast reactor fuels. *Progress in Nuclear Energy*, 31(1-2):83–110, 1997.

[20] PG Medvedev. Fuel performance modeling results for representative FCRD irradiation experiments: Projected deformation in the annular AFC-3A U-10Zr fuel pins and comparison to alternative designs. Technical report, INL/EXT-12-27183, Idaho National Laboratory, 2012.

[21] PG Medvedev. BISON investigation of the effect of the fuel-cladding contact irregularities on the peak cladding temperature and FCCI observed in AFC-3A Rodlet 4. Technical report, INL/EXT-16-40027, Idaho Argonne National Laboratory, 2016.

[22] Y Miao, N Stauff, A Oaks, AM Yacout, and TK Kim. Fuel performance evaluation of annular metallic fuels for an advanced fast reactor concept. *Nuclear Engineering and Design*, 352:110157, 2019.

[23] RG Pahl, CE Lahm, R Villarreal, GL Hofman, and WN Beck. Recent irradiation tests of uranium-plutonium-zirconium metal fuel elements. Technical report, CONF-860931-9, Argonne National Laboratory, 1986.

Chapter 9

Implementation of failure modes and statistical treatment to compute failure probability for TRISO particles in Bison

W. Jiang, B.W. Spencer and A. Slaughter

9.1 Introduction

TRistructural ISOtropic (TRISO) coated fuel particle has been accepted by most countries as the reference concept for use in High Temperature Gas Reactors(HTGRs). TRISO fuel is in general extremely rugged, and the coating layers in most particles are expected to effectively prevent fission product release. The ability of the fuel to contain fission products is largely dictated by the quality of the manufacturing process because most of the fission product release is expected to occur due to failure of coating layers a small number of particles at the locations of defects.

A basic capability for thermo-mechanical analysis of TRISO fuel has existed for some time [1], but prior to the present effort, Bison was missing the ability to address failure of particles to compute fission gas release. Developing such a capability was the focus of the fiscal year 2019 effort for TRISO development in Bison. The initial development of statistical treatment to determine failure probability in Bison was focused on the implementation of the PARFUME [2] code's approach to determine failure modes and the Monte Carlo scheme to calculate failure probability. This report documents the basic methodology and development of foundational capabilities needed for TRISO statistical failure calculation.

9.2 Particle Failure Mechanisms

There are several potential failure mechanisms for TRISO fuel, outlined in the sections below, that are considered in this modeling approach.

9.2.1 Pressure vessel failure

Early during irradiation, pyrocarbon layers shrink and put the SiC layer in compression. As irradiation progresses, the creep of the pyrocarbon layers tends to relax some of this compressive stress. In addition, the buildup of fission gas pressure tends to put the coating layers in tension. If the gas pressure becomes high enough, the tangential stress in the SiC layer could eventually become tensile. Failure due to overpressurization, i.e. a pressure vessel failure, occurs when the tangential stress exceeds the strength of the SiC. An example of the tangential stresses of IPyC, OPyC and SiC layers during operation is shown in Figure 9.1. In this figure, the stress in SiC layer remains compressive throughout the whole simulation.

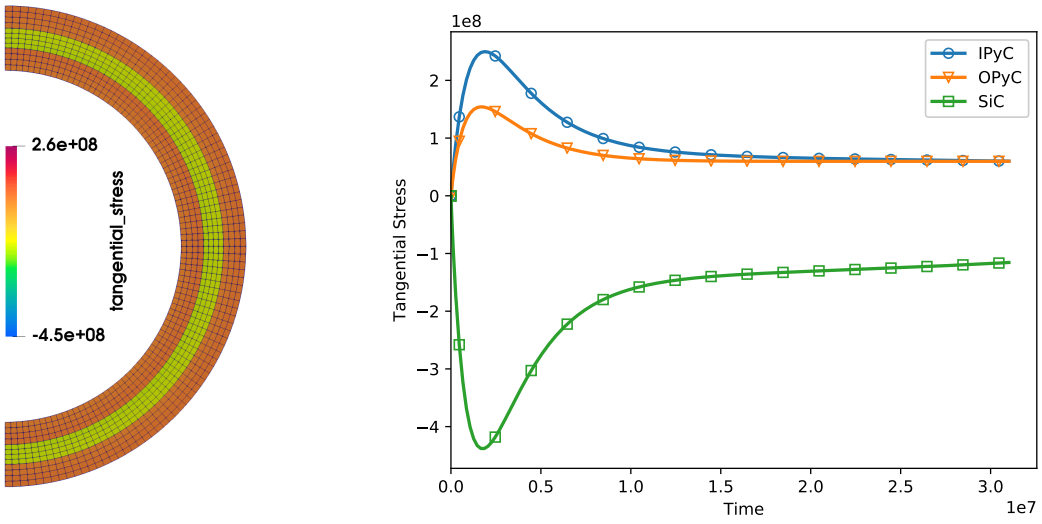

(a) (b)

Figure 9.1: Tangential stresses of IPyC, OPyC and SiC.

9.2.2 Cracking of IPyC and OPyC cracking

During irradiation, shrinkage of the pyrocarbon layers causes a significant tensile stress in those layers. If the stress exceeds the tensile strength of that material, a radial crack forms in that pyrocarbon layer. The radial crack leads to a high local tensile stress in the SiC layer adjacent to that cracked pyrocarbon layer that could lead to particle failure. As shown in Figure 9.2 and 9.3, the stress in the SiC layer near the crack tip is elevated significantly due to the development of cracking in the IPyC or OPyC layer.

9.2.3 Partial debonding of the IPyC from the SiC

During irradiation, the IPyC layer shrinks, which causes a radial tensile stress at the interface between the IPyC and SiC layers. If the stress exceeds the strength of the bond between those layers, then debonding of the IPyC from the SiC occurs. As shown in Figure 9.4, a stress concentration occurs in the SiC layer at the edge of the debonded region, which could lead to SiC failure.

9.2.4 Pressure vessel failure of an aspherical particle

A single flat facet on one side of the particle created during fabrication is a common cause of aspherical behavior in particle fuel. The degree of asphericity for a particle is measured by the aspect ratio $A = 2R/(R+\sqrt{R^2-r^2})$ (see Figure 9.5). In an aspherical particle, the stresses in the faceted portions are elevated, which can lead to particle failure.

9.2.5 Kernel migration

Kernel migration occurs due to the presence of a temperature gradient. For UCO fuel, kernel migration is minuscule, while for UO_2 fuel, kernel migration is significant. The migration distance is computed as $\int_0^t K_{MC}(T)\frac{1}{T(\tau)^2}\frac{dT(\tau)}{dx}d\tau$ and is implemented as `TRISOKernelMigration PostProcessor` in Bison. Particle failure is assumed to occur when the kernel comes into contact with the SiC layer.

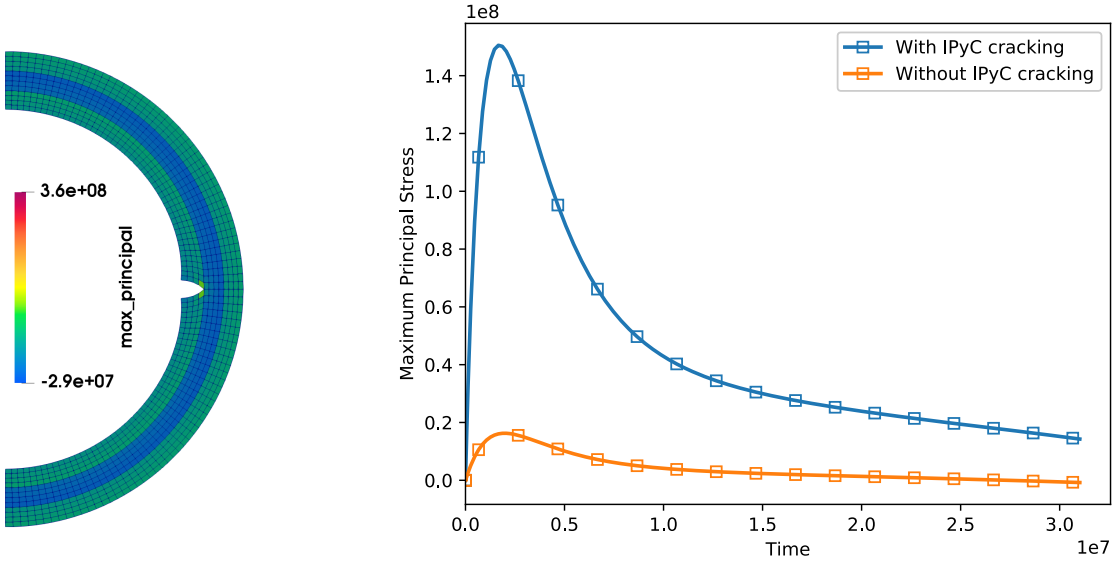

(a) (b)

Figure 9.2: Maximum principal stress near IPyC crack tip.

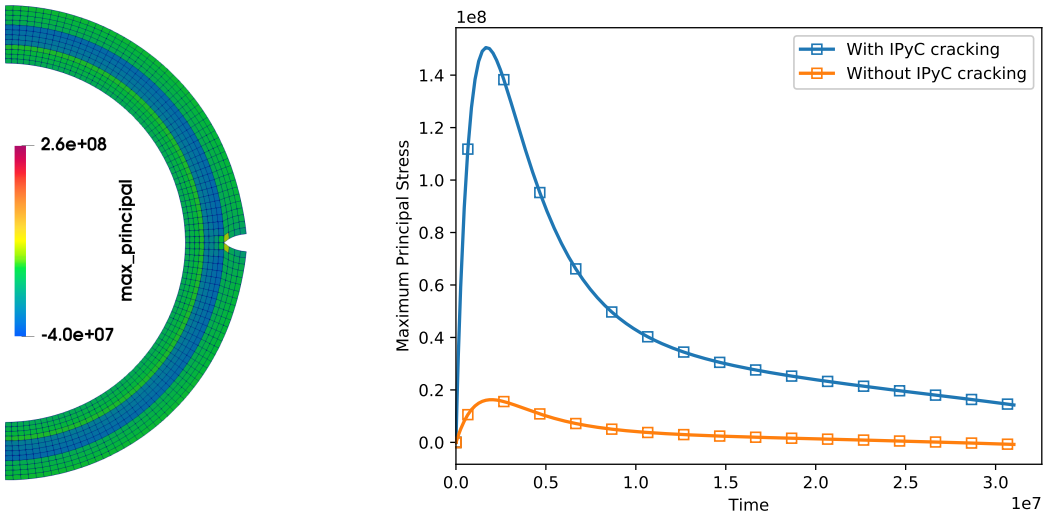

(a) (b)

Figure 9.3: Maximum principal stress near OPyC crack tip.

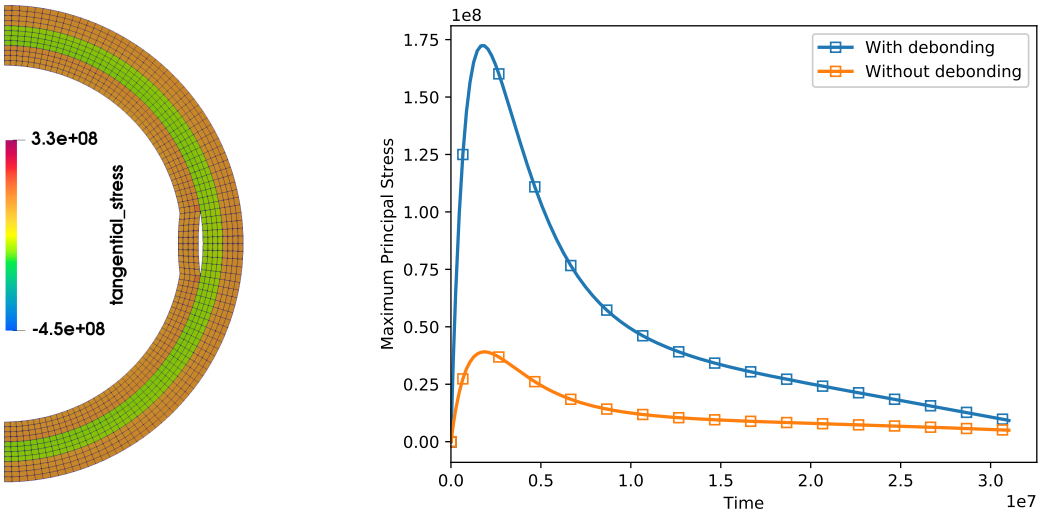

(a) (b)

Figure 9.4: Maximum principal stress near debonding tip.

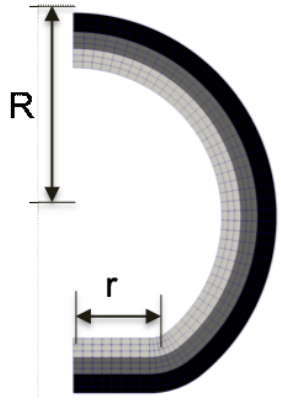

Figure 9.5: Aspect ratio of an aspherical particle.

9.2.6 Thinning of the SiC layer

Thinning of the SiC layer is caused by either thermal decomposition or interaction with fission products, associated mainly with accident conditions at high temperatures. The tensile stresses are elevated[1] through the entire SiC layer cross-section in the vicinity of the thinned regions, which can lead to particle failure.

9.3 Implementation of Particle Failure Model

9.3.1 Weibull Failure Theory

A Weibull failure criterion is used to determine vessel failure for the inner pyrolytic carbon (IPyC) layer, silicon carbide (SiC) layer and outer pyrolytic carbon (OPyC) layer. The maximum stress σ_c is compared to a strength that is sampled from a Weibull distribution having mean strength σ_{ms} to determine whether or not failure occurs. The

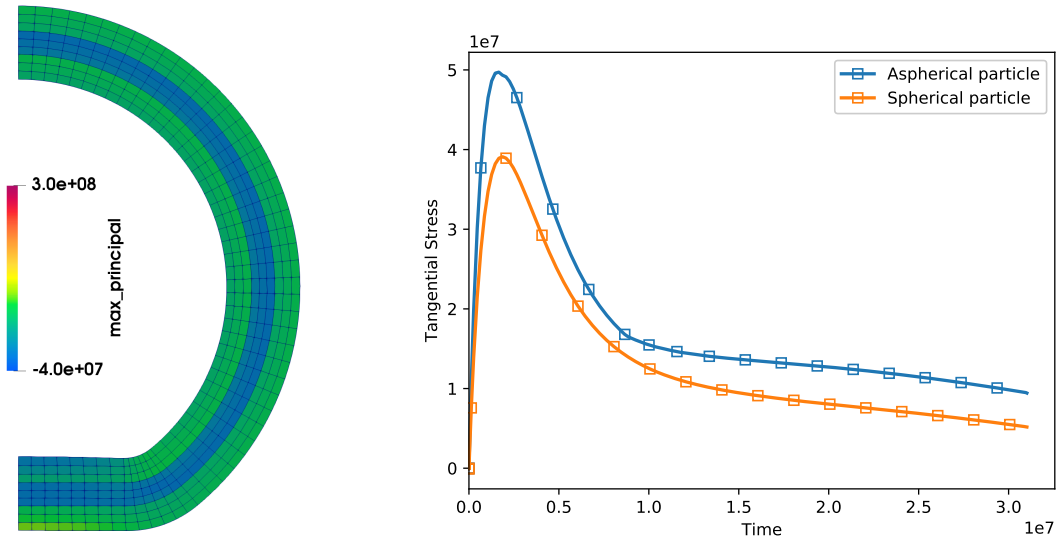

(a) (b)

Figure 9.6: Maximum principal stress in a aspherical particle.

effective mean strength σ_{ms} is given as:

$$\sigma_{ms} = \frac{\sigma_0}{I_n^{\frac{1}{m}}}, \tag{9.1}$$

where σ_0 is the characteristic strength, m is the Weibull modulus. The integral I_n is a normalized integration of the stress distribution using the principle of independent action (PIA) model as follows:

$$I_n = \frac{\int_V (\sigma_1^m + \sigma_2^m + \sigma_3^m) dV}{\sigma_c^m} \tag{9.2}$$

where σ_c is the maximum value calculated for a principal stress anywhere in the volume and σ_1, σ_2 and σ_3 are three principal stresses. The negative principal stresses are not included in this integral because the compressive stresses do not contribute to fracture. The effective mean strength and determinant of failure is implemented as `WeibullEffectiveMeanStrength` and `WeibullFailureIndicator`, respectively.

9.3.2 High-fidelity analysis

For computational efficiency, it is important that the fuel performance calculations are primarily conducted using 1D models because they are run within a Monte Carlo sampling procedure. However, the stress concentrations due to the presence of phenomena such as cracking must be characterized using a higher-dimensionality, higher fidelity model. To account for these multi-dimensional phenomena within a 1D fuel performance model, a high-fidelity analysis is first performed to obtain the mean strength based on the multi-dimensional stress distribution and stress correlation factor. The stress correlation factor is defined as the ratio of maximum principal stress that is calculated in the multi-dimensional and one-dimensional simulations. The multi-dimensional strength and stress correlation factor are calculated prior to statistical modeling and then used as a time-dependent function that is used within the 1D model in `WeibullFailureIndicator` to determine failure. The flow diagram for this statistical approach is shown in Figure 9.7.

9.3.3 TRISO Failure Determination

`TRISOFailureEvaluation` checks failure of the IPyC, SiC and OPyC layers in a TRISO fuel particle at each time step. It returns a value of 1 if the TRISO particle fails, and 0 if it does not. If cracking of either the IPyC or OPyC

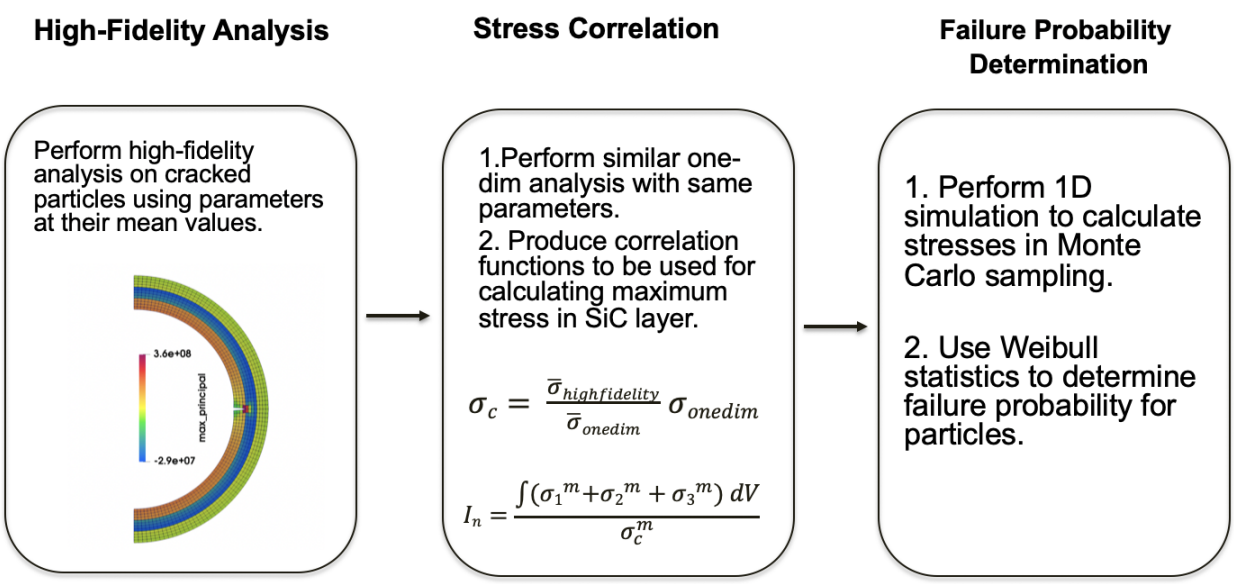

Figure 9.7: High-fidelity analysis and stress correlation.

layers occurs, the particle is checked for failure of the SiC due to the cracking of the IPyC and OPyC layers. If neither the IPyC nor OPyC layers fail, the particle is checked for failure of the SiC due to pressure. The current implementation considers failure mechanisms due to pressure vessel failure and cracking of the IPyC and OPyC, but can be easily extended to incorporate other mechanisms, such as debonding of the IPyC from the SiC, failure of an aspherical particle and kernel migration.

9.3.4 Monte Carlo Scheme for Predicting Failure

The Monte Carlo scheme to compute failure probability for a statistically sampled batch of particles is shown in Figure 9.8. For each realization of the randomized parameters, 1D TRISO model is run to compute stresses and determine whether failure has occurred. The final probability is computed as a ratio of number of failure particles to the total number of particles.

9.4 Monte Carlo Simulation in Bison

9.4.1 MOOSE Stochastic Tools Module

The MOOSE stochastic_tools module is designed for performing stochastic analysis for MOOSE-based applications. As shown in Figure 9.9, MOOSE's multi-app system is utilized here to perform Monte Carlo sampling. A number of other statistical tools are available for this purpose, and are capable of performing sampling and driving a code such as Bison. The decision to use MOOSE for this purpose for Bison TRISO failure calculations was driven by performance considerations. In this case, the individual analyses are relatively computationally inexpensive (around 10 s on a single processor). However, because failure probabilities are expected to be very low, a very large number of samples is potentially required for the Monte Carlo iterations to converge. Improvements were made to the MOOSE multi-app system that resulted in very low overhead costs for the probabilistic driver in terms of computation time and memory requirements.

In the MOOSE multi-app system, a master (`SamplerMasterApp`) and sub-application (`SamplerMultiApp`) are used, where the master application performs the sampling and drives the analyses, which are performed by the sub-application. In `SamplerMasterApp`, a distribution for each random variable is specified. The sampled data is then passed to each SamplerMultiApp to set random variable values. Each SamplerMultiApp computes maximum stress

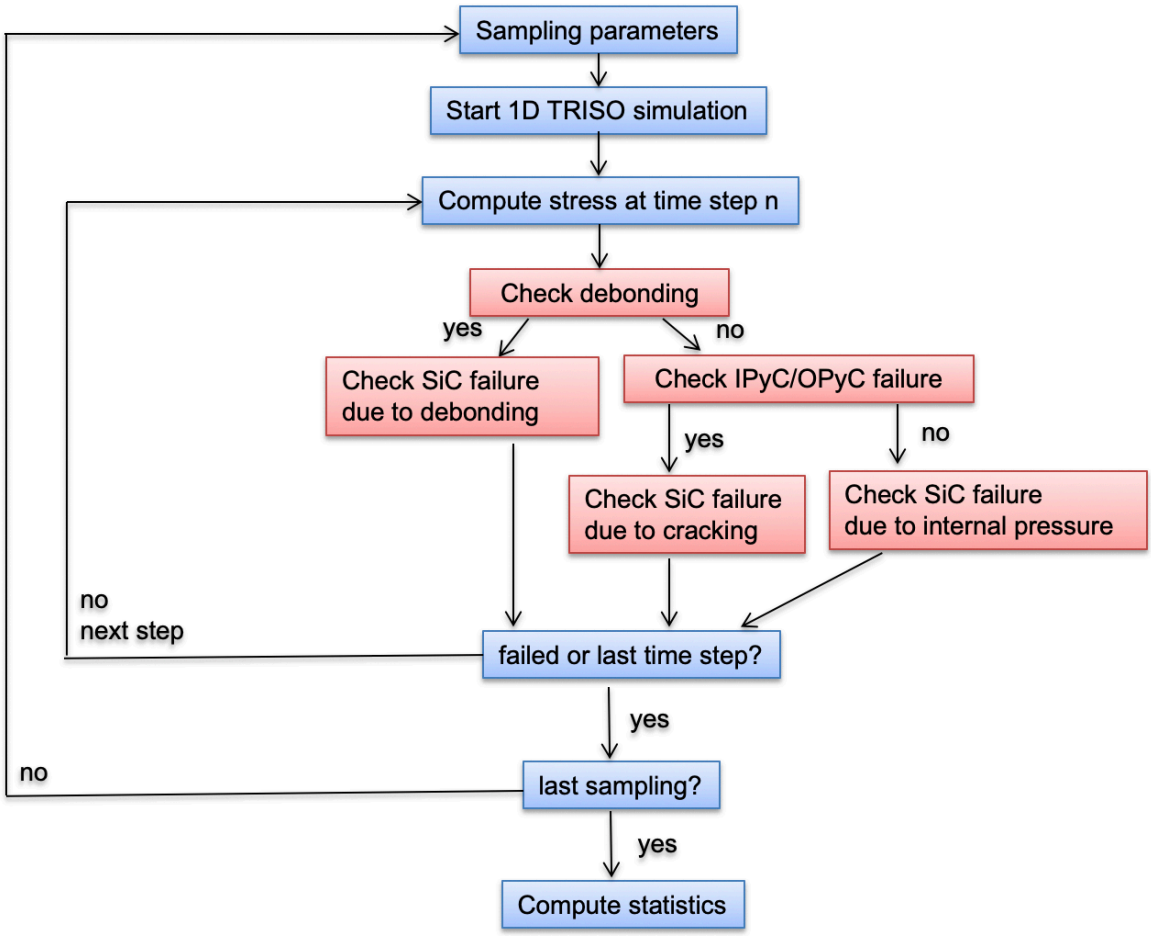

Figure 9.8: Monte Carlo Scheme Solution scheme in Bison

and determines whether failure has occurred based on Weibull theory. The failure index for each sampler is transferred back to `SamplerMasterApp` to compute the failure probability of a population of particles.

9.4.2 Improvements to the MOOSE Sampler Multi-app System

A number of improvements to MOOSE's statistical sampling system needed to be made to permit its use for this application, as described below.

9.4.2.1 MultiAppCommandLineControl

Prior to the present work, MOOSE relied on the `Control` system, which alters parameters of an already initialized analysis model to set the randomized values of parameters. However, this system proved to not be sufficiently flexible for the Bison TRISO application. To account for statistical variation in physical dimensions from particle to particle, the layer thickness in the `TRISOFiveLayersMesh` block is required to be altered. However, this value could not be altered from within sub-application input file via a Control object because the parameter is applied to the mesh when it is created. By the time that the `Control` system usually modifies the parameters in the sub-model, the mesh had already been created, and could not be modified to take into account a randomly sampled variable.

To address this issue, a new approach called `MultiAppCommandLineControl` was developed. This technique passes the randomized values in as command-line arguments to the sub-app, which means that all randomized input parameters can be set at the very beginning of the sub-app's execution. This enabled the mesh dimension parameters to be altered in the sampled Bison analyses.

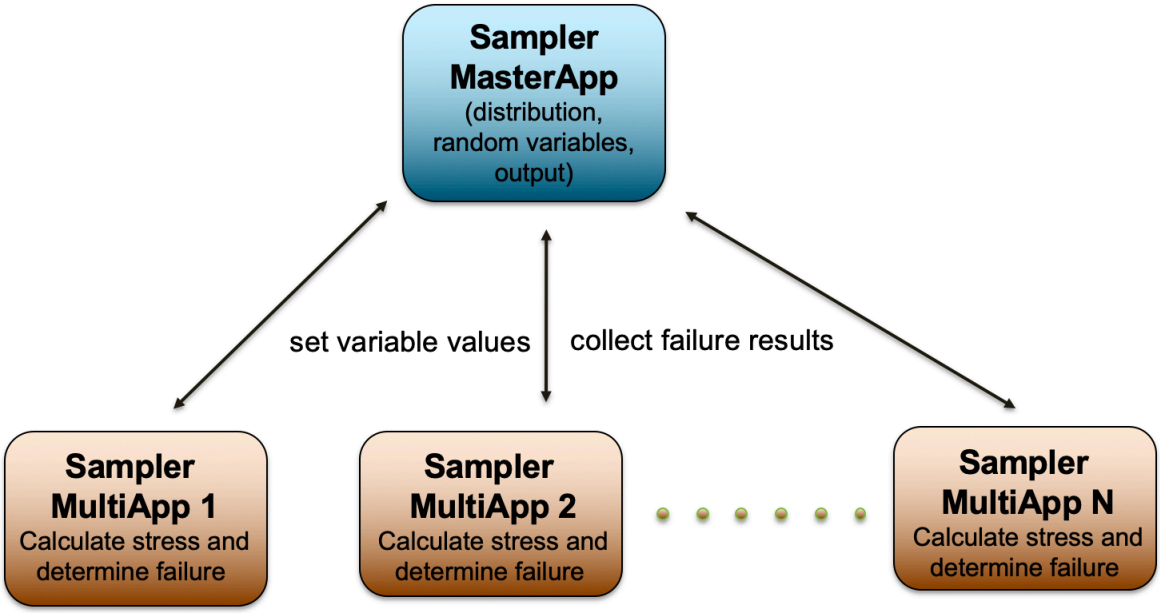

Figure 9.9: MOOSE sampler `MultiApp` system.

9.4.2.2 Stochastic Tools Batch Mode

Prior to the present work, MOOSE's stochastic system created instances of all sub-applications that are driven by the master application, which required that there was sufficient memory for all of the sub-applications. When a large number of samples are required, as in the TRISO failure application, this requires an amount of memory that far exceeded the available system resources.

To address this issue, a new capability of running sub-applications in "batch-reset" mode has been added to the sampler system to work in conjunction with `MultiAppCommandLineControl`. In "batch-reset" mode, one sub-application is created for each processor, and this sub-application is destroyed and re-created for each row of data supplied by the Sampler object. The primary benefit to using a batch mode is to improve performance of a simulation by drastically reducing the memory requirement. This is illustrated in the results of a performance evaluation in terms of memory usage and execution time with different number of Monte Carlo samples shown in Figures 9.10 and 9.11.

9.4.3 Preliminary Monte Carlo Simulation in Bison

To demonstrate the use of MOOSE's built-in Monte Carlo sampling in conjunction with the models to predict particle failure in Bison, a representative TRISO model was evaluated with the randomized parameters listed in Table 9.4.3 using INL's high performance computing resources. The scalability of the simulations in parallel, which is very good, is shown in Figure 9.12. A standalone 1D TRISO simulation takes about 6.2 seconds while average time for each 1D TRISO simulation within Monte Carlo consisting of 10 million samples is about 7.66 seconds. The overhead is less than 2 seconds per realization. The source of this overhead still needs to be identified, but it is possibly associated with `MultiApp` initialization and data transfer. It is desirable to further minimize that overhead, and this will be further investigated in the future.

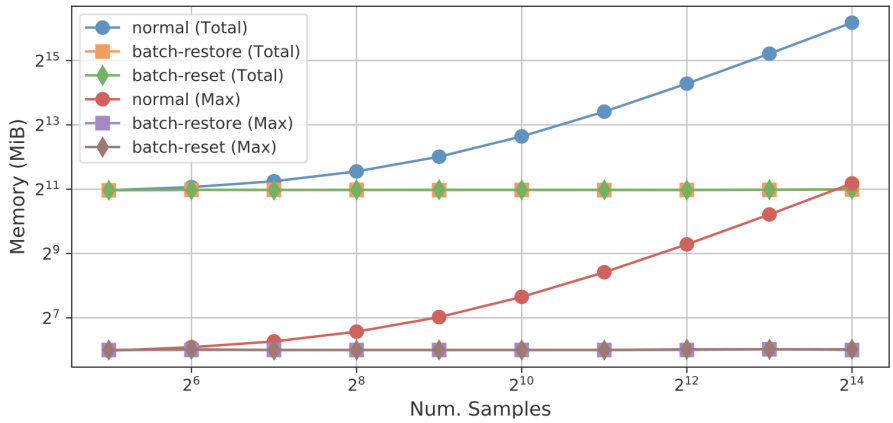

Figure 9.10: Total memory and maximum memory per processor at the end of the simulation using a SamplerFullSolveMultiApp with increasing number of Monte Carlo samples for the three available modes of operation running on 32 processors.

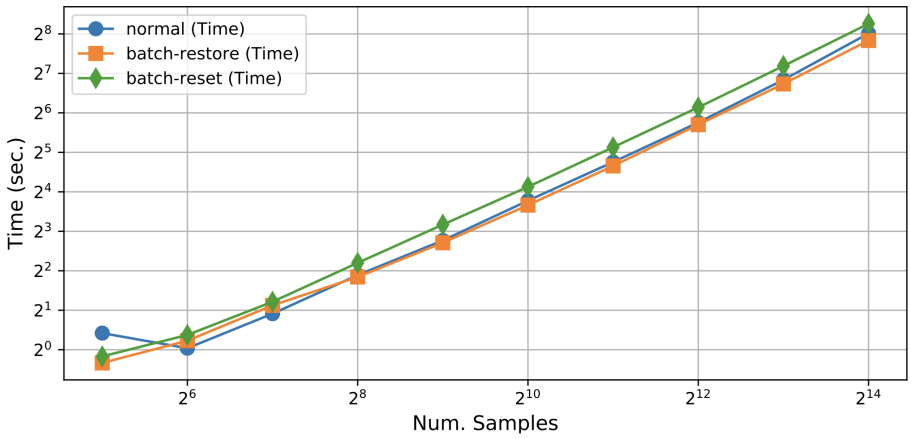

Figure 9.11: Total execution time of a simulation using SamplerFullSolveMultiApp with increasing number of Monte Carlo samples for the available modes of operation on 32 processors.

Attribute	Unites	Value
Kernel diameter	μ m	425±10
Buffer thickness	μ m	100±10
IPyC thickness	μ m	40±4
SiC thickness	μ m	35±3
OPyC thickness	μ m	40±4
IPyC density	μ g/m^3	1.90±0.02
OPyC density	μ g/m^3	1.90±0.03
SiC Weibull modulus		6
IPyC/OPyC Weibull modulus		9.5
SiC characteristic strength	MPa-m$^{3/m}$	16.8
IPyC/OPyC characteristic strength	MPa-m$^{3/m}$	9.64

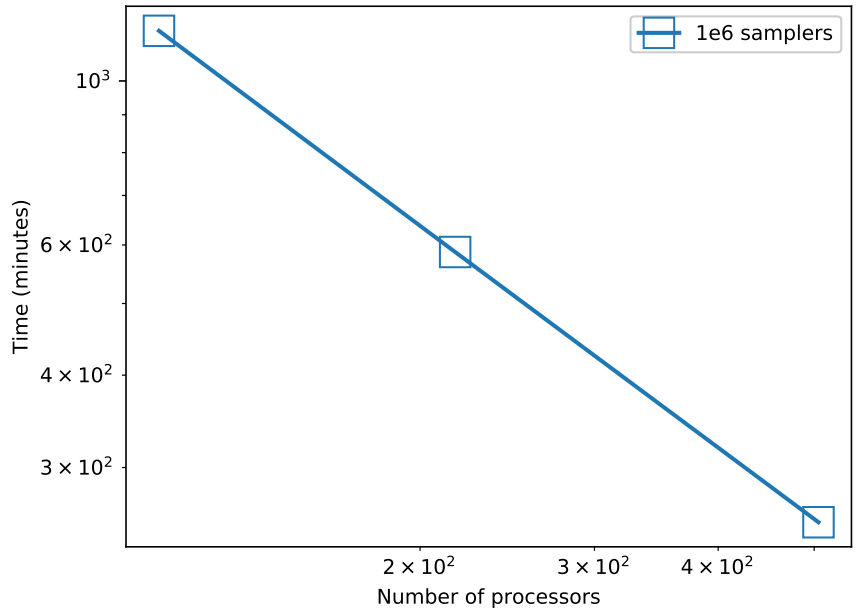

Figure 9.12: Scalability of parallel simulation.

9.4.4 Future Scope

The current TRISO failure model implementation has focused on pressure vessel failure due to cracking of the IPyC and OPyC layers. Other failure mechanisms, such as debonding of the IPyC layer from the SiC layer, failure of an aspherical particle, kernel migration and thinning of SiC, also need to be considered, and will be implemented using a similar process. An initial demonstration of this capability has been demonstrated, but the accuracy of this approach still needs to be verified. This will be done in part by benchmarking Bison's failure probability analysis against PARFUME [2] results.

There is also a need for more realistic modeling of the mechanisms of cracking and debonding, which are currently being performed using 2D models, but should be modeled in 3D. High-fidelity cracking and debonding modeling will be performed in Bison to improve the understanding of these failure mechanism. In addition, development will continue to optimize the performance of Bison's capability to perform statistical fuel particle failure analysis.

Bibliography

[1] J.D. Hales, R.L. Williamson, S.R. Novascone, D.M. Perez, B.W. Spencer, and G. Pastore. Multidimensional multiphysics simulation of triso particle fuel. *Journal of Nuclear Materials*, 443(1):531 – 543, 2013.

[2] Darrell L. Knudson, Gregory K Miller, G.K. Miller, D.A. Petti, J.T. Maki, and D.L. Knudson. Parfume theory and model basis report. 9 2009.

Chapter 10

Particle fuel validation plan

S. R. Novascone

The purpose of this document is to establish the initial validation plan for simulating particle fuel using Bison. The plan is based on an IAEA document summarizing advances in high temperature gas cooled reactors [1], in which many experiments are described along with presentation of corresponding measurements and fuel performance simulation results. Sixteen benchmark cases were identified, ranging in complexity from a simple fuel kernel having a single elastic coating layer, to realistic TRISO-coated particles under a variety of irradiation conditions. In each case, the particle geometry, constitutive relations, material properties and operating conditions were carefully prescribed to minimize differences between the various code predictions. The plan presented here is to use Bison to essentially reproduce what is found in [1] and show how Bison compares to other fuel performance codes and experiment measurements.

10.1 Background on the high temperature fast reactor IAEA Coordinated Research Project (CRP-6)

The purpose of this CRP was for many countries to present their experiment measurements and corresponding computer models for the purpose of comparing and mutually advancing high temperature gas cooled knowledge. As stated in [1], the objectives were:

- Support the development of improved HTGR fuel technology
- Facilitate the coordination of technology development activities
- Exchange relevant technical information among the interested Member States

The outcome of the project was successful in that it provided a platform for quantifying the value of computer models by comparing them to each other and to measurements from experiments.

10.2 CRP-6 validation cases

10.2.1 Thermo-mechanics

Table 10.1 briefly describes the benchmark cases we chose to run. A detailed discussion of the benchmarks can be found in sections 9 and 10 of [1]. Section 9 is titled "Benchmarking of fuel performance models during normal operation and operational transients", where all of the codes and the benchmark calculations are described. The models are all essentially 1D spherical thermo-mechanics calculations with irradiation effects considered. As such, figures of merit are temperature, stress, and deformation.

Cases 1-8 of Section 9 are benchmarks for normal operations and cases 9-13 are benchmarks for operational transients. In cases 1-7 the analytical benchmark problems meant to calibrate the codes all compared well with the corresponding closed-form solutions. Case 8 included accounting for cyclic temperature history that is characteristic

Table 10.1: IAEA CRP-6 benchmark cases considered in the Bison coated-particle verification exercise. HFR-K3 and HFR-P4 are German pebble and fuel element experiments, respectively.

Case	Geometry	Description
1	SiC layer	Elastic only
2	IPyC layer	Elastic only
3	IPyC/SiC	Elastic with no fluence
4a	IPyC/SiC	Swelling and no creep
4b	IPyC/SiC	Creep and no swelling
4c	IPyC/SiC	Creep and swelling
4d	IPyC/SiC	Creep- and fluence-dependent swelling
5	TRISO	350 μm kernel, real conditions
6	TRISO	500 μm kernel, real conditions
7	TRISO	Same as 6 with high BAF PyC
8	TRISO	Same as 6 with cyclic temperature
10	HFR-K3	10% FIMA, 5.3×10^{-25}n/m^2 fluence
11	HFR-P4	14% FIMA, 7.2×10^{-25}n/m^2 fluence

for fuel in a pebble bed, and the codes compared well to each other. Cases 9-13 were simulations of real irradiation experiments and there were major differences between the codes.

Some of this work has been completed and documented in [2]. As an example, Figure 10.1 compares solutions for case 8, which involved a cyclic particle temperature, during the full irradiation history. In this figure, Bison solutions of the tangential stress at the inner wall of the IPyC and SiC layers are compared to solutions from three codes from the CRP-6 exercise, namely PARFUME [3], ATLAS [4] and STRESS3 [5]. As above, data for the code comparisons were extracted from plots in [1]. For the IPyC layer, the four solutions essentially overlay each other during the entire irradiation period. In the SiC layer, the four solutions are quite similar but some differences are evident, particularly for the first four temperature cycles. The Bison solution falls roughly midway between the PARFUME and STRESS3 solutions and is essentially identical to the ATLAS solution.

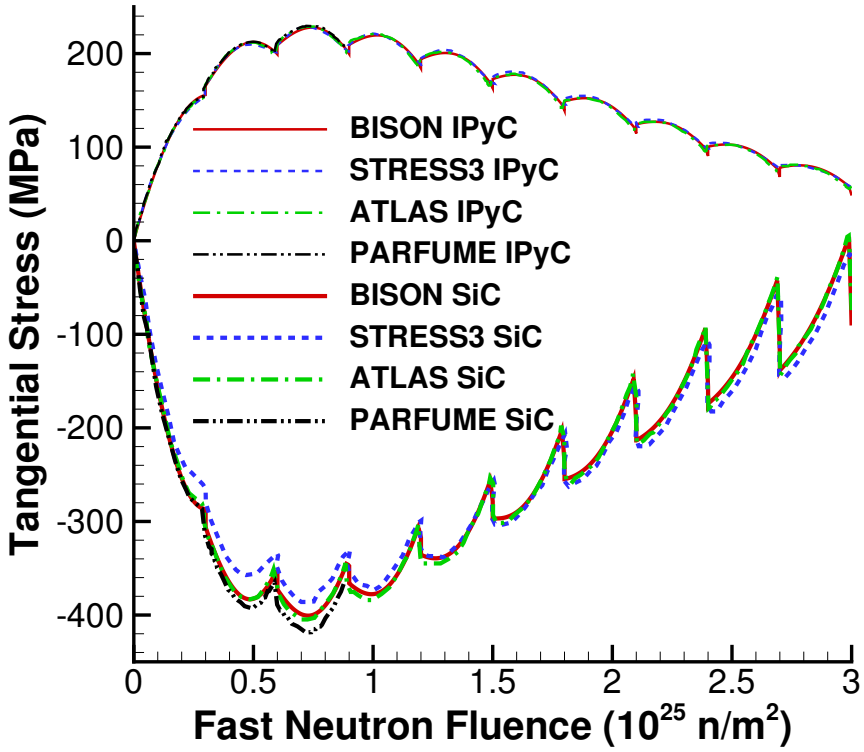

Figure 10.1: Code comparison for case 8, which included a ten cycle temperature history. Plotted is the tangential stress at the inner wall of the IPyC and SiC layers.

10.2.2 Fission gas release

Section 10 of [1] focuses on modeling fission product release under accident conditions. The simulations focus on generation and diffusion of strontium, silver, cesium, krypton, iodine, and xenon using 1D spherical models. Results from these simulations were compared with post irradiation examination data. In a fashion similar to the prior section, we plan to simulate the experiments listed here and compare with the other codes and experiment measurements. The definition of the benchmark as stated in [1]:

- a sensitivity study to examine fission product release from a fuel particle starting with a bare kernel and ending with an irradiated TRISO particle
- the post-calculation of some well documented irradiation and heating experiments
- the prediction of heating tests which are planned for the future

The summary and conclusions in [1] of the benchmark are briefly stated here for context as we plan calculations:

- In the sensitivity study, most codes showed good agreement with each other
- The diffusion coefficient of cesium in SiC is uncertain
- The diffusion of strontium was over-predicted in most cases, and it's thought that the diffusion coefficient in the SiC layer is too conservative
- Silver release measurements are often unusual and inconsistent, which makes it very difficult to accurately simulate. It's thought that mechanisms other than diffusion are at play.
- Krypton and cesium levels are over-predicted

For reference, the tests used in [1] are listed here:

- RB (conducted at HFIR by ORNL): HRB-22
- HFR (conducted by Germany in the Petten HFR reactor): HFR-K3, HFR-P4, HFR-EU1, HFR-K6, and possibly HFR-EU1bis (16.7% U-235) and HTR-PM (8.9% U-235)
- NPR (conducted at HFIR by ORNL): NPR-1
- AGR (conducted at ATR by INL): AGR-1 and AGR-2 have been run. These use UCO kernels.
- Gen-IV benchmark TRISO fuel performance models under accident conditions (this contains AGR-1, AGR-2 and HFR-EU1bis data; INL external report draft)
- Select AGR-1 and AGR-2 data not covered by international benchmarks but that are relevant to KP-FHR (available through various INL and ORNL reports)

10.3 Summary

The Bison validation plan for particle fuel consists of following the verification and validation activities documented in the IAEA report summarizing advances in high temperature gas cooled reactors [1]. Initially, this will consist of thermo-mechanics and fission gas release calculations and comparisons to other codes and experiment measurements. We expect this plan to evolve as new information and requirements are received from the advanced reactor community. As such, we view this plan as a "living" document that will be updated as required to support simulation requirements.

Bibliography

[1] Advances in high temperature gas cooled reactor fuel technology. Technical Report IAEA-TECDOC-1674, IAEA, 2012.

[2] J. D. Hales, R. L. Williamson, S. R. Novascone, D. M. Perez, B. W. Spencer, and G. Pastore. Multidimensional multiphysics simulation of TRISO particle fuel. *Journal of Nuclear Materials*, 443:531–543, 2013.

[3] G. K. Miller, D. A. Petti, J. T. Maki, , and D. L. Knudsen. PARFUME theory and model basis report. Technical Report INL/EXT-08-14497, Idaho National Laboratory, 2009.

[4] M. Phelip, F. Michel, M. Pelletier, G. Degeneve, and P. Guillermier. 2nd international topical meeting on high temperature reactortechnology. In *The ATLAS HTR fuel simulation code objectives, description and first results*, Beijing, China, September 2004.

[5] D. G. Martin. Considerations pertaining to the achievement of high burn-ups in HTR fuel. *Nuclear Engineering and Design*, 213:241–258, 2002.

Chapter 11

Convert existing validation cases to new Bison documentation system

D. J. McDowell

11.1 Background

In the past, Bison validation cases were typeset using LaTeX and distributed as .pdf files. While this generally is an accepted form of documentation and information consumption. The Bison team felt efforts could be made to make the documentation more dynamic, accessible, and consistent across the Bison framework. Over the past year, Bison documentation has migrated from using distributed .pdf files to leveraging the MooseDocs documentation framework. This framework compiles all Bison documentation ranging from syntax to introductory examples. By converting the existing validation cases to utilize this framework, users will experience a comprehensive overview of the Bison universe and aid in its adoption in research and industrial settings.

11.2 Migrating Documents to the New Bison System

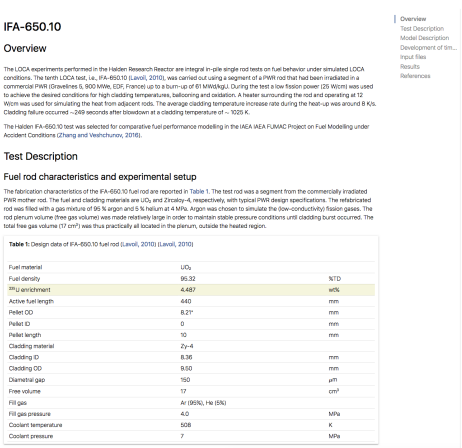
IFA-650.10

Overview

The LOCA experiments performed in the Halden Research Reactor are integral in-pile single rod tests on fuel behavior under simulated LOCA conditions. The tenth LOCA test, i.e., IFA-650.10 (Lavoil, 2010), was carried out using a segment of a PWR rod that had been irradiated in a commercial PWR (Gravelines 5, 900 MWe, EDF, France) up to a burn-up of 61 MWd/kgU. During the test a low fission power (25 W/cm) was used to achieve the desired conditions for high cladding temperatures, ballooning and oxidation. A heater surrounding the rod and operating at 12 W/cm was used for simulating the heat from adjacent rods. The average cladding temperature increase rate during the heat-up was around 8 K/s. Cladding failure occurred ~249 seconds after blowdown at a cladding temperature of ~ 1025 K.

The Halden IFA-650.10 test was selected for comparative fuel performance modelling in the IAEA IAEA FUMAC Project on Fuel Modelling under Accident Conditions (Zhang and Veshchunov, 2016).

Test Description

Fuel rod characteristics and experimental setup

The fabrication characteristics of the IFA-650.10 fuel rod are reported in Table 1. The test rod was a segment from the commercially irradiated PWR mother rod. The fuel and cladding materials are UO_2 and Zircaloy-4, respectively, with typical PWR design specifications. The refabricated rod was filled with a gas mixture of 95 % argon and 5 % helium at 4 MPa. Argon was chosen to simulate the (low-conductivity) fission gases. The rod plenum volume (free gas volume) was made relatively large in order to maintain stable pressure conditions until cladding burst occurred. The total free gas volume (17 cm³) was thus practically all located in the plenum, outside the heated region.

Table 1: Design data of IFA-650.10 fuel rod (Lavoil, 2010) (Lavoil, 2010)

Fuel material	UO_2	
Fuel density	95.32	%TD
^{235}U enrichment	4.487	wt%
Active fuel length	440	mm
Pellet OD	8.27*	mm
Pellet ID	0	mm
Pellet length	10	mm
Cladding material	Zy-4	
Cladding ID	8.36	mm
Cladding OD	9.50	mm
Diametral gap	150	μm
Free volume	17	cm³
Fill gas	Ar (95%), He (5%)	
Fill gas pressure	4.0	MPa
Coolant temperature	508	K
Coolant pressure	7	MPa

Overview
Test Description
Model Description
Development of tim...
Input files
Results
References

Figure 11.1
Example of converted document showing tables

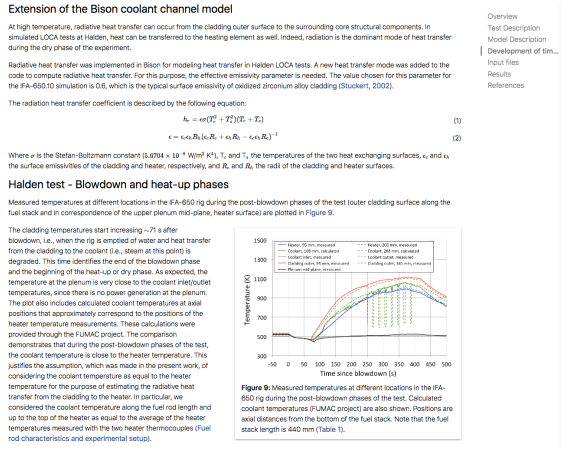
Extension of the Bison coolant channel model

At high temperature, radiative heat transfer can occur from the cladding outer surface to the surrounding core structural components. In simulated LOCA tests at Halden, heat can be transferred to the heating element as well. Indeed, radiation is the dominant mode of heat transfer during the dry phase of the experiment.

Radiative heat transfer was implemented in Bison for modeling heat transfer in Halden LOCA tests. A new heat transfer mode was added to the code to compute radiative heat transfer. For this purpose, the effective emissivity parameter is needed. The value chosen for this parameter for the IFA-650.10 simulation is 0.6, which is the typical surface emissivity of oxidized zirconium alloy cladding (Stuckert, 2002).

The radiation heat transfer coefficient is described by the following equation:

$$h_r = \sigma\varepsilon\left(T_c^2 + T_h^2\right)\left(T_c + T_h\right) \quad (1)$$

$$\epsilon = \epsilon_c \epsilon_h R_h \left(\epsilon_c R_c + \epsilon_h R_h - \epsilon_c \epsilon_h R_c\right)^{-1} \quad (2)$$

Where σ is the Stefan-Boltzmann constant (5.6704×10^{-8} W/m² K⁴), T_c and T_h the temperatures of the two heat exchanging surfaces, ϵ_c and ϵ_h the surface emissivities of the cladding and heater, respectively, and R_c and R_h the radii of the cladding and heater surfaces.

Halden test - Blowdown and heat-up phases

Measured temperatures at different locations in the IFA-650 rig during the post-blowdown phases of the test (outer cladding surface along the fuel stack and in correspondence of the upper plenum mid-plane, heater surface) are plotted in Figure 9.

The cladding temperatures start increasing ~71 s after blowdown, i.e., when the rig is emptied of water and heat transfer from the cladding to the coolant (i.e., steam at this point) is degraded. This time identifies the end of the blowdown phase and the beginning of the heat-up or dry phase. As expected, the temperature at the plenum is very close to the coolant inlet/outlet temperatures, since there is no power generation at the plenum. The plot also includes calculated coolant temperatures at axial positions that approximately correspond to the positions of the heater temperature measurements. These calculations were provided through the FUMAC project. The comparison demonstrates that during the post-blowdown phases of the test, the coolant temperature is close to the heater temperature. This justifies the assumption, which was made in the present work, of considering the coolant temperature as equal to the heater temperature for the purpose of estimating the radiative heat transfer from the cladding to the heater. In particular, we considered the coolant temperature along the fuel rod length and up to the top of the heater as equal to the average of the heater temperatures measured with the two heater thermocouples (Fuel rod characteristics and experimental setup).

Figure 9: Measured temperatures at different locations in the IFA-650 rig during the post-blowdown phases of the test. Calculated coolant temperatures (FUMAC project) are also shown. Positions are axial distances from the bottom of the fuel stack. Note that the fuel stack length is 440 mm (Table 1).

Overview
Test Description
Model Description
Development of tim...
Input files
Results
References

Figure 11.2
Example of converted document showing figures

The conversion between .tex to .md files was largely automated using the open-source, command-line utility pandoc [1]. Pandoc ensured the documents were converted correctly while maintaining information previously stored in tables or figures. This minimized issues such as typos and trailing white-space that may have been common if the

migration was done manually. Several personal elisp macros were also used to make minor changes to the markdown document. This allowed the new document to be in accordance with idiomatic MooseDocs.

Despite the programmatic approach, a few edge-cases, not handled by pandoc, produced minor errors throughout the documents which were dealt with manually. Examples such as figure sizing and alignment needed to be dealt with manually since the web layout was vastly different from the validation cases' original layout.

Several interactive features were added during the migration: Material and behavioral model documentation can now be accessed directly through hyperlinks while reading validation cases; Figures can now be toggled to enlarge for closer inspection and tables highlight current row on mouse-hover.

11.3 Inclusion of Helper Functions to Aid in Reproducibility

As mentioned above, the process of migration was largely automated using several command line utilities and text-editor macros. These tools would allow future users to migrate other LaTeX documents over to markdown if needed. This section will dive into some of the more technical details so that it can be replicated in the future.

Users can download pandoc directly from its website or use any package-manager such as `homebrew` or `apt-get`. A function can then be defined in the user's `.bashrc` as such:

```
convert_to_md() { pandoc --ascii -f latex -t markdown-multiline_tables-simple_tables --atx-headers -o
    "\$1" "\$2";}
```

The function `convert_to_md()` will take two parameters. The first being the name of the new markdown file being created, and the second being the existing .tex file that needs to be converted. The flags involved in this command seem to produce a document closest to idiomatic MooseDown. MooseDown requires tables, characters, and headings to be formatted a particular way. Ultimately, it would take extensive development work to have pandoc convert directly from LaTeX to MooseDown but this method gets extremely close. Further research could show additional flags that may be useful.

Once the document has been converted there typically will be some manual changes that can be addressed with a simple find and replace algorithm used by any modern text-editor. It's important to note that MooseDocs does not currently render Unicode characters, (hence the `--ascii` flag in the above function) thus, all Unicode characters are converted to its ascii equivalent. Sometimes pandoc goes to far and converts non-Unicode characters. This would be an example of using find and replace to manually fix up the document.

Other manual changes are often context dependent. This requires scanning through the document and recreating odd references and citations. This is the most manual part of the whole process and requires the most time.

Finally, pandoc does not have the capabilities to format figures the way MooseDown requires. Without the help of scripts or macros this would consume the user's time by having to retype, in correct format, the references to all the images throughout the document. To save time and increase Reproducibility, an elisp macro was written to speed this process up. The user must use the text-editor, Emacs, and save the following code in their `.emacs.d/init.el` file:

```
  (defun markdown-to-moosedown-image ()
  "Convert a Markdown image element to MooseDown format."
  (interactive "@*")
  ;; Look for a Markdown image element before the cursor or immediately
  ;; after the cursor. Don't look any further than the start of the current
  ;; paragraph.
  (let ((limit (save-excursion
                 (backward-paragraph)
                 (point)))
        (regexp "\\s-*!\\[\\([^][]*\\)\\](\\([^()]*\\))\\({[^}{]*}\\)?"))
    (if (and (eq ?! (char-after (1- (point))))
             (eq ?\[ (char-after (point))))
        (backward-char))
    (while (not (looking-at regexp))
      (search-backward "![" limit))
    ;; If the search didn't error out, then we exited the loop with
    ;; 'looking-at' matching 'regexp'. The match data therefore contains
    ;; the parts of the image link.
    (skip-syntax-forward "-")
    (let ((caption (subst-char-in-string ?\n ?\ (match-string 1)))
          (id (match-string 2))
          (style (and (match-string 3)
                      (substring (match-string 3) 1 -1))))
      ;; Remove the Markdown syntax.
      (delete-region (- (match-beginning 1) 2) (match-end 0))
      ;; Add line breaks before and after if it looks like there aren't any.
      (unless (eolp)
        (open-line 1))
      (unless (<= (point) (save-excursion
                            (back-to-indentation)
                            (point)))
        (insert "\n"))
      ;; Insert the new syntax.
      (insert "!media figures/" id ".png\n"
              "    id=" id "\n"
              "    caption=" caption)
      (when style
        (insert "\n   style=width:50%")))))

;; Key Mapping for above function
(defun my-eval-after-load-markdown-mode ()
  (define-key markdown-mode-map "\C-ci" 'markdown-to-moosedown-image))
(eval-after-load "markdown-mode" '(my-eval-after-load-markdown-mode))
```

By placing the cursor at the beginning of the image reference, the user can use the command `C-c i` to convert the reference to MooseDown format automatically.

11.4 Conclusion

In total, over 46 validation cases were converted over to the new documentation system and now currently reside on the Bison development branch. This was the final step in converting all existing documentation to the new system. All future documentation will be implemented using MooseDocs.

11.5 Future Work

Future work to improve the dynamic nature of the validation cases will be the implementation of an automated plotting script. This script will combine experimental and Bison simulation data to show users up-to-date figures of recent Bison runs. This update will ease updating the validation cases and keep all interested parties informed on the performance of Bison.

Additional future work will be to implement a system to convert validation cases back to LaTeX in order to be distributed as a .pdf. Being able to move between document formats easily will only aid in our ability to disperse the documentation in easy to consume formats despite the situation.

Bibliography

[1] Pandoc Development Team. *Pandoc: the swiss-army knife for converting files from one markup format into another.*, 2019.

Chapter 12

Activities

The activities for FY19 are listed in Table 12.1. They are listed (roughly) in order of activities that added content to the code followed by routine maintenance/improvements and user support activities.

Table 12.1: FY-2019 Activities for NEAMS INL-engineering scale fuel performance effort

Milestone	Completion Date
Improve frictional contact	5/30
Adapt XFEM to simulate moving material interface	4/28
Improve code robustness and plan/implement rigorous material model testing for metallic fuel	9/15
Support MW-scale micro-reactor development and analysis	8/30
Improve code documentation and testing	9/30
User training and support	9/15
Provide training and support material model development (with focus on particle fuel)	9/30

12.1 Improve frictional contact

A. D. Lindsay

A new mortar implementation has been added to MOOSE, building off the previous work of John Peterson described in the technical report [1]. The new mortar implementation shows correct convergence properties for all finite element discretizations tested: P2P1, P2P0, P1P1, and P1P0. (P2 = second order Lagrange, P1 = first order Lagrange, P0 = constant monomial). Results of these studies and comparisons with the old mortar implementation can be found on the corresponding MOOSE issue. Along with displaying the correct convergence properties, the new mortar implementation automatically generates the mortar segment mesh, a feature which is essential for using mortar with a dynamically moving mesh, e.g. during most BISON simulations. New mortar also can be run with an arbitrary number of processes using a replicated mesh. Tests have been developed for solution continuity, gap heat conductance, periodic boundary conditions, and normal and tangential mechanical contact.

The new mechanical contact objects which inherit from mortar constraints employ MOOSE's automatic differentiation system in order to obtain as accurate a Jacobian as possible. The new objects also use what is known as a Nonlinear Complimentarity Problem (NCP) formulation with Lagrange multipliers (LMs) in order to enforce the mechanical contact constraints [2]. The motivation behind using NCP is to convert the inequality constraints inherent in mechanical contact into a non-smooth equality constraint that fits naturally into a Newton algorithm. More explicitly, NCP converts the general conditions:

$$a \geq 0 \tag{12.1}$$

$$b \geq 0 \tag{12.2}$$

$$ab = 0 \tag{12.3}$$

into

$$\phi(a,b) = 0 \tag{12.4}$$

where typical choices for $\phi(a,b)$ are the min function or the Fischer-Burmeister (FB) function:

$$\phi(a,b) = a + b - \sqrt{a^2 + b^2} \tag{12.5}$$

Current testing suggests that the min function is a good choice for enforcing normal contact conditions while the FB function is a good choice for tangential frictional slip-stick conditions.

For a preliminary evaluation of the NCP-LM-mortar contact formulation, a toy two-body problem was used. The problem consisted of a small block sliding down the surface of another much larger block in two-dimensions. The small block was 0.6 mm wide and 0.8 mm long and the large block was 0.6 mm wide and 20 mm long. Figure 12.1 illustrates the geometry and mesh used for all analyses.

The vertical displacement of the smaller block was decreased linearly with time while the horizontal displacement was varied sinusoidally such that periodic contact was made with the larger block. A comparison of the NCP-LM-mortar contact algorithm with a penalty node-face constraint algorithm is shown in Table 12.2 for a Coulomb friction model. The total number of non-linear iterations required to simulate about 9.5 contact cycles was 476 with the NCP-LM-mortar algorithm, approximately half of the 938 iterations required with the penalty node-face algorithm. The total amount of simulation time decreased by 33% with the new algorithm, demonstrating that the increase in solve efficiency significantly outweighs the added cost of generating a mortar mesh every residual and Jacobian evaluation. It is hoped that for more complex geometries and larger contact set, improvement in solve efficiency between the NCP-LM-mortar algorithm and older algorithms is even greater, perhaps allowing implementation of frictional models for BISON assessment cases that previously were limited to frictionless formulations.

Table 12.2: Comparison of new NCP-LM-mortar algorithm with existing penalty node-face contact constraint enforcement for the sliding block problem. A Coulomb model with a friction coefficient of 0.4 was used.

Algorithm	Solution time (arb. units)	Total non-linear iterations
NCP-LM-mortar	13.9	476
penalty node-face	20.7	938

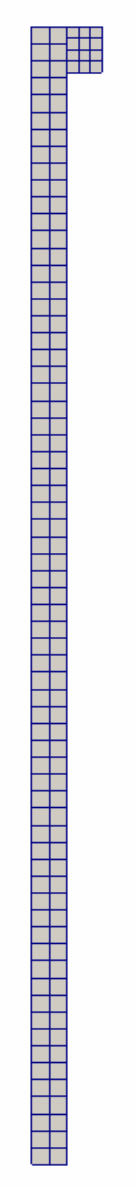

Figure 12.1: Geometry and mesh used for the sliding block tests.

Bibliography

[1] J. W. Peterson. Progress toward a new implementation of the mortar finite element method in MOOSE. Technical Report INL/EXT-17-44034-Rev000 TRN: US1902571, Idaho National Laboratory, 2018.

[2] Michael C Ferris and Jong-Shi Pang. Engineering and economic applications of complementarity problems. *Siam Review*, 39(4):669–713, 1997.

12.2 Adapt XFEM to simulate moving material interface

J. B. Tompkins

In an effort to accurately simulate thermomechanical transients in objects with discrete material interfaces that move over time, an investigation into utilizing the extended finite element method (XFEM) coupled with level sets is ongoing. Various phenomena in nuclear fuel could see modeling improvements as a benefit from this work as contemporary methods of modeling these processes are generally do not account for a loss of original material or changes in mechanical effects on the mesh. Phenomena that fit this description include corrosion, species diffusion, and phase changes in cladding materials as well as material relocation in fuel during burnup.

By using dimensional components of the rate by which material changes grow as a velocity term to advect a level set function, ϕ:

$$\frac{\partial \phi}{\partial t} + \overrightarrow{v} \cdot \nabla \phi = 0 \ , \tag{12.6}$$

that separates two material regions into either positive or negative level set values, the position of the material interface can be determined at each timestep by calculating the location of zero values of the level set function. The XFEM Moose module can then make cuts through the elements upon which the interface resides based on these zero value locations on the newly moved level set function, separating the mesh into discrete regions each with their own material properties assigned. Previous cuts may be "moved" thanks to recent additions of healing methods in the XFEM Moose module. Elements containing cuts on a moving interface are healed before the new cut is made. In this general way, any process involving a moving material interface may be modeled as long as a method to calculate that process' growth or movement rate is available. This addresses our original problems with modeling phenomena with moving material interfaces: accounting for the loss of original material and the mechanical response of all materials.

First steps in developing this capability are to demonstrate that XFEM is able to accomplish the basic tasks of cutting the mesh at the correct location, assigning material properties to appropriate sections of the block, and ensuring continuity of variables across the material interface independently of physics informed advection of the material interface (using the level set module). By assigning a prescribed level set function that drives the material interface, the efficacy of XFEM's methods is separated from the need to solve for the level set function; confining our results to XFEM's performance.

While the level set module is not employed, the XFEM module's class LevelSetCutUserObject is still used to determine where the cut should be made on the mesh based on the prescribed level set function as well as determining whether to utilize healing methods. The XFEMSingleVariableConstraint class specifies the constraints on a variable at the material interface and how to enforce jumps or continuity of that variable at the interface (Niche or penalty methods). In the more generalized XFEM block, options for XFEM methods may be specified such as the quadrature weighting rule to utilize. Finally, in the Materials block, properties specifically associated with each discrete material must have a provided base_name parameter so that the appropriately dimensionalized bimaterial material property class (LevelSetBiMaterialReal, LevelSetBiMaterialRankTwo, or LevelSetBiMaterialRankFour) may assign the property to the correct material within the block based on a provided level set function sign (positive corresponding to one material, negative to another).

With an understanding of the implementation of discrete two material region problem setup in the XFEM module, we demonstrate the results of a verification problem currently committed in the XFEM regression tests. This problem is constructed using the Method of Manufactured Solutions to solve a quasi-1D, 1st order, two material region transient heat transfer problem with homogeneous properties in each material in Cartesian coordinates. The differential equation describing time dependent heat transfer is

$$\rho c_p \frac{\partial T}{\partial t} - \nabla k \nabla T = q \ , \tag{12.7}$$

which may be expressed in 1D as

$$\rho c_p \frac{\partial T}{\partial t} - \frac{\partial}{\partial x} k \frac{\partial T}{\partial x} = q \ . \tag{12.8}$$

The domain in the x coordinate is defined by $\Omega_x = [0,1]$ and divided into 20 elements. The initial condition for temperature is $T(x,0) = 600$, and the prescribed level set function is

$$\phi(x,t) = 0.75 - x - 0.001t \ , \tag{12.9}$$

(initial interface location is at 0.75). Material properties are $(\rho c_p)_A = 10$, $(\rho c_p)_B = 7$, $k_A = 20.0$, and $k_B = 2.0$ with A being the material to the left of the interface and B the material to the right. The prescribed solution is piecewise in each material region

$$T(x,t) = 605 - 5x + t(8-x), \quad x < i \tag{12.10}$$

$$= \frac{1}{(1-i)}((-5+5i+it-2t)x + (605-605i+8t-7t)), \quad x > i \ , \tag{12.11}$$

where i is the interface position at any time

$$i = 0.75 - 0.001t \ . \tag{12.12}$$

The boundary conditions fall out of the prescribed solution; the left side of the solution is chosen as a Dirichlet condition

$$T(0,t) = 605 + 8t \ , \tag{12.13}$$

while the right end of the domain is bounded by a Neumann condition

$$\left.\frac{\partial T}{\partial x}\right|_{x=1} = \frac{k_B}{(1-i)}(-5+5i+it-2t) \ . \tag{12.14}$$

The source term is also derived from the prescribed solution and follows its piecewise nature

$$q(x,t) = (\rho c_p)_A(8-x), \quad x < i \tag{12.15}$$

$$= \frac{(\rho c_p)_B}{(1-i)}((i-2)x + (8-7i)), \quad x > i \ . \tag{12.16}$$

The last components required to model this problem are the continuity conditions at the interface. The value at the interface should be the same between the two material regions

$$T_A(i,t) = T_B(i,t) \ , \tag{12.17}$$

but there is an abrupt jump in flux (ϕ, not to be confused with the level set function of the same notation) defined by

$$\Delta\phi(i,t) = k_A \left.\frac{\partial T_A}{\partial x}\right|_i \cdot \vec{n} - k_B \left.\frac{\partial T_B}{\partial x}\right|_i \cdot \vec{n} \ , \tag{12.18}$$

which when the temperature solution is applied becomes

$$\Delta\phi(i,t) = k_A(5+t) + \frac{k_B}{(1-i)}(-5+5i+it-2t) \ . \tag{12.19}$$

These conditions derived from the prescribed temperature are utilized in the simulation to determine how closely the code is able to obtain results to the prescribed solution. Figure 12.2 illustrates the results of the simulation plotted alongside the prescribed solution. At this resolution, the XFEM solution temperature matches the exact solution very well: showing the linear nature of the solutions as well as the abrupt change in flux at the interface. However, to get a realistic picture of the differences in code results, we should interpret the results of Figure 12.3. This gives the element L2 errors between the XFEM results and prescribed solution at all three timesteps that were run. Error is relatively low, but of most concern is the slight increase in error between the third and second timesteps which demonstrates some instability in our methods.

The leading theory as to where this error comes from is that the quadrature weighting methods currently employed are inconsistently accounting for some aspect of the elements cut by XFEM (aspect ratio, shape, etc.). Further investigation would be of interest to identify and quantify this error, but for now, this investigation has illustrated that the XFEM moving interface method has small enough error to move forward with developing a use case for it.

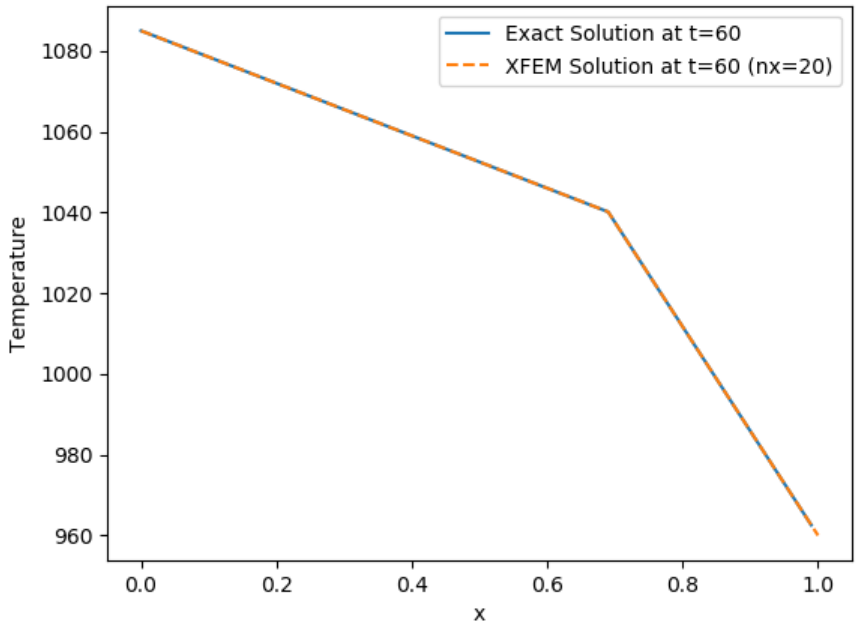

Figure 12.2: Simulation results and prescribed solution for XFEM MMS verification problem at $t = 60$.

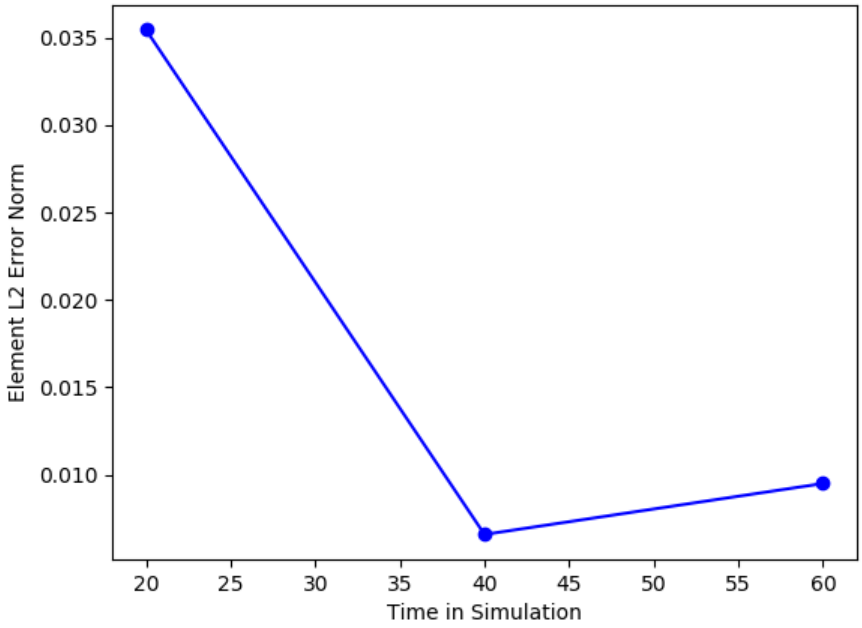

Figure 12.3: Element L2 error norms at each solved timestep.

In an effort to demonstrate the utility of the developed capability, one of the earlier discussed applications for this coupled level set and XFEM method work is explored. A primary concern in fuel performance modeling is corrosion of zirconium alloys as it contributes largely to many methods of failure in nuclear fuels. This seems to be a singularly excellent example of the type of modeling challenge that would benefit from the coupled XFEM and level set work as it concerns discrete material interfaces and Zircaloy oxidation growth rates are temperature dependent. The current finite element based oxidation modeling approach in Bison is limited to nodal boundary value calculation with a thermal resistance applied based on the calculated thickness of the oxide layer at a specific axial position. By employing the coupled XFEM and level set method, material changes are physically modeled in the mesh which much more accurately simulates real world material responses to thermomechanical changes in nuclear fuel cladding.

So to go about implementing coupled level set and XFEM oxidation, a Material kernel is developed. Before beginning this development though, in order to reduce the amount of duplicate code in Bison, Zircaloy oxidation models are separated from the current oxidation method's class into a utility file containing a function for each model so that either the current oxidation class ZryOxidation or the developed ZryOxideGrowthRate class may either utilize the models. The oxide growth rate class utilizing coupled level set and XFEM is similar to the nodal method in its calculations with two major exceptions. As each material now has its own physical section on the mesh, the beta phase fraction and oxygen weight gain calculations from the ZryOxidation class need to be assigned to the parts of the zirconium alloy material near the oxidation interface which requires a nontrivial amount of work to implement; so for now, neither of these properties is calculated in the coupled oxidation class. The other main difference between the two oxidation classes is the coupled oxidation class is meant to calculate dimensional components of the oxide growth rate so that the level set module's advection kernel may use them to move the material interface. This is accomplished by calculating the oxide scale growth rate and multiplying it by the normalized temperature gradients of each dimension at the nearest node.

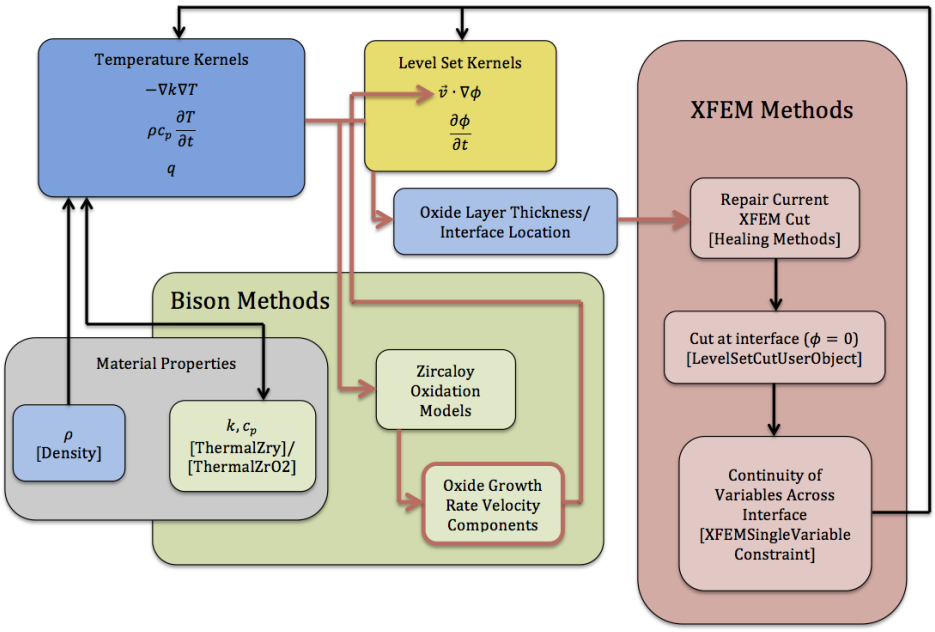

Figure 12.4: XFEM/level set coupled oxidation implementation diagram.

Now being able to determine velocity components, some processing is required before the advection Kernel is able to use them. As it is being calculated in a Material class, the oxide growth rate calculated is given at quadrature points, but for a Moose Kernel to use it, the variable must be given at nodes on the mesh. An Auxiliary Kernel MaterialRealVectorValueAux is used to both separate the oxide growth rate variable into respective dimensional components and interpolate the values at quadrature points to obtain values at the nodes. Now, we have everything we need to provide to the level set advection Kernel and have developed the preliminary coupled level set and XFEM oxidation capability. Figure 12.4 illustrates how oxidation methods feed into the level set solve that then provides XFEM with a location

to cut which determines the new mesh for the next timestep to be solved upon. Items highlighted in red emphasize contributions from this activity that were developed or used in conjunction for the first time while in the course of advancing the coupled oxidation capability.

Ideally, again, we would construct problems to verify the code's implementation with a method of manufactured solution problem, but there are a few obstacles to overcome to accomplish this when dealing with oxidation problems in Bison. Specifically, the need to utilize temperature dependent (and thus, coordinate dependent) material properties in ParsedFunction objects is problematic as there is not currently a method to accomplish this. However, we already have an idea of the level of accuracy with which XFEM is able to model a heat transfer problem with a moving material interface due to the earlier verification problem; so for the time being, our investigation into the results of a simple coupled level set and XFEM oxidation problem is a qualitative verification assessment of the level set module being able to move the material interface based on oxidation models' prediction of oxide growth rates.

Again, we are interested in a time dependent heat transfer problem (Equation 12.7) but also need to solve the level set advection equation (Equation 12.6). Temperature decreases in the y direction so we may ensure a varying rate of oxidation along the axial direction of this representative length of cladding. There is no need for a source term as we do not need to artificially influence the solution to meet a prescribed temperature solution ($q(x,t) = 0$). The domain is $[\Omega_x, \Omega_y] = [[0, 575.0 \times 10^{-6}], [0, 1200.0 \times 10^{-6}]]$ with 8 elements in x and 4 elements in y. Dirichlet boundary conditions range from 620.0 K to 618.35 K from bottom to top of the clad on the left (inner) side of the cladding material to 580 K all along the right (outer/coolant) side. The material interface is located at 470.0×10^{-6} at the initial timestep with the level set function's initial condition

$$\phi(x, y, 0) = 470.0 \times 10^{-6} - x \ . \tag{12.20}$$

Densities for materials are given as 6550.0 kg/m^3 for Zircaloy and 5680.0 kg/m^3 for zirconium dioxide (ZrO_2). Thermal properties (k, c_p) are calculated for each material from the Bison's ThermalZry and ThermalZrO2 classes. Like the XFEM only verification problem, the value at the interface needs to be the same between materials (Equation 12.17), but in this case, the flux jump also will be zero (continuous flux conditions). Oxidation models employed in this simulation are Bison's default models: EPRI_KWU_CE for normal operating temperatures and Leistikow for high temperatures. The oxidation growth rate is scaled by 1.0e4 in order to more clearly demonstrate temperature effects on the oxide growth rate.

Temperature results for this problem at 50 seconds into the simulation are plotted in Figure 12.5.
The two dimensional plot shows the temperature throughout the cladding mesh and a radial temperature profile at $y = 0$. The difference in heat transfer rates between cladding material and oxide is immediately apparent with the cladding having a small temperature difference between the inner surface and metal-oxide interface while the oxide demonstrates its low thermal conductivity and higher thermal resistance with a large difference in temperatures. This at least illustrates that the code is applying material properties to the correct sides of the interface consistently and is able to solve the heat transfer problem throughout the material regions. Another concern in this simulation is whether the oxide interface grows at a rate consistent with its dependence on temperature. Oxide growth rates are positively correlated to temperature, so the higher the temperature at the metal-oxide interface, the more oxide growth there should be. Figure 12.6 shows the oxide growth rate versus interface temperature for differing axial positions at 50 seconds into the simulation. The results are consistent with the expected behavior, as locations with higher temperatures did see more oxide growth than lower temperature positions.

These results demonstrate the utility of XFEM coupled to level set solutions driven by modeling rates of physical phenomena. While they are currently limited to heat transfer, incorporation of mechanical feedback is forthcoming. Future work includes general XFEM investigations into verifying moving interface problems in RZ coordinates and identification and reduction of error due to quadrature weighting, further development of coupled level set and XFEM oxidation, as well as validation studies for oxidation modeling. Bison development specifically would include Method of Manufactured Solutions problems for verification, alpha zirconium phase growth and material properties modeling, and feature additions to the current coupled oxidation modeling in Bison to be more consistent with the nodal oxidation models (adding oxygen weight gain and hydrogen diffusion). Verification studies for the coupled oxidation are currently underway with the aim of comparing results and performance between the current assessments for REBEKA LOCA cases and coupled oxidation versions of these cases. Looking past oxidation, interest has been high in expanding the applications utilizing level set advected XFEM material interfaces and boundaries including central void formation and pore migration in ceramic nuclear fuels, eutectic formation in metal fuels, and melting.

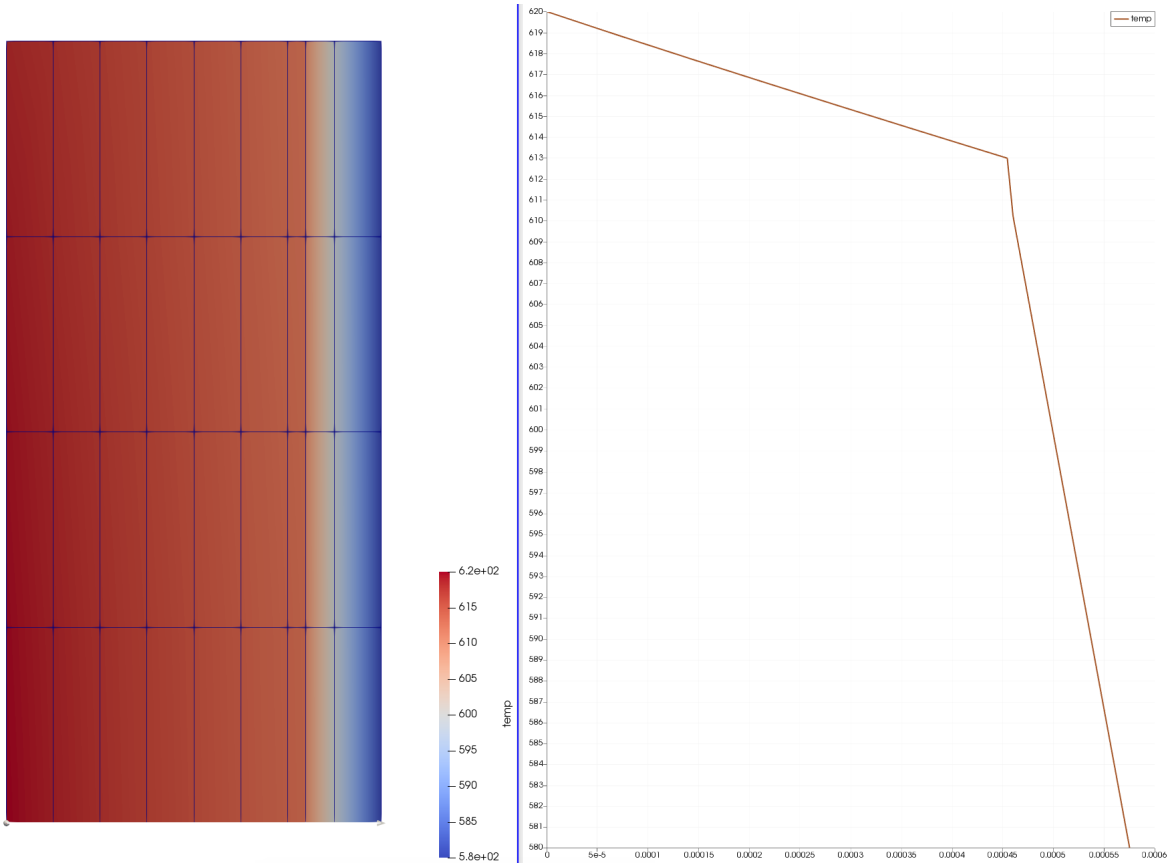

Figure 12.5: Results from heat transfer oxidation simulation at $t = 50$.

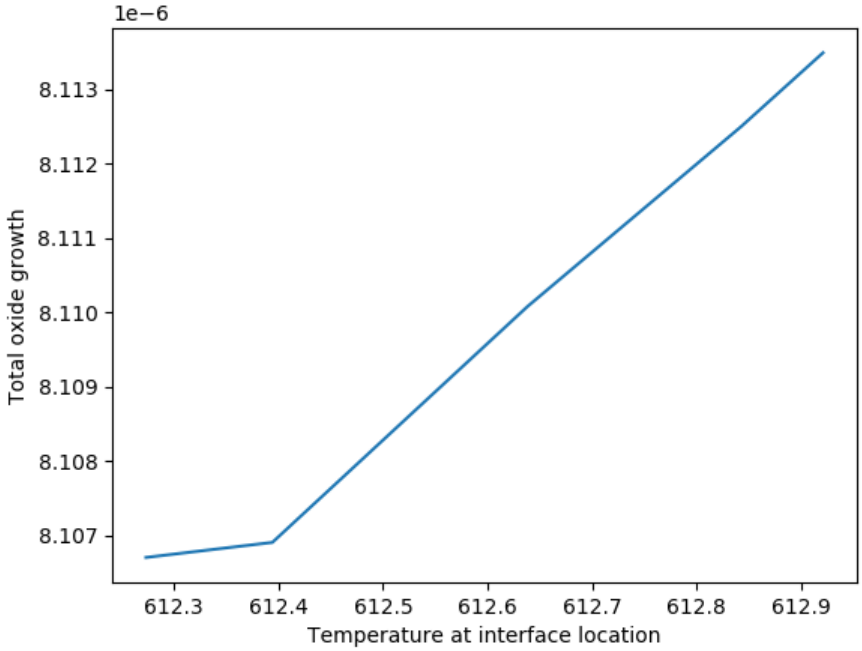

Figure 12.6: Oxide growth vs temperature at metal-oxide interface for coupled oxidation simulation.

12.3 Improve code robustness and plan/implement rigorous material model testing for metallic fuel

S. R. Novascone
A. M. Jokisaari

There have been developments, both realized and potential, regarding improvements to code robustness in FY19. An example of a potential improvement is described in chapter 12.1 of this report. Another potential improvement is the new automatic differentiation feature in MOOSE, which calculates derivatives for material models and kernels with respect to primary variables. This feature should reduce errors in writing code, that could lead to convergence trouble, and thus improve robustness. For more information about automatic differentiation in MOOSE, see mooseframework.org.

A realized example of code robustness is an improvement made to gap conductance models. Recall that gap conductance is defined as thermal conductivity in the gap (between fuel and cladding) divided by the gap size. After experiencing trouble with convergence on many metallic fuel simulations, we discovered that the relatively large gap conductance (as compared with LWR) was causing trouble with the solve procedure. Limiting the size of the gap conductance eliminates the issue with convergence, and fortunately, has little impact on the converged solution. Figures 12.7 and 12.8 demonstrate this fact. Figure 12.7 shows the change in gap conductance vs. gap size, which of course follows 1/x behavior. Figure 12.8 shows the corresponding change in fuel center temperature. Despite the rather large change in gap conductance, the fuel center temperature changes very little. So, in the case of metallic fuel simulations, we now set the gap conductance to a constant value. We also made changes to minimize how quickly gap conductance changes as gap size approaches zero, which has resulted in increased robustness.

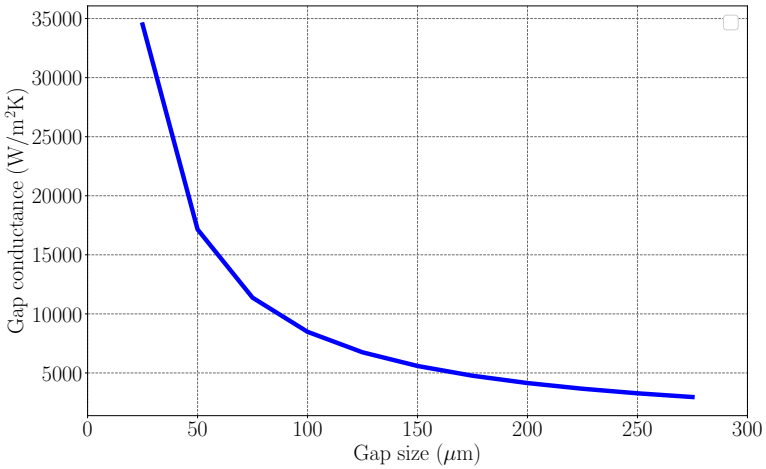

Figure 12.7: Representative gap conductance vs. gap size for sodium-bonded metallic fuel

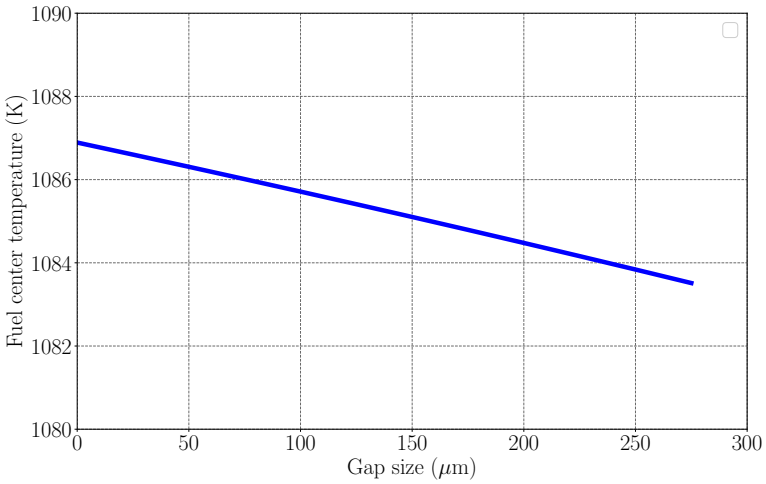

Figure 12.8: Representative fuel center temperature vs. gap size for sodium-bonded metallic fuel

Improvements have also been made to the rigor level of regression tests, particularly for metallic fuel material models. For example, a zirconium diffusion test that verifies phase stability information and uses it to evaluate Fickian and Soret diffusion parameters and their derivatives with respect to temperature and zirconium. This test calculates diffusion parameters and their derivatives for eight compositions, temperatures, and combinations of stable phases. Rather than checking a single input, the test goes through a range of input parameters and verifies that the model is returning expected values. This approach is expected to improve robustness by identifying and mitigating trouble with the material model in a simple test before it's used in the simulation of an integrated fuel pin, where diagnosing convergence issues is more difficult. More work is required in this area to ensure that material models are properly tested and documented before being added to the code.

The improvements of FY19 have enabled more rigorous multiphysics testing of fuel slug and cladding behavior, *i.e.*, integral testing. Integral testing must be a focus moving forward as new materials models are developed. Oftentimes, models are designed in anticipation of a small set of use conditions; when multiple models are combined to study a multiphysics scenario, interactions between models or parameters (such as power history) may result in unanticipated behavior. As new models are designed, they should be tested in a full fuel performance scenario to assess their behavior; if they are replacing an existing model, the difference in parameters of interest should be quantified. For example, metallic fuel generally undergoes creep during service, but is sometimes modeled as elastic (without creep). The difference in radial fuel swelling when modeled as elastic versus with creep is shown in Fig. 12.9. Evidently, radial strains increase further after fission gas release (which occurs around 4% burnup here) with creep active in the model. Similar effects should be considered with additional model development.

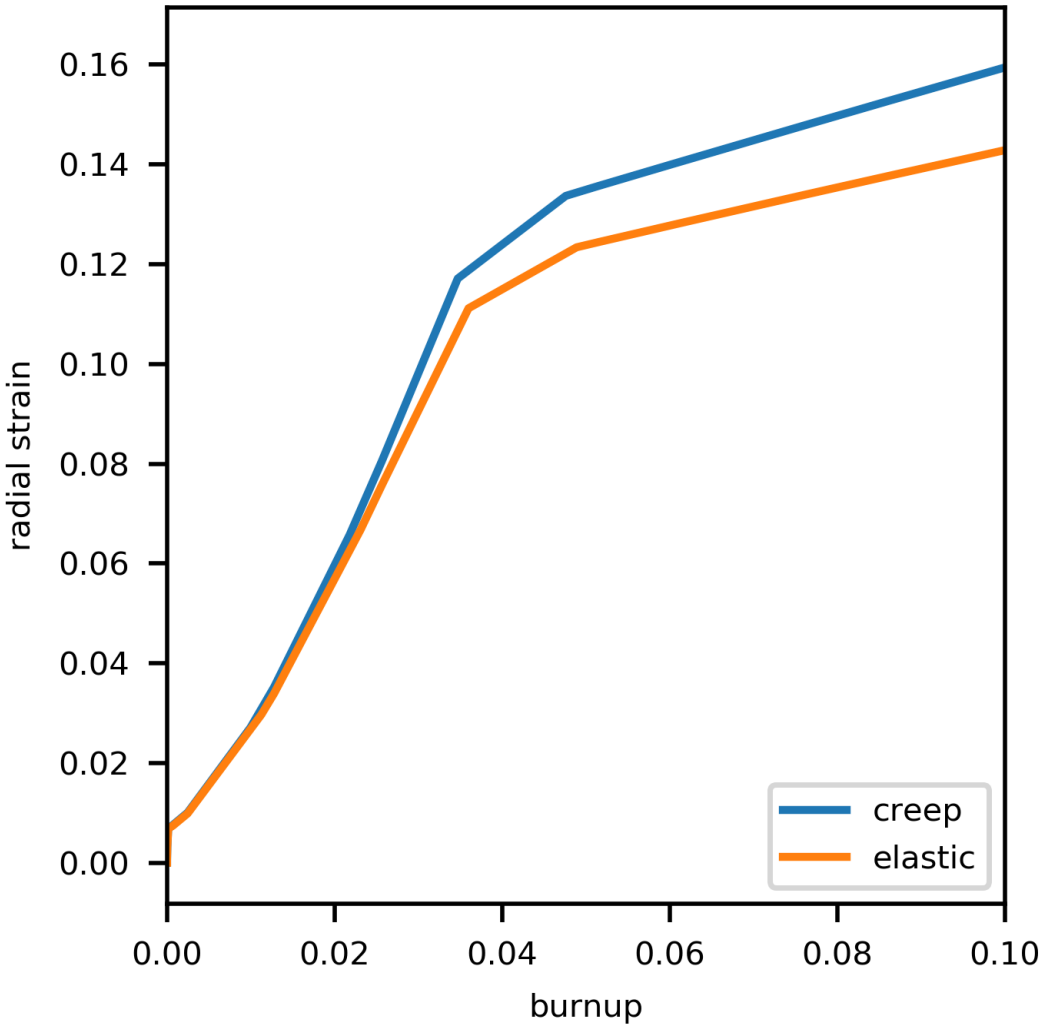

Figure 12.9: Radial fuel swelling as a function of burnup (FIMA) for the EBR-II X441 group A assessment case including fuel creep, and simplified to elastic fuel.

12.4 Evaluation of robustness and efficiency of assessment cases

D. S. Stafford

As part of an ongoing effort to improve the efficiency and robustness of LWR fuel rod simulations using Bison, we benchmarked one of the large full-rod assessment cases and investigated potential for better performance. The USPWR 16x16 TSQ002 case was selected because of its relatively large resident size in memory, because it has a relatively long run time, and because it applies so many of the physical models available in Bison. Ultimately, we found that the run time of this case could be improved by roughly 30% when using a combination of a higher-performance linear solver and a more advantageous time stepping strategy. This combination simultaneously eliminated all failed nonlinear solver steps and should contribute to successful simulations of complete rods in other cases as well.

12.4.1 Time stepper robustness

Initial investigation of the run time of the TSQ002 assessment case indicated that much of the run time was being spent on ”tough” time steps. This behavior is demonstrated in Figure 12.10; the solver spent $\approx$ 40% of the run time attempting to converge time steps that eventually failed and had to be discarded. Note also that the number of nonlinear iterations for the successful time step after each failure is entirely reasonable at around 5-7 steps in most cases. A closer look revealed that the nonlinear solver was failing at these time steps simply because it was trying to step over large changes in the forcing function that applies the heat rate to the LWR rod.

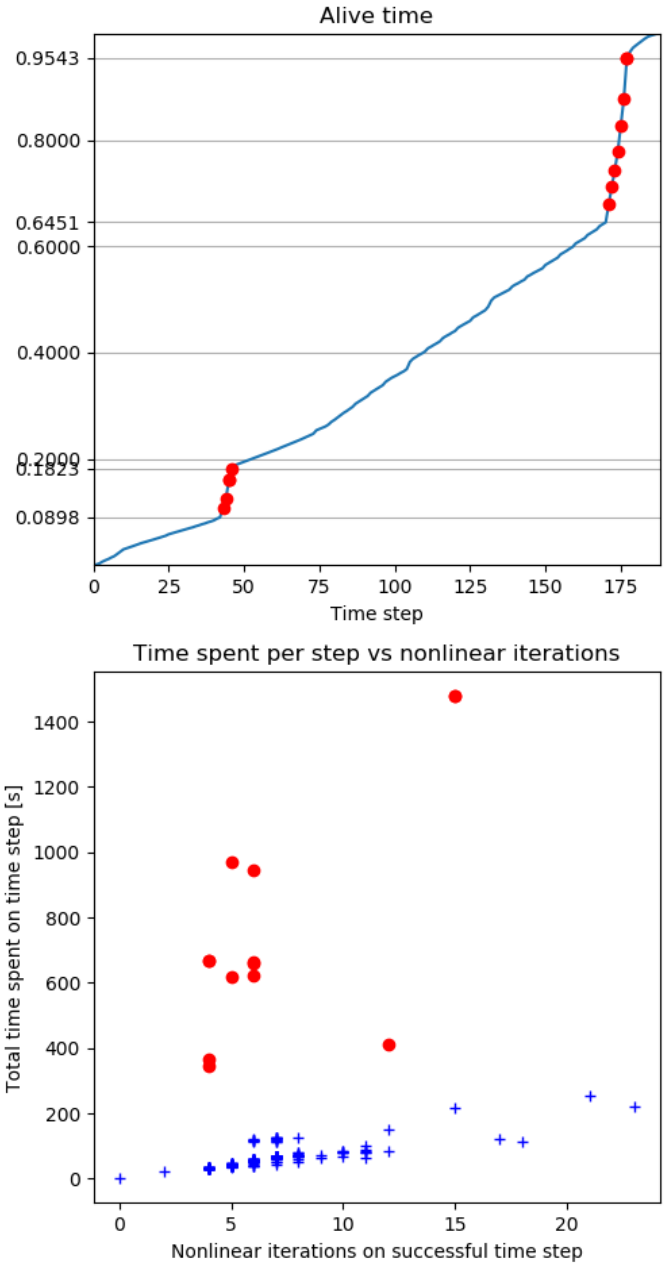

Figure 12.10: Nonlinear solver performance of Bison for USPWR TSQ002 assessment case. The red dots indicate time steps where the solver failed to converge and had to cut the time step.

Two possible fixes existed at the time: either force a time step limit at every place where the (piecewise linear) linear heating rate changes or force a time step limit when the linear heating changes by a specified amount. Using the former strategy could lead to an unnecessary increase in time steps, so we applied the latter solution. The IterationAdaptiveDt already had a feature that allowed enforcement of maximum function change, but a minor code update was needed to ensure that the feature did not skip over rapid transients.

After applying the code fix, the TSQ002 case ran $\approx 17\%$ faster without further optimization. More significantly, the time stepper did not fail to converge on any of the steps. Thus, this feature can be applied judiciously to cases in the future to improve convergence robustness and overall run time.

12.4.2 Performance of the preconditioner

We also benchmarked the time the solver spends during preconditioning of the Jacobian – again for the USPWR TSQ002 assessment case — in relation to the number of MPI processes used for the run. As part of this study, we also benchmarked strong scaling and found that the TSQ002 case scales well ($> 50\%$ parallel efficiency) up to 32 MPI processes. In this region of acceptable efficiency, the linear solver accounts for up to $1/3$ of the total run time and is a potential place for improvement.

Therefore, we benchmarked the linear solver packages MUMPS, PARDISO, and STRUMPACK versus the incumbent SuperLU. SuperLU has been the suggested method for preconditioning Bison runs for several years now because it robustly outperforms iterative preconditioners such as AMG methods and additive Schwartz on the problems for which Bison is typically used. SuperLU performs a supernodal (directed-acyclic graph) LU factorization with $O(N^2)$ FLOPS and has $O(N^{4/3})$ memory requirement. It is an optional package for PETSc and requires no other options to make it work well for LWR simulations.

More recently, multi-frontal solvers such as MUMPS [1], PARDISO [2], and STRUMPACK [3] have been developed; they typically have $O(N^{4/3}\log N)$ FLOPS and $O(N)$ memory usage and should therefore outperform SuperLU for most Bison simulations. We tested these three packages and found that MUMPS did not outperform SuperLU on several tests. In addition, we ruled out PARDISO due to licensing concerns with Intel's MKL. However, STRUMPACK did perform better than SuperLU on large Bison runs, as shown in Table 12.3. Although both preconditioners scale poorly past 16 MPI processes, STRUMPACK takes 30% less time than SuperLU at 32 processes, enabling Bison to achieve $\approx 50\%$ parallel efficiency at 32 processes.

Table 12.3: Parallel scaling efficiency for SuperLU vs STRUMPACK on the USPWR TSQ002 assessment case.

MPI procs	Fraction of runtime		Parallel efficiency	
	SuperLU	STRUMPACK	SuperLU	STRUMPACK
4	0.13	0.11	1.00	1.00
8	0.19	0.13	0.58	0.77
16	0.28	0.17	0.31	0.48
32	0.37	0.26	0.16	0.23
36	0.40	0.27	0.14	0.20

As with SuperLU, STRUMPACK is also optional for PETSc and can be used with several different sparsity reordering packages. However, due to issues with its build system, it will not be included in the MOOSE redistributable packages. Nevertheless, STRUMPACK should be considered an expert option for very large cases due to its superior scaling efficiencies with large numbers of degrees of freedom.

Bibliography

[1] P. R. Amestoy, I. S. Duff, J. Koster, and J.-Y. L'Excellent. A fully asynchronous multifrontal solver using distributed dynamic scheduling. *SIAM Journal on Matrix Analysis and Applications*, 23(1):15–41, 2001.

[2] D. Kourounis, A. Fuchs, and O. Schenk. Towards the next generation of multiperiod optimal power flow solvers. *IEEE Transactions on Power Systems*, PP(99):1–10, 2018.

[3] Strumpack – structured matrices package, version 00, 12 2014.

12.5 Support MW-scale micro reactor development and analysis

S. R. Novascone
W. Jiang

Megawatt scale, so-called micro reactors, seem to be of increasing interest to DOE; there are several programs that support micro reactor-related work. In FY19, NEAMS supported development activities for micro reactors, which consisted of running simulations that demonstrate coupling between several MOOSE applications: Bison, Sockeye, Mammoth, and Rattlesnake. These applications were bundled to create a new MOOSE application called DireWolf. In DireWolf, Bison solves thermo-mechanics equations, passes temperature and displacements to Mammoth, and passes cladding temperature to Sockeye. Sockeye provides the thermal boundary condition to Bison and Mammoth passes power density to Bison. See figure 12.11 for a slightly more detailed description. Also see the recent INL report [1] for a more in-depth description. A significant amount of time was spent supporting this work. Our efforts focused on preparing Bison models (input files) for use in DireWolf simulations and a mesh convergence study, which is documented in [1] and demonstrates the expected high computation expense of full-core micro reactor simulations.

12.5.1 Penalty Enforcement of an inclined boundary condition

The monolith core of micro reactors often have a symmetric hexagonal pattern. To take advantage of symmetry, we need to model only a portion of the actual geometry to reduce the computation time. On the symmetry boundaries, the displacement vector component perpendicular to the plane should be zero. The `PenaltyInclinedNoDisplacementBC` was implememented in MOOSE to enforce $\mathbf{u}\cdot\mathbf{normal} = 0$ for mechanics problem. With a penalty method, the residual is given as

$$\mathcal{R}_i = \alpha(\mathbf{u}\cdot\mathbf{normal})\mathbf{normal}(\text{component})\psi_i \tag{12.21}$$

where α is the penalty parameter and 'component' corresponds to the direction in which to apply the residual. The normal directly comes from the surface normal defined in a mesh.

The `InclinedNoDisplacementBCAction` BC was also implemented to simplify the input file when several variables have the same inclined no displacement boundary condition applied in the normal component. Figure 12.12 and 12.13 shows the 2D and 3D examples using the inclined no displacement boundary condition.

Bibliography

[1] Piyush Sabharwall, Ching-Sheng Lin, Joshua Hansel, Vincent Laboure, David Andrs, William Hoffman, Stephen Novascone, Andrew Slaughter, and Rich Martineau. Application of integrated modeling and simulation capabilities for full scale multiphysics simulation of microreactor concepts. Technical Report INL/EXT-19-55159, Idaho National Laboratory, 2019.

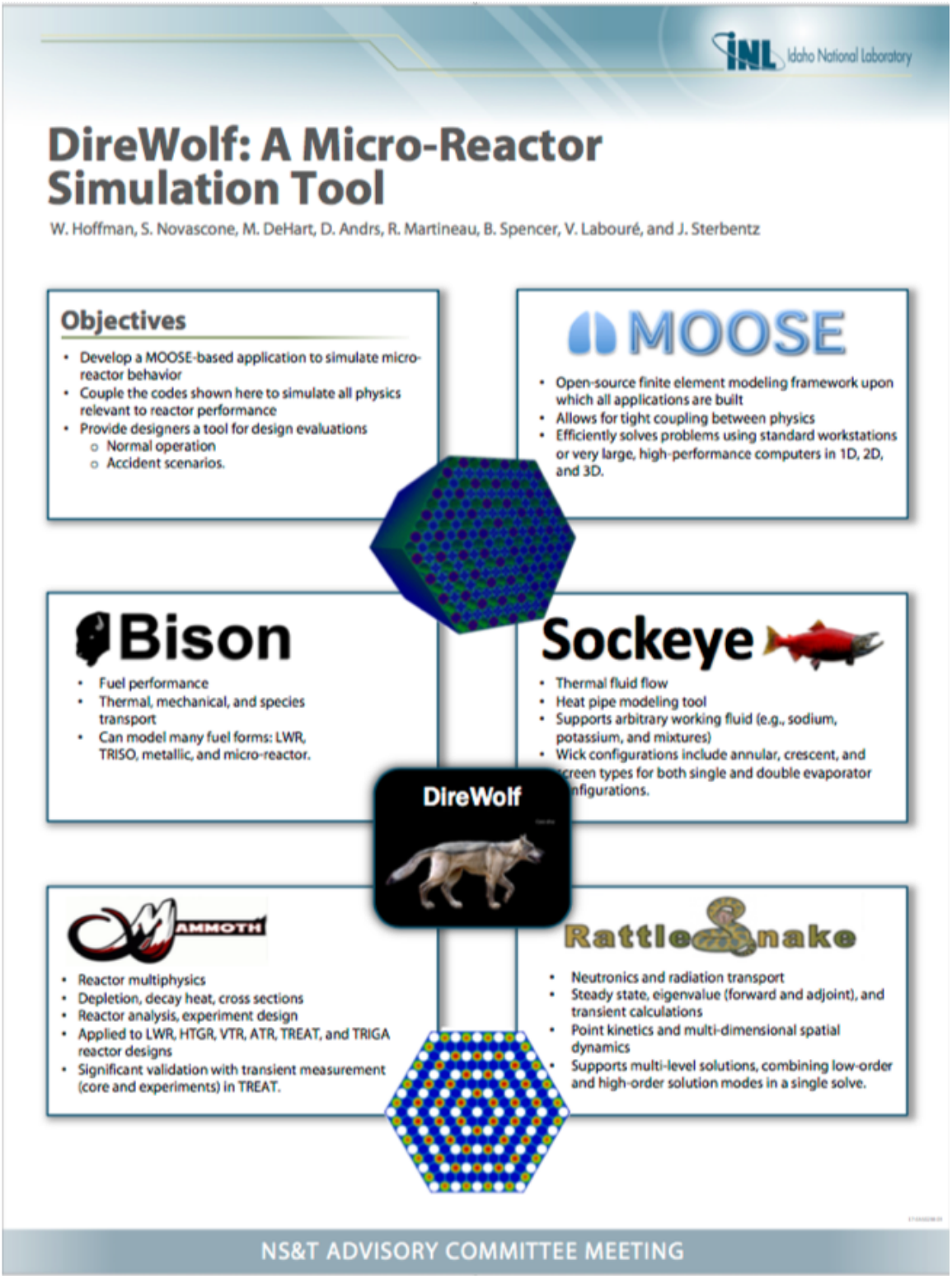

Figure 12.11: A brief description of Direwolf

(a) **(b)**

Figure 12.12: 2D example: inclined no displacement boundary conditions are prescribed and a uniform displacement loading is applied on the top.

(a) **(b)**

Figure 12.13: 3D example: inclined no displacement boundary conditions are prescribed and a uniform displacement loading is applied on the top.

12.6 Improve code documentation and testing

S. R. Novascone

Many improvements have been made to documentation and testing. The chapter on migrating the assessment cases to an online form, documented in 11, and the improvements in testing discussed in section 12.3 of this chapter are examples. The Bison training workshop slides are also migrating to an online form. These improvements are reflected in updates we make to bison.inl.gov, the outward facing website, where the public can read about the curated features of Bison. The online documentation approach we've adopted from MOOSE is a powerful resource to Bison beginners, advanced users, and developers. We plan to continuously develop this feature.

12.7 Provide training and support material model development (particle fuel)

The advanced reactor community is in need of specialized training for using NEAMS tools. As such, we've reached out to several members in industry and at the NRC and provided training and continue to provide support. The next section lists the Bison training we've held in FY19.

12.8 User training and support

- Kairos October 17-18
- General Atomics May 2-3
- INL June 11-12
- Westinghouse (Pittsburgh) June 18-19
- Top Fuel (Seattle) planned for September 27

An expected result from conducting these training workshops is an increase in user support. This is time-demanding and requires an increase in funding from the sponsor and attention by the development team.

Chapter 13

Future work

The following sections highlight proposed milestones and activities that logically follow prior work. The actual work, of course, depends on the FY20 budget.

13.1 Demonstrate physics-based, LLS-informed swelling model that predicts EBR-II observations

S. R. Novascone
A. Casagranda

Despite recent progress in numerical stability and the inclusion of more physical phenomena, current models in Bison continue to underestimate fuel swelling. It is important to accurately predict swelling, porosity interconnection (fission gas release), and cladding wastage due to fuel-cladding chemical interaction. The timing and combined effect of these phenomena impact cladding mechanical performance. In other words, the duration of cladding exposure to increased plenum pressure and contact with the fuel decreases the amount of time cladding will maintain its intended structural function. By applying lessons learned from prior years of model development and our increasing familiarity with EBR-II data, we plan to calibrate parameters in current models to duplicate EBR-II measurements and demonstrate this in multiple assessment cases. Furthermore, we plan to leverage lower-length scale knowledge and models to enable engineering scale model updates and defend model calibration.

13.2 Develop strain-based design criteria for cladding performance limit

S. R. Novascone
A. Casagranda

Historically we've used cumulative damage index to determine cladding performance limit. This approach relies on having a large statistical database. In the absence of this large database, as is the case for cladding used in metallic fuel, we plan to use results from separate effects measurements and simulations to establish a bound on cladding strain that includes transients. With focus on lower length scale, this effort will include advancing the state of cladding mechanical properties and models with documentation of the corresponding impact on cladding performance limit calculations. VTR personnel have expressed interest in this, and we plan to proceed with their feedback.

13.3 Demonstrate species migration and correlate to wastage

S. R. Novascone
A. Casagranda

While we've demonstrated some success in solving Zr redistribution, we've also struggled to solve these types of diffusion equations when implicitly coupled to thermo-mechanics equations. We plan to utilize multi-apps to solve the diffusion equations in isolation. This approach is expected to improve numerical stability. We can also apply this approach to lanthanide migration and begin cladding wastage calculations when fuel-cladding contact commences followed by lanthanide arrival at the interface. Deliverables are demonstration of the multi-app approach and comparison

between EBR-II measurements and Bison calculations for Zr redistribution and cladding wastage calculations that correspond to the timing of lanthanide migration.

13.4 Develop and demonstrate models for TRISO fuel kernels

G. Pastore

The primary effort will be to develop models to simulate fission product redistribution in UCO fuel, which is preferred over UO2 since it provides resistance against kernel migration and internal pressure buildup caused by excessive CO formation. UCO thermal and mechanical models will also be implemented in Bison as needed. A small effort is anticipated to complete implementation of any PARFUME UO2 models in Bison. Model validation will be performed to the extent experimental data are available. Close coordination with industrial partners will be maintained.

13.5 Develop and demonstrate models for graphite plus extend fuel particle failure capability

G. Pastore

The major focus here will be development and early assessment of thermal and mechanical models for graphite, which is widely used in HTGR applications. Early efforts will be needed to understand material applications (e.g., graphite vs graphite-matrix) to identify and prioritize needed properties and models. It is clear that oxidation is an important failure mechanism for graphite, thus models of this behavior will be included. Development will continue to improve and optimize Bison's capability to perform statistical fuel particle failure analysis, a capability introduced and initially demonstrated in FY19. In all areas, initial model validation will be performed to the extent experimental data are available. Close coordination with industrial partners will be maintained.

13.6 Develop and demonstrate initial capability to simulate UC and UN fuel

G. Pastore

Important industrial collaborators have expressed the need to simulate UC and UN fuel for advanced reactors. Capability development will begin for UC by incorporating existing correlations in Bison for thermal and mechanical properties. The key research effort for UC will then be development of reliable models to predict fuel swelling which, due to the shortage of experimental data, will be strongly supported by physics-based LLS models. With the experience gained from UC, initial efforts will be made to extend this work to UN. Model validation will be performed to the extent experimental data are available. Close coordination with industrial partners will be maintained.

13.7 Bison development and validation for priority LWR-ATF fuel concepts, including LLS-informed modeling

G. Pastore

This milestone will focus on modeling developments, implementation in Bison and code validation for priority LWR-ATF fuel concepts. The ATF concepts that will be targeted are (i) advanced UO2 (Cr2O3-doped) and (ii) uranium silicide (U3Si2) fuels. Engineering models will be informed by LLS calculations to fill the experimental data gap. Models that will be developed include advanced multiscale models for fission gas release, gaseous swelling, grain growth and densification. Modeling of creep and cracking, and the impact on pellet-cladding interaction (PCI) behavior, will also be investigated. Experimental validation will be performed through simulation of ATF experiments with Bison, such as the integral Halden fuel rod tests and the ATR irradiations, and comparisons to experimental data. Code-to-code comparisons will also be performed where possible. Validation will be complemented by uncertainty quantification to assess the effects of the uncertain modeling parameters, including those derived from LLS calculations, on the fuel performance simulation results. Engagement with NRC, industry, and the AFC ATF program will be continued and enhanced.

13.8 Bison developments for LWR-UO2/Zry fuel analysis at high-burnup and during design-basis accidents, including LLS-informed modeling

G. Pastore

This milestone will focus on Bison developments for the analysis of UO2/Zry fuel system behavior during high-burnup and design-basis reactor accident scenarios (LOCA, RIA). As many fundamental effects on the thermal, mechanical and fission gas behavior of high-burnup UO2 fuel are related to the formation of the high-burnup structure (HBS), such Bison extension will involve the development and implementation of a model for the formation of the HBS. Also, the Bison model for fission gas behavior (FGR and gaseous swelling) will be extended to consider high-burnup effects. For accident fuel behavior, modeling developments will include (i) fuel fragmentation during accidental transients and the related (ii) axial relocation of fuel fragments during cladding ballooning. Atomistic and meso-scale simulations of the evolution and properties of the high-burnup structure will be undertaken to inform engineering-scale models for HBS formation, fuel fragmentation and FGR. Finally, an initial engineering model will be developed for cladding hydriding and the associated cladding embrittlement, which is important for both high-burnup and accident fuel analysis. LLS simulations will also be pursued for describing hydride evolution and mechanical properties, to be used for assessment of the corresponding engineering-scale capabilities.

13.9 Bison demonstration and validation for LWR-UO2/Zry fuel analysis under off-normal reactor conditions

G. Pastore

This work will focus on demonstration of Bison capabilities and code validation for the analysis of UO2/Zry fuel system behavior during design-basis accidents as well as load-follow situations. The validation base of Bison for modeling design-basis accidents will be expanded. In particular, validation will target integral fuel rod LOCA experiments from the Halden Legacy Database, which allow for an assessment of the whole suite of models for accident analysis in Bison, including fuel axial relocation. Other experiments will be considered, such as separate-effects LOCA tests and/or RIA power pulse tests. Additional Bison capability demonstration for LOCA scenarios will include the application of cladding creep models developed at the LLS. Furthermore, load-follow analysis with Bison will be demonstrated through the simulation of load-follow scenarios and the comparison of results to experimental data, e.g., in terms of FGR kinetics. This may require code developments to be performed beforehand, e.g., for fission gas burst release during transients. Finally, the Bison/TRACE coupled (CRAB) capability for accident analysis will be enhanced and an initial multi-rod demonstration, with multiple rods in a core being simulated simultaneously, will be performed.

13.10 Bison algorithmic robustness, performance, ease-of-use and quality assurance improvements

D. Schwen

Bison is a major driver for current MOOSE framework capability extensions, such as automatic differentiation and mortar-based contact. These new technologies offer promise of substantial robustness and performance improvements in Bison. The two biggest computational challenges in Bison are the robustness of thermo-mechanical contact and combination of fuel creep and smeared cracking models. We will apply a combination of mortar and automatic differentiation to improve contact robustness and will explore the use of automatic differentiation and staggering to improve the robustness of combined creep and cracking models. To bring these improvements to end-users a variety of ease-of-use technical priority tasks need to be identified and accomplished, simplifying the setup of common simulation models, a reduced complexity input syntax through the use of MOOSE actions, and lowering the barrier to get Bison up and running on a wider variety of common operating systems such as Microsoft Windows through binary redistributable packages. In parallel we need to invest in continuous documentation improvements and user support, incorporating end-user feedback. To insure full NQA-1 compliance we will identify remaining issues in our design and user documentation and our test and assessment suite.

13.11 Improvements in the Bison validation base and documentation

R. L. Williamson

This work will focus on making needed improvements to the existing Bison validation base. Specific tasks will include adding new cases in targeted areas, ensuring uniform application of material models and meshing in existing cases, and developing capability for and performing statistical analyses on large sets of cases. Improvements will also be made to the validation documentation.

Chapter 14

Acknowledgments

The submitted manuscript has been authored by a contractor of the U.S. Government under Contract DE-AC07-05ID14517. Accordingly, the U.S. Government retains a non-exclusive, royalty free license to publish or reproduce the published form of this contribution, or allow others to do so, for U.S. Government purposes.